Dipartimento di Fisica

Università di Genova

ISTITUTO ITALIANO DI TECNOLOGIA
NANOSCOPY & NIC@IIT

Development of laser sources and interferometric approaches for polarization-based label-free microscopy

PhD Thesis submitted by:
Fabio Callegari

Tutor: Prof. A. Diaspro
Supervisors: Dr. A. Le Gratiet, Dr. P. Bianchini

PhD Course in Physics and Nanosciences – XXXV Cycle

Contents

Abstract 1

Preface 2

Organization of this thesis 3

I - Introduction and state of the art 5

1 - Label-Free Microscopy 6

1.1 - Overview of label-free methods 6

1.2 - Mueller Matrix Microscopy 9

2 - Light Sources in Optical Microscopy 14

2.1 - Illumination stage in an optical microscope 14

2.2 - Laser sources for microscopy 15

2.3 - Laser sources for polarization microscopy 19

II - Development of laser sources and interferometric methods 28

3 - Zeeman Laser 29

3.1 - Development and performances 29

3.2 - Stokes-Mueller description of the beating signal 33

3.3 - Fast polarization encoding in the beating signal of a Zeeman laser 35

3.4 - Conclusion 40

4 - Dual-Comb Laser 42

4.1 - Development of the DCL oscillator 42

4.2 - Characterization of the laser oscillator 45

4.3 - Broadband characterization of optical anisotropies 50

4.4 - Conclusion 57

III - Polarimetric imaging with an optical scanning microscope 59

5 - Mueller matrix microscopy with the Zeeman Laser 60

5.1 - Microscope development 60

5.2 - Mueller imaging results 64

5.3 – Conclusion 67
6 – Conclusions 69
Annexes 71
A. Mathematical formalisms for polarization description 72
A.1 Jones formalism 72
A.2 Stokes-Mueller formalism 73
B. Helium-Neon Laser and Zeeman Laser 76
B.1 HeNe Laser 76
B.2 Zeeman Laser 77
C. Elements of ultrafast laser design 78
C.1 Mode evolution in the laser resonator 78
C.2 Dispersion compensation and generation of optical solitons 80
List of scientific contributions 82

LIST OF ACRONYMS

LED: Light Emitting Diode

DFDP: Dual-Frequency, Dual-Polarization

DCL: Dual-Comb Laser

ML: Mode-Locked/Locking

PCM: Phase Contrast Microscopy

DIC: Differential Interference Contrast

QPM: Quantitative Phase Microscopy

NLM/NLO: Nonlinear Microscopy/Optics

SHG/SFG/THG: Second/ Third Harmonic Generation

SFG: Sum Frequency Generation

CRM: Coherent Raman Microscopy

SRS: Stimulated Raman Scattering

CARS: Coherent Anti-Stokes Raman Scattering

MM: Mueller Matrix

CD: Circular Dichroism

CIDS: Circular Intensity Differential Scattering

PSG/PSA: Polarization State Generator/Analyzer

LP: Linear Polarizer

HWP, QWP: Half/Quarter Waveplates

VIS: Visible

UV: Ultraviolet

IR: Infrared

LSM: Laser Scanning Microscope

MPM: Multiphoton Microscope

SLD: Semiconductor Laser Diodes

FLIM: Fluorescence Lifetime Microscopy

CW: Continuous-Wave

AOM/EOM: Acousto/Electro-Optical Modulator

DPSSL: Diode-Pumped Solid-State Lasers

OPO/A: Optical Parametric Oscillator/Amplifier

WLL: White Light Lasers

PCF: Photonic Crystal Fibers

AOTF: Acousto-Optical Tunable Filter

PER: Polarization Extinction Ratio

FSR: Free Spectral Range

ZL: Zeeman Laser

OFC: Optical Frequency Comb

RF: Radio Frequency

HV: High Voltage

SU: Stabilization Unit

PBS/UBS: Polarizing/ Unpolarizing Beam Splitters

OCP/OLP: Orthogonal Circularly/Linearly Polarized

µC: Microcontroller

FC: Frequency Counter

FH: Foil Heather

WP: Wollaston Prism

LA: Lock-In Amplifier

SESAM: Semiconductor Saturable Absorber Mirror

BP: Biprism

OSA/MSA: Optical/Microwave Spectrum Analyzer

CCD: Coupled-Charged Device Camera

Abstract

The project developed in this thesis describes the design and the experimental realization of optical methods which can probe the anisotropy of semitransparent media. The ability to manipulate polarized light enables a label-free imaging approach that can retrieve fundamental information about the sample structure without introducing any alteration within it. Such a potential is of great importance and methods like the ones based on polarization analysis are gaining more and more popularity in the biomedical and biophysical fields. Moreover, when they are coupled with fluorescence microscopy and nanoscopy, they may provide an invaluable tool for researchers.

The optical method I developed mainly exploits the laser radiation emitted from tailored optical oscillators to dynamically generate polarization states. The realization of such states does not comprise any external active device. The resulting time-evolving polarization state once properly coupled to an optical system enables probing a sample to retrieve its anisotropies at a fast rate.

The development of two different laser sources is presented together with the characterizations of their optical properties. One of them consists of a Helium-Neon laser modified by applying an external magnetic field to trigger the Zeeman effect in its active medium. The other one is a Dual-Comb source, that is a mode-locked (ML) laser generating a pair of mutually coherent twin beams. Moreover, the thesis delivers the theoretical model and the experimental realization of the optical method to probe the optical anisotropies of specimens. Finally, the technical realization of a custom laser scanning optical microscope and its imaging results obtained with such methods are reported.

Preface

The research for new ways of generating and exploiting light has always played a central role in the development of humankind. In hundred-thousand years, our ancestors have been able to improve such forms of technology from the control of fire to the spreading of electrical illumination. In such a huge time span, optical scientists as Michael Faraday or Pieter Zeeman, who will appear again later on in this thesis, were used to filter specific components of light with a particular set of optical properties matched with the targets of their investigations. Despite the tremendous effort behind this highly inefficient task, they were able to probe nature's secrets by exploiting light. The development of light sources led to the milestone realization of the first working Light Emitting Diodes (LEDs) and lasers in the 20th century [1], [2]. These advancements enabled unprecedented control of generating light with tailored properties, such as power, wavelength, duration, coherence and many others. The impact of these technologies in almost every field of modern society is nearly invaluable. The ever finer and more efficient control of light technologies enabled the advent of the digital era and the reduced impact in the electrical consumption for civil illumination, to reach new insight into the structure of the matter and to sense countless environmental phenomena. It is a naive but not uninspiring thought to wonder about what those scientists from the past could be able to do with such fantastic technological advancements. The improved control over light generation and detection also had an extremely positive impact on life sciences. Several biophotonics instruments have been invented in research labs, providing invaluable tools to biological researchers [3]. Some of these biophotonics technologies also reached the medical field, enriching the diagnostic and therapeutic toolbox for clinical applications [4], [5]. During the last decades, several research groups worked on developing tailored light sources to exploit new imaging schemes rather than optimize the performances of specific imaging methods. It is inspiring to see the amount of extraordinary work done by the laser and microscopy communities in this direction [7], [8]. In addition, we are witnessing the spreading of quantum optical technologies in imaging applications. We can also expect a remarkable impact due to the development of non-classical light sources [9], [10]. The continuous development of photonics technology will bring new opportunities, and we are eager to see how it will further impact the biophotonics and life sciences fields.

During my Ph.D. path, I tried to bring my background and knowledge of laser science and technology to improve the capabilities of multimodal optical microscopes. At that time, I hardly knew the relevance of multimodality in biological imaging and was certainly unaware of the importance of label-free methods. The improvement of a multimodal microscope can provide an invaluable tool to compare the results of label-based and label-free methods evenly, enabling the spread of the latter. Fluorescence-based imaging is one of the most spread approaches to visualize the details of biological specimens at the sub-micrometer scale. The use of exogenous labeling molecules provides high specificity and excellent signal-to-background contrast, motivating the popularity of this method. However, the use of fluorescence microscopy implies some constraints, such as the time-consuming procedure for preparing samples with the proper fluorescent label or the issue of photobleaching. In addition, when dealing with such a small size scale, we cannot neglect the alteration of the biomolecular composition by tagging molecules

whose size is comparable with the structure of interest [6]. Such drawbacks motivate the improvement of state-of-the-art of label-free imaging and the development of a multimodal microscope. Therefore, I couldn't be more enthusiastic when my PI and I agreed on developing a "multi-messenger microscope" illumination stage. In the last three years, we have explored new illumination techniques mainly focused on the dynamic generation of imaging with polarized light. The analysis of the sample-induced alteration of light polarization provides a label-free method that is gaining increasing popularity in biomedical optics applications. Therefore, two main laser technologies I explored for this task are Dual-Frequency, Dual-Polarization (DFDP) lasers and the Dual-Comb Lasers (DCL). As a DFDP laser, I realized a He-Ne laser exploiting the longitudinal Zeeman effect. Then an Yb:CALGO based mode-locked oscillator sustaining two degenerated optical frequency combs has been realized as a DCL. After their realization, I performed optical characterization on both the lasers. Their optical properties have been exploited to performed polarimetric sensing by means of two similar interferometric methods enabled by their characteristic laser emission. Despite the feeling that we have only scratched the surface of such technological advancements, our results are promising and we believed this technology can be widely adopted for optical sensing and imaging.

Organization of this thesis

This thesis is divided into three main sections: the introductory overview of label-free microscopy and light sources commonly used in optical microscopy, the development of custom laser sources for generating polarized light and the characterization of the polarization sensing capabilities aimed at label-free imaging applications.

The first chapter of Section I is devoted to introducing the field of label-free microscopy, highlighting the main optical methods, and going deep into Mueller-Matrix microscopy, the polarization-based imaging technique I studied and implemented. Then, in chapter 2, I give a general review of the several light sources used in optical microscopy, highlighting the impact of research trends in such imaging field and the influence on products developed by laser companies. Each chapter of Section II addresses the development and characterization of a different laser source I worked on and the polarimetric methods to characterize the sample's optical anisotropies. Section III shows the realization of a Mueller matrix microscope and its imaging results. Finally, I dedicate three annexes to going into deep the explanation of the Jones and Stokes-Mueller formalisms I used to model the polarization in such optical setup and the basic concepts of the laser technologies I dealt with during the development of these projects.

References

[1] A. L. Schawlow and C. H. Townes, “Infrared and Optical Masers,” *Phys. Rev.*, vol. 112, no. 6, pp. 1940–1949, Dec. 1958, doi: 10.1103/PhysRev.112.1940.

[2] T. H. MAIMAN, “Stimulated Optical Radiation in Ruby,” *Nature*, vol. 187, no. 4736, pp. 493–494, Aug. 1960, doi: 10.1038/187493a0.

[3] E. Of and N. Of, “Review of Super- Resolution Fluorescence Microscopy for Biology,” pp. 967–980, doi: 10.1366/11-06398.

[4] J. C. Ramella-roman, I. Saytashev, and M. Piccini, “A review of polarization-based imaging technologies for clinical and preclinical.”

[5] G. L. Monroy *et al.*, “Clinical translation of handheld optical coherence tomography : practical considerations and recent advancements Clinical translation of handheld optical coherence tomography : practical considerations and recent,” vol. 22, no. 12, 2023, doi: 10.1117/1.JBO.22.12.121715.

[6] V. Astratov, *Label-Free Super- Resolution Microscopy*. .

[7] C. Xu and F. W. Wise, “Recent advances in fibre lasers for nonlinear microscopy,” *Nat. Photonics*, vol. 7, no. 11, pp. 875–882, 2013, doi: 10.1038/nphoton.2013.284.

[8] C. Lefort, “A review of biomedical multiphoton microscopy and its laser sources,” *J. Phys. D. Appl. Phys.*, vol. 50, no. 42, 2017, doi: 10.1088/1361-6463/aa8050.

[9] G. B. Lemos, V. Borish, G. D. Cole, S. Ramelow, R. Lapkiewicz, and A. Zeilinger, “Quantum imaging with undetected photons,” *Nature*, vol. 512, no. 7515, pp. 409–412, 2014, doi: 10.1038/nature13586.

[10] C. A. Casacio *et al.*, “Quantum-enhanced nonlinear microscopy,” *Nature*, vol. 594, no. June, 2021, doi: 10.1038/s41586-021-03528-w.

I – Introduction and state of the art

1 – Label-Free Microscopy

Optical microscopy is a popular bio-imaging approach exploiting light to probe the chemical, morphological and functional characteristics of living matter. The use of light provides a gentle way to image sample structure and allows to reach magnification of details maintaining high resolution. However, biological specimens are quite transparent to light, so scientists developed several imaging modalities to enhance the contrast in such samples. Modern microscopes exploit different light properties and light-matter interaction mechanisms to overcome such limitations and achieve contrast. In bio-imaging applications, contrast can be achieved by adding some molecular alteration through the proper preparation and treatment of samples. This approach is generally considered a gold standard in bio-imaging. There is a wide variety of labeling strategies and protocols, such as the use of stains in histopathology, the use of dyes or fluorescent antibodies to highlight subcellular structures, or the use of genetically encoded fluorescent proteins. Such approaches, herein called *label-based* methods, are more spread thanks to the high specificity provided by the biochemical labels tagging specific structures in samples. In contrast, such tags may alter the physiological environment inside the specimen and may interfere with the biomolecular processes within it. Another class of methods generate imaging contrast by exploiting the intrinsic optical properties of samples. Such methods are known as *label-free* imaging and would be preferable for studying living matter since they allow to image samples with minimal perturbation and in their more native state. However, such bio-imaging technologies have to fill the gap with the degree of maturity, progress and reliability of label-based methods.

This chapter reviews the main label-free microscopy methods used to investigate the biological world. I will discuss the importance of label-free imaging methods: an overview of the different types of label-free methods is reported in Chapter 1.1. Then, Chapter 1.2 describes the case of Mueller Matrix microscopy as a label-free imaging technique based on light polarization.

1.1 – Overview of label-free methods

The development of optical instruments able to image biological specimens exploiting their intrinsic properties will play a relevant role in life sciences. Different types of light-matter interactions lead to the alteration of different properties of light and such a process can be exploited to generate label-free image contrast. The order and the nature of light-matter interaction provide the criteria for the classifications of these methods. In this section, I restrict the discussion to the all-optical cases, where the physical process behind the contrast origin is only due to the light-matter interaction. However, it is worth mentioning that there are also methods where other forms of energy transfer are involved, for instance, in an acoustic wave or thermal absorption or dissipation.

Light carries information within all its parameters, such as power, phase, wavelength, and polarization. During the interaction with a specimen, some of these quantities may be altered in a distinctive way. The fingerprint of the optical response is impressed on the altered properties of the light and it can be used to generate label-free contrast without altering the sample. Therefore, label-free imaging can be classified on the sample's linear or nonlinear optical response to the illuminating beam. When an electromagnetic field interacts with a dielectric

medium, it alters the local distribution of charges of its atoms and molecules. The polarizability relation in eq. 1 links the medium response related to its dielectric susceptibility tensor $(\chi^{(n)})$ to the electric field $\left(\overrightarrow{E^n}\right)$ of the impinging beam.

Eq. 1) $\vec{P} = \overrightarrow{P_L} + \overrightarrow{P_{NL}} = \epsilon_0 \sum_n \chi^{(n)} \overrightarrow{E^n}$

where n is the order of the medium optical response. Linear label-free imaging involves alteration of the quantities appearing in eq. 1 by truncating the series expansion at $n = 1$, which means considering only the contribution of $\overrightarrow{P_L}$. Such methods exploit contrast based on phase, polarization or directional properties of light or a combination of them. Since they are based on the linear component of the specimen optical response, a low light level is generally required to generate label-free images with such methods.

Among phase-based techniques, the most popular ones are phase contrast microscopy (PCM), differential interference contrast (DIC) and quantitative phase microscopy (QPM). Such techniques have been among the first ever developed label-free methods and are also widely adopted because of their relative simplicity and consequent integrability in a standard optical microscope. Since biological specimens typically exhibit low absorption, phase-based imaging methods exploit their structure's spatial differences in thickness and refractive index distribution. Indeed, the differences in the optical path length experienced by light while it travels through the sample lead to the phase-based contrast. So, these methods need a phase structuring of the input beam and the spatial interference between components with different phase shifts transduce the sample phase signature into light intensity differences. This technique is suitable to be implemented both in widefield and scanning imaging configurations and provides label-free images at high spatiotemporal resolution. Such characteristics allow to image the morphological features of the sample, which is useful in several basic science and medical applications.

Light components scattered during light-matter interaction are the source of the label-free signal used to form images in a dark-field microscope. This method allows for a substantial reduction of the background by blocking the light waves with a partially opaque mask. Thus, only the presence of a scatterer deviates light components, overcoming the mask and becoming useful for image generation. A modern implementation of this imaging modality uses metallic nanoparticles as labeling agents to enhance signal generation in samples, weakening the concept of label-free technique in return for higher contrast [1].

In polarization imaging, an alteration of the polarization state caused by optical anisotropies is projected as an intensity variation and exploited to generate the label-free contrast [2]. Therefore, the vectorial description of the light and medium properties is necessary. If the light-matter interaction involves an isotropic material, the linear susceptibility component $(\chi^{(1)})$ can be assumed as a scalar. Anisotropy materials instead require a more complex description where $\chi^{(1)}$ is a 3-dimensional tensor. The values of such tensor, linked to the refractive index of the medium, depending upon the vibration direction of the light. Thus, anisotropy in the real part of the tensor elements describes those materials introducing a different delay to light components

with different polarizations: such material property is called phase anisotropy (or retardance or birefringence). As its name suggests, the same light beam experience a double refraction that depends upon the relative orientation of light polarization and the optical axes of the medium. Anisotropies may also be related to the dichroism that is the differential response of the sample with respect to the field amplitude of orthogonally polarized light components. Here, the anisotropy lies in the imaginary part of the dielectric tensor thus, different polarization states experience different attenuation [3]. Both birefringence and dichroism properties of specimens can be used to generate label-free images. Section 1.2 deals with a more complete discussion of the imaging technologies employed in polarized light microscopy.

Nonlinear microscopy (NLM) is described by taking into account also the contribution of $\overrightarrow{P_{NL}}$ in eq.1. These methods typically require high-intensity ultrashort laser pulses since the medium's nonlinear optical (NLO) response depends on the excitation of higher-order terms of the polarizability vector. Therefore, the light dose required to trigger nonlinear contrast is typically higher than that demanded by linear methods. On the other hand, the NLO process leads to frequency conversion, so the separation of the excitation beam and the converted light is typically easier and implemented employing dichroic mirrors and optical filters. Several NLO processes can be triggered in the samples, depending upon their structure and chemical composition [4]–[6].

For instance, nonlinear coherent scattering processes following higher harmonic generation are often exploited to develop label-free microscopes. Second Harmonic Generation (SHG) and Sum Frequency Generation (SFG) are second-order nonlinear optical processes triggered by the simultaneous interaction of the photons in a nonlinear medium [7]. During these processes, the frequency of the nonlinear signal is the sum of those of impinging photons. Such interactions have place when the centrosymmetric molecular structure is broken. Several biological materials such as collagen, cellulose, microtubules or myosin have been imaged with such microscopy methods. Moreover, polarization-resolved SHG imaging also provides an excellent tool for defining the orientations of the signal sources because the generation of nonlinear signals is typically strongly anisotropic. Another method based on harmonic generation is Third Harmonic Generation (THG) imaging. Here, a molecule virtually absorbs three photons and its nonlinear response generates a new photon with tripled optical frequency, i.e. energy. Conversely to SHG, this process is not sensitive to a specific asymmetry of the medium structure. THG imaging allows probing the presence of water-lipid and water-protein interfaces, allowing to image of cellular membranes and extracellular matrix structures [8].

Among the methods exploiting third-order nonlinear effects, Coherent Raman Microscopy (CRM) has a special role in nonlinear label-free imaging. The excitation of Raman signals links the vibrational modes associated with the characteristics of a specific chemical bond to the spectral content of the nonlinear response. Therefore, these vibrational transitions can be used as a fingerprint of the presence of certain molecular species. Thus, the sample response may provide a distinctive fingerprint of its chemical composition [9]. First, Raman microscopes had an extremely long acquisition time as main drawback because of the small amount of spontaneous Raman signal triggered in the specimens. However, the development of methods based on

stimulated Raman signals overcame this limitation, paving the way for spreading such imaging methods. This class of methods includes several techniques, such as Stimulated Raman Scattering (SRS) and Coherent Anti-Stokes Raman Scattering (CARS) [5], [9]. In such methods, spectral components of the excitation light are properly generated, attenuated or amplified by the nonlinear light-matter interaction. The detection of such amplitude variation in the detected spectra can be used to map the Raman-based contrast. Hence, such methods often involve hyperspectral analysis of the light re-emitted by the specimens. CRM is a promising label-free approach for a plethora of applications, from label-free histology to pharmaceutical research.

Time-resolved spectroscopy techniques, such as pump-probe spectroscopy, inspired another interesting NLO imaging method [10]. As in the other nonlinear cases, pump-probe imaging requires high peak intensity, but two different pulsed lasers are required in this case. A first beam, called pump, excites an intensity-dependent variation in the photophysical properties of the sample through a nonlinear absorption process. Then, a second beam records these variations by experiencing a different transmission through the sample. Such probe beam is less intense than the pump, in order to neglect its perturbation on the sample properties. Then, these mechanisms are observed by modifying the delay between the arrival time of the pump and probe pulses. Therefore, this method allows to image dynamic variations in the sample structure, such as the relaxation dynamics of the nonlinear properties as a consequence of the pump excitation. Moreover, nonlinear absorption is exhibited without the need for any labels: the nonlinear nature of the mechanism links the optical response to the intrinsic properties of the sample. Pump-probe methods enable the observation of non-fluorescent regions in specimens since the contrast is due to the transient absorption changes induced by nonlinear absorption processes.

The panorama of the label-free imaging methods is even wider than the brief overview I made above. The different physical mechanisms behind them provide complementary information about biological specimens, possibly allowing a complete observation of their inner structure. In addition, the parallel development of optical microscopes with resolution approaching the molecular scale emphasizes the need for improvement in state-of-the-art label-free technologies. Moreover, the improvement of the optical performances, such as the higher resolution or faster acquisition speed, as well as the increased compactness of the optical instruments, helps the spreading of such imaging technologies.

1.2 – Mueller Matrix Microscopy

In the last decades, scientists developed several polarization-based sensing techniques and imaging methods [11]–[13]. Such approaches are known as polarimetric techniques. They rely on the Jones and Stokes-Mueller formalism (see Annex A) for describing the polarization states and their interactions with anisotropic media. Among these approaches, Mueller Matrix imaging is the most comprehensive polarization-resolved technique that provides label-free contrast based on specimen anisotropies. The morphological and conformational properties of sample structures, as well as their size and orientations, influence the alteration of polarized light. So, the label-free contrast related to optical anisotropies and microscopy images can be obtained using only the sample's intrinsic properties. Mueller coefficients can be used as map where the

imaging contrast is associated with the value of the coefficient itself. The identification of several Mueller elements provides several label-free images of the same object, making the Mueller microscopy an approach intrinsically multimodal. The values of different Mueller coefficients are influenced by different optical anisotropies from the sample. For instance, m_{14} coefficient of the Mueller matrix is associated to the Circular Dichroism (CD) and to the Circular Intensity Differential Scattering (CIDS). The first quantity expresses the differential absorption with the respect of light components with different states of circularly polarized light, namely circular left and right. CIDS instead is linked to the differential value of the intensity of the scattered light with orthogonal components of circularly polarized light. The chiral organization of molecules, such as chromatin in cell nuclei, is sensitive to this type of anisotropy [14]–[16]. So, the analysis of the scattered intensity contained in circularly polarized light components is an interesting label-free method for studying this type of molecular structures. Similarly, the linear and regular organization of tissues, such as collagen-rich areas in muscles and tendons, is sensitive to the elements of the Matrix related to the linear birefringence and dichroism. Mueller matrix microscopy has been applied to image collagen, mitotic cell division, ophthalmology, brain tissues, and many other areas [17].

The Mueller matrix of a sample fully describes its optical anisotropies and its identification enables to form 16 images. Indeed, since each Mueller coefficient is associated with a specific component of the anisotropy, such imaging method is intrinsically multimodal. The Mueller matrix is identified by shining the sample with different states of polarized light and detecting their alterations. Different polarizations can be modified in a distinctive way by sample anisotropies, so, the variation of such states is recorded. Therefore, several input polarization states and several intensity projections of polarized components are needed to obtain information about all the Mueller coefficients. Fig.1 shows a simple block scheme describing the general architecture of a setup used for characterizing the Mueller matrix of a sample.

Figure 1 - The PSG stage generates the proper light polarization (grey double-sided arrow). The output polarization state is altered if the sample contains any anisotropy (grey ellipsoidal arrow). The PSA analyzes such alterations by projecting the intensities associated with different polarization components onto a pre-determined basis.

Here, a Polarization State Generator (PSG) is employed to generate different states of polarized light, whereas the detection of their alteration is performed through the Polarization State Analyzer (PSA) [18]. Thus, modifications of polarized light are converted into intensity contrast by projecting the states onto a certain polarization basis. Such stages are typically realized by using polarization optics such as linear polarizers (LP) and birefringent waveplates (half, HWP and quarter, QWP). These optical elements are passive devices exhibiting strong and tailored levels of polarization dichroism and birefringence. Through their use, the polarization states can be generated or analyzed in a static way that depends on the relative orientation of their optical

axis and the input polarization state. Apart from these two stages, a polarized light microscope shares most of the elements in its setup with an ordinary optical microscope. A significant concern should come if other elements are altering the polarization properties of light, such as other polarizers or waveplates, dichroic mirrors, or optical elements with residual mechanical stress.

There are several generation and analysis strategies in terms of multiplexing the polarization information and probe the sample with different states. The main approaches exploit spectral, spatial or temporal multiplexing of the polarization states. The use of array detectors, in combination with other optical elements, allows the implementation of all these strategies. However, when dealing with laser scanning microscopy, a single-element detector is typically the preferred choice to collect the light. These devices introduce a constraint in choosing the encoding strategy of the polarization states since both the spatial and spectral information are averaged across its sensitive area. Therefore, the possibility to address different polarization state to different spectral regions or spatial modes of the light is hindered. Then, a typical choice is to exploit the generation of different polarization states in time to perform Mueller matrix imaging in a laser scanning microscope. I focus the discussion on those methods compatible with the characteristics of a laser-scanning microscope since it is the architecture of the imaging system adopted in the projects developed in this these. The temporal generation of polarized light is a widely adopted approach also used in many optical setups exploiting an external device to perform the function of PSG. The single-element detector employed in such microscopy configuration may provide high temporal resolution, but it averages the spatial structure of the beam and the spectral information in the optical range. Therefore, a polarization laser-scanning microscope requires fast generation rates from a PSG stage that matches the scanning system's pixel dwell time [17]. Typically, devices used as PSG behaves as electronically-controlled polarization optics: their anisotropy properties changes in time following the trigger of some driving signal [19]. The simplest and more complete way to dynamically generate the polarization states is by means of three polarization optics mounted on mechanical holders with a rotational degree of freedom. The main limitation coming from using passive optics is the slowness, which may lead to excessively long imaging acquisition time. However, other devices allow to achieve the polarization generation and analysis tasks in a more effective way, but at the expense of the cost, simplicity and compactness of the optical setup. Table 1 reports some of these devices: it is worth noting that the same technology can be used both for the dynamic generation and analysis of polarization states in time. So, their function in the optical setup also depends on if they are located before (PSG) or after (PSA) the specimen.

	Physical Mechanism	Generation Rate	Strengths	Weakness
Rotating Polarization Optics (LP + HWP + QWP)	Intrinsic dichroism and birefringence + mechanical rotation	~ Hz	Cheap cost Broadband PSG	Relatively cheap Slow
Liquid Crystals Modulators (LCM)	Electric field-induced orientation of birefringent molecule chains	< kHz	Broadband PSG	Relatively cheap Slow
Photoelastic modulators (PEM)	Photoelastic effect: birefringence induced by mechanical stress	50-100 kHz	Relatively fast Broadband PSG	Expensive Optical Alignment
Electro-optic modulators (EOM)	Electro-optic effect: birefringence induced by electric field	few MHz	Very fast	Expensive High-Voltage Driving Optical Alignment

Table 1 - List of some active devices commonly used to control e analyze the state of polarization light in time.

A common negative aspect is that their implementation relies on using a bulky device with its own power and controlling electronics that may require a delicate optical alignment. Moreover, an illumination stage is obviously also necessary in the microscopy setups since these devices are not able to generate light, but they only manipulate its polarization states. Therefore, a significant simplification and improved usability of these imaging technologies would come by developing a light source able to dynamically generate light with structured polarization states. Such results would simplify the coupling with other imaging approaches, paving the way for developing a more compact multimodal imaging platform.

References

[1] P. F. Gao, G. Lei, and C. Z. Huang, "Dark-Field Microscopy: Recent Advances in Accurate Analysis and Emerging Applications," 2021, doi: 10.1021/acs.analchem.0c04390.

[2] S. Inoué, "An Introduction to Biological Polarization Microscopy," in *Collected Works of Shinya Inoué*, WORLD SCIENTIFIC, 2008, pp. 503–536.

[3] O. A. Barriel, "Mueller matrix polarimetry of anisotropic chiral media," 2010.

[4] A. Diaspro *et al.*, "Two-Photon Excitation Fluorescence Microscopy," in *Science of Microscopy*, P. W. Hawkes and J. C. H. Spence, Eds. New York, NY: Springer New York, 2007, pp. 751–789.

[5] S. Yue, M. N. Slipchenko, and J. X. Cheng, "Multimodal nonlinear optical microscopy," *Laser Photonics Rev.*, vol. 5, no. 4, pp. 496–512, 2011, doi: 10.1002/lpor.201000027.

[6] R. Cicchi and F. S. Pavone, "Multimodal nonlinear microscopy : A powerful label-free method for supporting standard diagnostics on biological tissues," vol. 7, no. 5, pp. 1–16, 2014, doi: 10.1142/S1793545813300085.

[7] P. J. Campagnola and L. M. Loew, "Second-harmonic imaging microscopy for visualizing biomolecular arrays in cells , tissues and organisms," vol. 21, no. 11, pp. 1356–1360, 2003, doi: 10.1038/nbt894.

[8] B. Weigelin, G. Bakker, and P. Friedl, "Third harmonic generation microscopy of cells and tissue organization," vol. c, pp. 245–255, 2016, doi: 10.1242/jcs.152272.

[9] R. Vanna *et al.*, "Vibrational imaging for label-free cancer diagnosis and classification," *La Riv. del*

Nuovo Cim., vol. 45, no. 2, pp. 107–187, 2022, doi: 10.1007/s40766-021-00027-6.
[10] T. Ye, D. Fu, and W. S. Warren, "Invited Review Nonlinear Absorption Microscopy †," pp. 631–645, 2009.
[11] V. V. Tuchin, L. V. Wang, and D. A. Zimnyakov, *Optical Polarization in Biomedical Applications*, vol. 0, no. 93. Berlin, Heidelberg: Springer Berlin Heidelberg, 2006.
[12] N. Ghosh, "Tissue polarimetry: concepts, challenges, applications, and outlook," *J. Biomed. Opt.*, vol. 16, no. 11, p. 110801, Nov. 2011, doi: 10.1117/1.3652896.
[13] J. C. Ramella-roman, *Polarized Light in Biomedical Imaging and Sensing*. Cham: Springer International Publishing, 2023.
[14] A. Diaspro, M. Bertolotto, L. Vergani, and C. Nicolini, "Polarized light scattering of nucleosomes and polynucleosomes-in situ and in vitro studies," *IEEE Trans. Biomed. Eng.*, vol. 38, no. 7, pp. 670–678, Jul. 1991, doi: 10.1109/10.83568.
[15] A. Diaspro, G. Radicchi, and C. Nicolini, "Polarized light scattering: a biophysical method for studying bacterial cells," *IEEE Trans. Biomed. Eng.*, vol. 42, no. 10, pp. 1038–1043, 1995, doi: 10.1109/10.464379.
[16] A. Le Gratiet *et al.*, "Circular intensity differential scattering (CIDS) scanning microscopy to image chromatin-DNA nuclear organization," *OSA Contin.*, vol. 1, no. 3, p. 1068, Nov. 2018, doi: 10.1364/OSAC.1.001068.
[17] A. Le Gratiet, A. Mohebi, F. Callegari, P. Bianchini, and A. Diaspro, "Review on complete mueller matrix optical scanning microscopy imaging," *Appl. Sci.*, vol. 11, no. 4, pp. 1–18, 2021, doi: 10.3390/app11041632.
[18] H. Fujiwara, *Spectroscopic Ellipsometry*. Wiley, 2007.
[19] J. C. Kemp, "Piezo-Optical Birefringence Modulators: New Use for a Long-Known Effect," *J. Opt. Soc. Am.*, vol. 59, no. 8, pp. 950–954, Aug. 1969, doi: 10.1364/JOSA.59.000950.

2 – Light Sources in Optical Microscopy

This chapter aims to highlight the state of the art of light sources mainly employed in Optical Microscopy. Most common approaches and research trends are reviewed and classified by the light generation technology. Section 3.1 deals with the state-of-the-art of more traditional microscopy light sources, typically exploited in widefield brightfield microscopy. Then, Section 3.2 describes the most popular laser technologies used in microscopes with scanning architectures.

2.1 – Illumination stage in an optical microscope

An optical microscope is a powerful tool for studying biological systems and its evolution has also been possible thanks to the advancements in its light sources. Light allows the observation of sample characteristics with minimal invasiveness and perturbation. Also, several light properties can be used to exchange information with the specimen structures, providing a wide variety of methods to probe them. So, the illumination source is one of the primary key stages of the microscope architecture. Thermal light from the sun or candle flames has been used to illuminate the sample for centuries. This simple type of illumination exploited transmission inhomogeneity in samples structure to form a contrast and reveal their inner structures. Significant advancements came from introducing more sophisticated artificial light sources emitting in the visible (VIS) range and suitable for brightfield illumination. Incandescent lamps made with tungsten and/or halogens have been used to send light in the optical microscopes in a more controlled way. This source exploits the light emission produced when a resistive filament is heated and an electric current travels through it. This process generates a black-body-like continuous spectrum across the visible spectrum, although most of the photons are emitted in the infrared (IR) range. However, these lamps are not prone to fast switching operation dynamics and the thermal management of the electric current dissipation bounds their output power. Moreover, since most of their emission is in the infrared, only a tiny portion of the output light is actually valuable for shining the specimens. So, the IR components must be filtered out to avoid useless sample heating. Other light sources widely used in fluorescence microscopy are discharge arc lamps made with xenon or high-pressure mercury. These devices exploit the light emission produced by plasma generated through the electrical breakdown in a high-pressure gas contained between two conductive electrodes. These lamps are brighter than incandescent sources and their typical spectral emission contains several spectral lines, mainly in the visible and the ultraviolet (UV) spectral regions. Thus, mercury lamps provide an efficient way to generate light with shorter wavelengths. These lamps are suitable for applications where their discrete-like spectrum can be effectively exploited, for instance, to match the absorption spectra of fluorophores. On the other side, xenon lamps produce a more uniform white light spectrum. Both these technologies require high voltage power supply, and their light bulb is a hazardous waste that needs careful handling to avoid breaking. Further, light bulbs have a slow warm-up time, and their lifetime is relatively short (around 200 hours for mercury and 1000 hours for xenon lamps). Metal halide lamps overcome many of these issues. Also, these lamps generate light through an arc discharge but most of the spectral peaks they emit are in the visible range, resulting in lower unwanted heating. Even if these lamps are typically more

expensive than mercury and xenon lamps, they have better emission stability in time and a longer lifetime (2000 hours). These lamps are often combined with liquid light guides to provide uniform and homogeneous light sources with decreased spatial and temporal coherence. The introduction of light-emitting diodes (LEDs) sources outperformed these devices that have been replaced in many of their traditional microscopy applications. The main advantages of LEDs over lamps are lower power consumption, longer operational lifetime, stability, higher compactness, and cheaper cost. Moreover, LEDs emit relatively narrow spectral lines, typically matched with fluorophores absorption bands. Thus, heat dissipation on the sample is minimized and white light generation remains still possible by combining different LED devices or using phosphorous-based sources. However, the advent of laser sources in the 60s brought one of the most disruptive innovations in the field of microscopy. Since then, microscopists have realized countless optical schemes and imaging methods exploiting the peculiar properties of these light sources.

2.2 - Laser sources for microscopy

The introduction of laser revolutionized optical microscopy by providing a monochromatic, highly stable, and intense light source for imaging, with great room for customization and tailoring of its optical properties. Some of the first and most successful laser-based microscopy techniques were the confocal laser scanning microscope (LSM) and the multiphoton microscope (MPM). In such microscopy techniques, the laser light is focused on a sample in a diffraction-limited spot. Light-matter interaction alters radiation properties and then these alterations are recorded for each point of the scanning area. The advantages of laser-based microscopy include increased resolution and contrast, minimal spatial crosstalk, reduced photobleaching, and the optimization of the photon budget. These advantages have led to the development of a wide range of laser-based microscopy techniques, each with unique features and applications. Later advances in laser technology have enabled new capabilities in optical microscopy, as well as new imaging modalities and improved optical performances.

Both gas and dye lasers were relevant in developing the earliest laser scanning microscopes. However, these devices have been replaced by more modern laser technology in most of their traditional microscopy application nowadays. In gas lasers, the active medium is a mixture of ionized gases, typically noble gases, such as helium, neon, argon and krypton. The pumping mechanism usually involves flowing an electrical current through the medium following the gas ionization. A standard helium-neon laser at 632.8 nm has been employed in the first realization of a confocal laser scanning microscope [1]. The first fluorescent confocal LSM exploited a helium-cadmium beam at 441.6 nm to excite fluorescence in cells stained with fluorescein isothiocyanate [2]. A dye laser instead exploits an organic dye containing a chromophore to achieve optical amplification and thus, the lasing action. Such active media are often realized as a liquid solution, decays in time and the liquid solution must be replaced. Moreover, these solutions contain volatile and toxic solvents that make the handling of these devices complex. A dye laser has a broadband emission spectrum, allowing the realization of a tunable light beam or the generation of ultrashort pulses. Nowadays, dye lasers are not widely employed, but these devices have been used in many spectroscopy applications and in the development of the

earliest laser scanning microscopes, the first pioneering applications of confocal fluorescence, two-photon fluorescence and Raman microscopy [3]–[5].

Semiconductor laser diodes (SLDs) are a very popular choice in optical microscopy due to their low cost, and high reliability and their small footprint helped their integration into microscope systems. SLDs have a wide range of emission wavelengths from the UV to IR and are commonly used in many fluorescence-based techniques, such as confocal and fluorescence lifetime microscopy (FLIM). The characteristics of their spectral emission depend upon the semiconductor materials used for their fabrication. Traditional semiconductor materials are gallium arsenide (GaAs) and indium phosphide (InP), which typically cover the red/near-infrared window. Since the 90s, the use of gallium nitride (GaN) also allowed the realization of efficient SLD laser emitting at bluer wavelengths [6], [7]. Therefore, multi-wavelength laser systems are becoming increasingly popular in optical microscopy due to their ability to provide several excitation wavelengths in a single compact device. These systems typically consist of several laser diodes, each emitting at a different wavelength. This multispectral emission allows for the simultaneous excitation of several fluorescent probes or the use of various imaging approaches in a single experiment, improving the efficiency and speed of imaging experiments. Direct driving through the injecting of electrical current is one of their most significant advantages since it allows power level modulation and tailoring of the temporal profile of their emission. Such devices can emit both continuous-wave (CW), modulated and pulsed optical radiation with the proper electronic driver [8]. Most other laser technology (gas, solid-state, fibers) requires an external device to achieve intensity modulation, typically an acousto-optical or an electro-optical modulator (AOM/EOM).

Solid-state lasers have been widely used in many applications in both industrial and research fields thanks to their high-power output, low intensity noise, and great versatility in performance tailoring. Laser companies have a commercial interest in developing more compact, reliable, cost-effective sources with a broader range of wavelengths and increasingly higher power levels. Moreover, both CW and pulsed emission, with a duration ranging from nanosecond down to femtosecond, can be realized through this technology. Especially the development and the spreading of turn-key ultrafast lasers, which produce pulses of light with extremely short duration (on the order of pico- or femtoseconds) leads to the rise of nonlinear label-free methods. The research field focuses on developing novel laser schemes, scaling performance, and looking for new reliable laser materials. The most commonly used solid-state laser technologies in optical microscopy include titanium-sapphire lasers (Ti:Sa) and diode-pumped solid-state lasers (DPSSL). The core component of these devices is a solid material (both glass and crystal) where the optical transition is offered by rare-earth ions doping such hosting media. These active materials typically have absorption and emission bands in the NIR region, so they are commonly used to generate infrared beams. Such spectral features perfectly match the needs of MPM and NLM since they require excitation in this spectral range. Another common approach is to use DPSSL to seed nonlinear optical conversion stages: doing so, the visible and ultraviolet ranges [9] can be achieved and the spectral coverage is extended to match fluorophore absorption. However, many rare-earth ions also generate fluorescence in the VIS

after absorbing light in the blue. Such spectral features have not been traditionally exploited due to a lack of efficient, compact, and practical pump sources in these wavelength windows. Therefore, the evolution of DPSSL technology certainly benefitted from the development of new laser diodes in terms of both available power levels and wavelengths [10], [11]. The improvement of diode laser technology, as the realization and the power scaling of diodes emitting in the blue region [6], opened new possibilities for DPSSL pumping. Such developments allow us to revise active media based on rare-earth were used. The new class of pump diodes has been successfully employed to realize DPSSL directly emitting in the visible [12]–[15]. Moreover, these devices can still exploit nonlinear conversion to extend their spectral coverage and reach more efficiently the laser emission in the deep-UV range [16].

Ti:Sa crystals can be used to realize both widely tunable CW lasers and ultrashort pulses with a duration shorter than 100 fs, with an emission band between 700 and 1000 nm [17]. These characteristics make it a classical source for nonlinear and multiphoton imaging, where high peak powers and NIR emission are required [18]. However, a Ti:Sa laser is quite a complex and expensive device characterized by a bulky pumping stage. Indeed, it is typically realized with a frequency-doubled DPSSL because of the lacking of performing sources directly emitting in its absorption band in the blue-green window. Recently, the performance improvements of green/blue laser diodes and LEDs allowed to simplify the pumping stage architecture, thus enabling the development of more compact Ti:Sa oscillators [17], [19], [20].

Many systems also incorporate a solid-state laser for pumping an optical parametric oscillator (OPO) and amplifier (OPA) in tandem. Such devices are an ideal source for many spectroscopy and microscopy applications thanks to their wide tunability range, high peak power and ultrashort pulse duration. The core element of these devices is a conversion process realized in a nonlinear crystal. However, these sources are quite bulky and power-consuming, but many microscopy applications still exploit their optical performances to realize advanced nonlinear imaging applications [9], [21]–[23]. As for the Ti:Sa lasers, a significant effort has been put into developing OPO with lower complexity and smaller footprint. The advent of engineered nonlinear optical crystals allowed to relax of the phase-matching constraints in the nonlinear process and achieving a greater conversion efficiency [24], [25]. So, a great variety of tailoring possibilities of nonlinear conversion have been enabled. This technological improvement positively influenced the development of nonlinear optical light sources, such as OPO and OPA. A great effort in realizing more compact and efficient devices is opening new application possibilities for these devices [26]–[29].

The enormous popularity of fiber lasers in research and industrial applications makes them one of the most exciting and disruptive technologies in this field. Thanks to their unique properties, they have emerged as an essential tool, providing many advantages over other laser sources. Indeed, fiber lasers owe their success to several aspects, such as the possibility of having a very compact and robust ultrafast laser source with great versatility in tailoring its optical emission. In addition, they are relatively inexpensive and allow for long-term, continuous operation with minimal maintenance. In-fiber optical oscillator reduces the constraints of the optical alignment and allows for keeping the device footprint compact without sacrificing the

cavity length. So, the long interaction length and the small core size where the radiation is confined increase the accessible optical gain. Moreover, easier heat management supports scaling up the output power level and consequently, the relaxation of cooling requirements allows them to keep their footprint compact [30]. All these aspects enable their easy integration into more complex laser systems and instruments, such as optical microscopes [31]. As for the case of solid-state lasers, the typical spectral bands emitted by fiber lasers are in the NIR. So, they are effectively used to match the absorption band of most fluorophores used in MPF microscopy and in applications where the high penetration depth is preferable. Also, the classification of fiber lasers can be based on the type of active medium used in the laser cavity. Rare-earth doped fibers are the gain media used for these devices and the most common dopants are ytterbium (Yb) and erbium (Er). Both these active fibers can produce laser output with high peak power and picosecond/femtosecond ultrashort pulses. The spectral emission of Yb-doped fibers is around 1050 nm whereas those based on Erbium emits at 1550 nm. Also here, conversion stages based on nonlinear process enable wavelength extension. Particularly, the interest in MPM stimulate to reach laser emission toward longer wavelengths, thus reducing the impact of tissue scattering and increasing the penetration depth [32].

As already pointed out, one of the major efforts in developing laser technologies is the achievement of different spectral ranges. Thus, another significant development in laser technology has been the development of white light lasers (WLL, also known as supercontinuum lasers), which generate a broad spectrum of laser light. WLLs are widely used in many spectroscopy and imaging applications because they are powerful broadband light sources with a relatively simple architecture and compact footprint. These lasers emit a wide range of wavelengths, from ultraviolet to infrared, making them suitable for various imaging techniques. This facilitates researchers to perform multispectral imaging, in which different wavelengths are used to image multiple fluorophores simultaneously [33]–[35]. There are two main types of supercontinuum lasers: fiber-based and crystal-based. Fiber-based supercontinuum lasers are generated by cascading nonlinear optical processes in a specialized optical fiber called photonic crystal fibers (PCF). Alternatively, high-energy pulses also allow supercontinuum generation in bulk crystals [36]. Both types of supercontinuum lasers have high power output, broad spectral range, and good beam quality. These sources typically require spectral filtering for wavelength selection. A typical configuration includes an acousto-optical tunable filter (AOTF) for fast color tuning [37], [38].

In this chapter, I reviewed both industrial and research trends on the main laser technologies. The use of laser sources in optical microscopy has dramatically improved the capabilities of this important imaging field. With new laser technologies constantly emerging, the advances in laser technology will likely continue to shape the future of biophotonics applications in life sciences. Beyond the specific approach to laser development, it is clear that most of the improvements involved only some light properties. In particular, considerable efforts have been put into increasing the output power levels, controlling the pulse duration and duty cycle, shifting the spectral emission, or reducing the noise. Meanwhile, the quality of the other performances, such as beam quality, emission stability and device reliability, has to be maintained. I dedicate a separate section to discussing the polarization role in laser sources. Tailoring of polarization

has deserved a significantly lower amount of work, providing so more room for improvement in such a task. The vast majority of the laser source produces a linear state of polarized light that is solely characterized by its orientation and Polarization Extinction Ratio (PER), which is the ratio of optical powers in the two main orthogonal directions of the beam electric field. A combination of anisotropy factors determines the polarization emission depending on the active medium and the other resonator elements. So, the vectorial properties of the electromagnetic field emitted by most sources are constant and fixed in time, even if slight variations may occur due to thermal drifting or similar phenomena. However, methods to generate a structured state of polarized light exist, whether the polarization variation depends upon the wavelength [39], time [40] or spatial properties [41] of the laser beam. Therefore, I concentrated my efforts on studying, developing and using lasers with a dynamic emission of the polarization state because of their potential application and compatibility with laser scanning microscopy.

2.3 – Laser sources for polarization microscopy

Here, I describe the laser technologies that generate a light beam with a time-evolving polarization state. The development of such devices may help spread sensing applications where fast polarization shaping is relevant. Several light microscopy methods, as some of those discussed in Section 2, may benefit from such advancement. Light polarization has a fundamental role in application as fluorescence anisotropy imaging, label-free polarization-based method, and nonlinear optical approaches. If adequately tailored, laser-scanning microscopy can benefit from such a feature because such a fast generation rate can effectively match the time constraints introduced by scanning imaging. In addition, the spreading of laser sources with such polarization feature enable the realization of these imaging instruments avoiding external active devices to shape the polarization state. Section 2 already discussed the devices traditionally used in Mueller Matrix microscopy for shaping the polarization states. Traditionally, the generation of polarized light has place outside the laser cavity, sending the light to an optical component that may act as an electronically controlled birefringent waveplate or polarizer.

During the design of a laser oscillator, the anisotropy of its optical elements has to be considered. The active medium may have polarization-dependence in both absorption and emission spectra, as in the case of Ti:Sa, Yb:CALGO or Nd:YVO4 crystals. In such a case, it may be convenient to align the polarization plane of the pump light to the axis where the absorption spectrum has a maximum. In addition, the design should consider the presence of intracavity elements introducing an attenuation depending upon the polarization direction to minimize the cavity losses. Such elements may be a polarizer acting as an output coupler, a Brewster plate to increase the PER of the emitted radiation or a birefringent element for nonlinear conversion or optical switching. The overall balance between the active optical gain and resonator losses determines the polarization properties of the laser output beam. Annex A.1 shows the Jones formalism that is typically used to describe the polarization state of the electromagnetic field. Such a formalism is also used to model the resonator anisotropy properties and the evolution of polarized light within it [42], [43]. As anticipated, commercial laser sources typically do not

provide sophisticated tailoring of polarization properties. In many cases, developing such sources involves reducing unwanted depolarization mechanisms to maximize the laser output power. However, in some applications, the laser design allows multiplexing the oscillating radiation and generating a more complex output state of polarized light.

The two main laser technologies I explored for this task are Dual-Frequency, Dual-Polarization (DFDP) lasers and the Dual-Comb Lasers (DCL). Before introducing them, I want to recall few fundamental concepts about laser science. An optical resonator sustains the oscillation of discrete frequencies with a very narrow linewidth. Such lines are the cavity's longitudinal modes, and their frequency spacing is called Free Spectral Range (FSR). The roundtrip time is the inverse of the FSR and represents the time the oscillating light needs to cover a whole roundtrip inside the resonator.

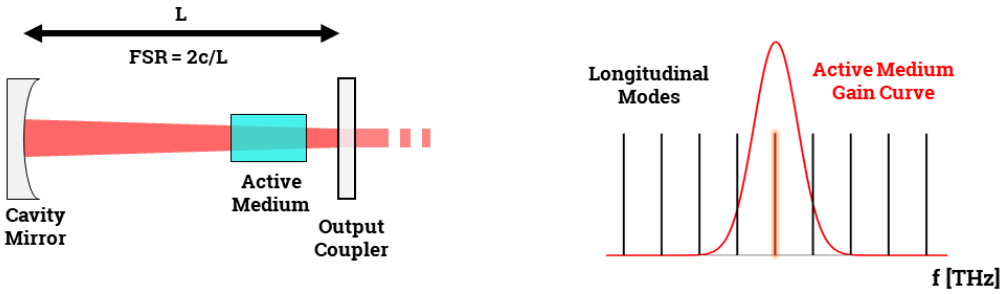

Figure 2 - On the left, a representation of a simple laser with a straight resonator. On the right is its output spectrum: if the cavity is short enough (L), the frequency spacing between its longitudinal modes (black lines) is such that only one of them (glowing red line) falls below the peak of the active medium gain curve (red line) and oscillates.

2.3.1 - Dual-Frequency, Dual-Polarization (DFDP) Lasers

A DFDP laser emits two orthogonally polarized beams with a slightly different frequency differences. There are two main methods to generate such crossed-polarized radiation: one implies splitting the active medium's gain line by means of the Zeeman Effect. The most popular device employing this mechanism is the Zeeman Laser (ZL, sometimes called Z-lasers). In this case, the anisotropy effect arises directly in the process of generating light since it involves the interaction between the magnetic field and the active atoms. The Zeeman effect has been mainly exploited in gas lasers by applying to their active medium an external magnetic field. The transfer of energy from the magnetic field to the atomic structure of the active medium causes the splitting of such energy levels. Two laser lines with slightly different optical frequencies oscillate if this active medium is put inside an optical resonator. These lines are associated with the split levels and the frequency difference is inherently related to the amount of energy difference between such levels [44], [45]. This process forms two frequency-shifted gain lines in the active medium, generating two laser lines with orthogonal polarizations. Therefore, a Zeeman laser generates two linear orthogonal or two circular orthogonal states of polarized light, depending on the magnetic field orientation with respect of the cavity axis. When the field is applied perpendicularly to the cavity axis, the crossed-polarized states are linear and this device is called Transverse-effect Zeeman Laser [46]. Conversely, a Longitudinal or Axial

Zeeman-effect Laser emits two orthogonal counter-rotating circularly polarized components by applying a magnetic field parallel to the optical axis [40], [47].

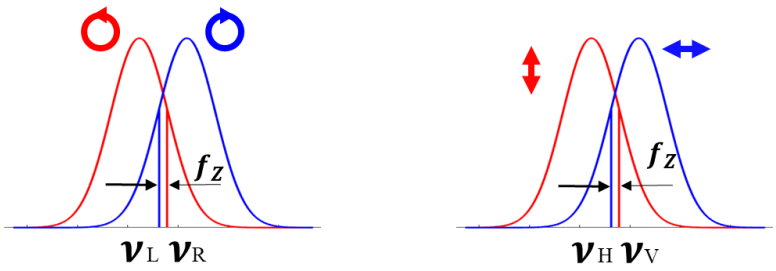

Figure 3 - On the left, the representation of the spectrum of a laser medium experiencing the Longitudinal Zeeman effect, whereas on the right, those of a Transverse Zeeman effect. The red/blue lines and arrows represent the gain curves split by the Zeeman effect and the associated polarization states respectively (L/R: circular left/right, H/V, linear horizontal/vertical) .

In the other case, the presence of a cavity birefringence allows the simultaneous oscillation of the two orthogonal cavity modes. Here, the anisotropy effect is introduced by using some birefringent cavity that provides closely spaced resonances associated with orthogonal polarizations. In an ideal isotropic cavity, there are no polarization-dependent losses or gains due to the absence of any polarizing and retarding optical elements. The roundtrip lengths for the cross-polarized light components traveling in the cavity axis are equal. If the laser cavity contains any anisotropy, each resonance frequency of the resonator splits into two closely spaced transmittance peaks [48]. Two cross-polarized components experience different path lengths because of the different refractive indices of the birefringent elements. Beneath they are oscillating in the same optical cavity, the two beams experience a different FSR. Therefore, their optical spectra are slightly different because of the different optical pathlength they experience during each roundtrip. Birefringence can be related both to the intrinsic optical property of an intracavity optical element [49] and being induced through photo-elastic [50] or electro-optic [51] effect. There is actually also a third method that simply exploits a combination of the first two approaches [48]. These methods have been used with several implementations in gas, semiconductor and solid-state lasers. All these devices emit a dual-frequency, dual-polarization (DFDP) radiation made by two overlapped beams with orthogonal polarization and a tiny frequency difference. Annex A shows how to model with the Jones and Stokes formalism the overall polarization state of this kind of optical output. This description leads to a beam with a carrier frequency in the optical range (VIS/NIR) whose polarization state evolves at a much lower rate, related to the frequency difference between its components. The value of difference depends upon the technology used to realize the DFDP emission. In ZLs, it may reach few MHz and is related to the strength of the magnetic field inside the active medium. This device has been already used to perform polarimetric measurement on the scattered components of light [52], [53]. This works act as a trigger for the projects developed in this thesis. The other methods to generate the DFDP radiation allow to reach few GHz and such frequency separation depends upon the overall cavity birefringence and on the other geometrical parameters of the resonator. In both cases, the rate of the polarization evolution of a DFDP beam is in the radio frequency (RF) range. Such generation rate makes these devices an ideal source for polarization-based

laser scanning microscopy. In these applications, the pixel-dwell time of the scanning acquisition imposes a fast switching of the polarization states. Moreover, no external devices are needed to control the polarization state, enabling the realization of a more compact setup.

2.3.2 - Dual-Comb Lasers (DCLs)

A Dual-Comb Laser (DCL) is a mode-locked laser emitting two-twin trains of ultrashort pulses that are associated with two mutually coherent Optical Frequency Combs (OFCs) in the spectrum. The emission of a mode-locked laser can be described by means of a Dirac comb both in the time and frequency domain: this kind of emission is called Optical Frequency Comb and its electric field, in time and frequency respectively, can be expressed as follows.

$$E(t) = \left(A(t) \cdot e^{i\omega_0 t}\right) * \left[\sum_n \delta(t - nT_R) \cdot e^{i\omega_{CEO} t}\right] + c.c.$$

$$\tilde{E}(\omega) = \left(\tilde{A}(\omega - \omega_0)\right) \cdot \left[\sum_n \delta(\omega - n\omega_R - \omega_{CEO})\right] + c.c.$$

And its intensity is: $I(t) = I_P(t) * \sum_n \delta\left(t - nT_{R,k}\right)$, where $I_P(t) = |A(t)|^2$ is the time-dependent intensity of a single pulse. $A(t)$ represents the envelope pulse shape and in most cases, it can be assumed as a gaussian or hyperbolic secant pulse. The intensity $I(t)$ describes a pulse train where the time interval between two consecutive pulses is $T_R = 2\pi/\omega_R$. Here, the FSR determines the pulse repetition rate ($FSR = f_{rep} = {T_R}^{-1}$). This time describes the temporal distance between two consecutive pulses (in time). The term $e^{i\omega_0 t}$ is the oscillation of the electric field of the carrier beneath the pulse envelope with optical frequency ω_0. Then, the convolution with the Dirac comb, periodically spaced by the roundtrip time, describes the repetition of the pulse in a train fashion. The phase term related to the ω_{CEO} describes the frequency shift where the comb pattern begins in the optical spectrum.

A DCL can be described as two beams with slightly different repetition rate $\omega_R = 2\pi f_R$. The interaction between two OFCs leads to the generation of a strong interferometric signal in virtue of the mutual coherence of the two combs. The time picture of the self-mixing of the two combs is a third train of interferograms, where the time interval between two consecutive interferograms is linked to their repetition rate difference (Δf_{rep}). Analogously, the spectrum of this interferometric signal is represented as a third comb in the RF range that is a rescaled replica of the optical output spectrum of the laser.

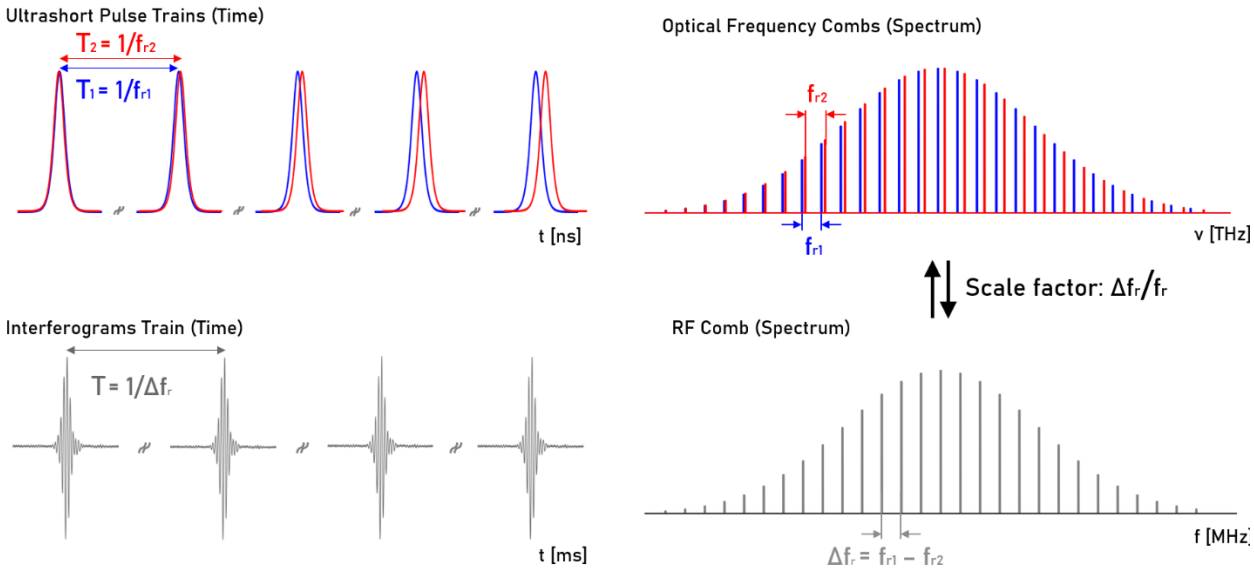

Figure 4 - Time and Frequency representation of a DCL. The upper part shows the two twin ultrashort pulse trains and the associated OFCs. The lower section instead shows the interferograms rising from the self-mixing of the two OFCs. Its spectrum contains a down-converted replica of the optical spectra in the RF range.

There are two main approaches that can be used to obtain the DCL radiation. The first involves the use of two mode-locked laser mutually synchronized through an active electronic system for locking them together. The other is to use the same resonator with some multiplexing element in its cavity that is introducing the frequency shifts in the repetition rate term and allows for the simultaneous oscillation of two beams. In this case, the two pulse trains oscillate in a single resonator, allowing to passively maintain the mutual coherence between them and to avoid the use of sophisticated phase-locking electrical systems. Dual-Combs generation can be achieved through different laser multiplexing strategies, namely based on wavelength, polarization, circulation direction or optical path [54]. The great advantage of this device is the presence of a detuning term, $\Delta f_{rep} = f_{rep,1} - f_{rep,2}$, representing the rep. rate difference exhibited by the two laser beams: it is the consequence of the different optical paths experienced in the cavity due to the multiplexing and it arises when the two OFCs interfere. This term allows to link the optical spectrum, in the hundreds of THz range, to the RF spectrum: each line pair of the two OFCs. is "down-converted" to a single beating line at the frequency difference between the two optical components. The resulting RF comb is made by many lines spaced by the amount of Δf_{rep} between the two OFCs [55], [56]. Therefore, mapping from the optical to the RF domain allows for directly measuring the alteration in the laser spectra with simple electronic instrumentation since standard photodiodes can handle the RF frequencies. The spectral width associated with the ultrashort pulses is relatively wide, so optical-to-RF mapping covers a wide range of wavelengths. These features make the DCL a popular source for researchers operating in the field of precise spectroscopy [56]. Recent works have also demonstrated this technology's potential when applied to fluorescence microscopy [57].

If the two polarizations of the two combs are crossed, the resulting polarization state has a feature similar to that of the two orthogonally polarized beams emitted by a DFDP laser. Each pair of corresponding lines from the two combs can be described as an optical signal whose

polarization is evolving at RF frequency. In addition, the spectral coverage of a DCL allows the generation of a broadband beam with a time-evolving polarization state at RF rate. This feature could be helpful for both spectroscopic and imaging applications requiring a hyperspectral analysis of the optical anisotropies of specimens.

References

[1] P. Davidovits and M. D. Egger, "Scanning laser microscope," *Nature*, vol. 223, no. 5208, p. 831, 1969, doi: 10.1038/223831a0.

[2] I. J. Cox, "Scanning optical fluorescence microscopy," *J. Microsc.*, vol. 133, no. 2, pp. 149–154, 1984, doi: 10.1111/j.1365-2818.1984.tb00480.x.

[3] M. D. Duncan, J. Reintjes, and T. J. Manuccia, "Scanning coherent anti-Stokes Raman microscope," *Opt. Lett.*, vol. 7, no. 8, p. 350, 1982, doi: 10.1364/ol.7.000350.

[4] W. Denk, J. H. Strickler, and W. W. Webb, "Two-Photon Laser Scanning Fluorescence Microscopy," *Science (80-.).*, vol. 248, no. 4951, pp. 73–76, Apr. 1990, doi: 10.1126/science.2321027.

[5] G. J. Puppels *et al.*, "Studying single living cells and chromosomes by confocal Raman microspectroscopy," *Nature*, vol. 347, no. 6290, pp. 301–303, 1990, doi: 10.1038/347301a0.

[6] S. Nakamura *et al.*, "InGaN-Based Multi-Quantum-Well-Structure Laser Diodes," *Jpn. J. Appl. Phys.*, vol. 35, no. 1B, p. L74, Jan. 1996, doi: 10.1143/JJAP.35.L74.

[7] N. Savage, "Ultraviolet lasers," *Nat. Photonics*, vol. 1, no. 2, pp. 83–85, 2007, doi: 10.1038/nphoton.2006.95.

[8] N. Savage, "Diode drivers," *Nat. Photonics*, vol. 2, no. 4, pp. 252–253, 2008, doi: 10.1038/nphoton.2008.49.

[9] Y. Cai, J. Ding, Z. Bai, Y. Qi, Y. Wang, and Z. Lu, "Recent progress in yellow laser: Principles, status and perspectives," *Opt. Laser Technol.*, vol. 152, no. December 2021, p. 108113, 2022, doi: 10.1016/j.optlastec.2022.108113.

[10] C. Kränkel, D. T. Marzahl, F. Moglia, G. Huber, and P. W. Metz, "Out of the blue: semiconductor laser pumped visible rare-earth doped lasers," *Laser Photonics Rev.*, vol. 10, no. 4, pp. 548–568, 2016, doi: 10.1002/lpor.201500290.

[11] S. Kalusniak, E. Castellano-Hernández, H. Yalçinoğlu, H. Tanaka, and C. Kränkel, "Spectroscopic properties of Tb3+ as an ion for visible lasers," *Appl. Phys. B Lasers Opt.*, vol. 128, no. 2, pp. 1–16, 2022, doi: 10.1007/s00340-022-07759-1.

[12] H. Tanaka *et al.*, "Visible solid-state lasers based on Pr3+ and Tb3+," *Prog. Quantum Electron.*, vol. 84, pp. 1–37, 2022, doi: 10.1016/j.pquantelec.2022.100411.

[13] G. Bolognesi *et al.*, "Yellow laser performance of Dy^3+ in co-doped Dy,Tb:LiLuF_4," *Opt. Lett.*, vol. 39, no. 23, p. 6628, 2014, doi: 10.1364/ol.39.006628.

[14] E. Castellano-Hernández, S. Kalusniak, P. W. Metz, and C. Kränkel, "Diode-Pumped Laser Operation of Tb3+:LiLuF4 in the Green and Yellow Spectral Range," *Laser Photonics Rev.*, vol. 14, no. 2, pp. 1–7, 2020, doi: 10.1002/lpor.201900229.

[15] H. U. X. Iao, X. U. J. Iang, and M. I. J. D. Amzen, "Alexandrite lasers with blue-diode-pumping," vol. 31, no. 4, pp. 5832–5842, 2023.

[16] A. Richter, E. Heumann, G. Huber, V. Ostroumov, and W. Seelert, "Power scaling of semiconductor laser pumped Praseodymium-lasers," *Opt. Express*, vol. 15, no. 8, p. 5172, 2007, doi: 10.1364/oe.15.005172.

[17] H. Liu *et al.*, "Review of laser-diode pumped Ti:sapphire laser," *Microw. Opt. Technol. Lett.*,

vol. 63, no. 8, pp. 2135–2144, 2021, doi: 10.1002/mop.32882.
[18] C. Lefort, "A review of biomedical multiphoton microscopy and its laser sources," *J. Phys. D. Appl. Phys.*, vol. 50, no. 42, 2017, doi: 10.1088/1361-6463/aa8050.
[19] P. W. Roth, A. J. Maclean, D. Burns, and A. J. Kemp, "Directly diode-laser-pumped Ti : sapphire laser," vol. 34, no. 21, pp. 3334–3336, 2009.
[20] P. I. P. Ichon, A. D. B. Arbet, J. E. A. N. H. B. Lanchot, F. R. D. Ruon, F. R. B. Alembois, and P. A. G. Eorges, "Light-emitting diodes : a new paradigm for Ti : sapphire pumping," vol. 5, no. 10, 2018.
[21] S. Brustlein *et al.*, "Optical parametric oscillator-based light source for coherent Raman scattering microscopy: practical overview," *J. Biomed. Opt.*, vol. 16, no. 02, p. 1, 2011, doi: 10.1117/1.3533311.
[22] K. Guesmi *et al.*, "Dual-color deep-tissue three-photon microscopy with a multiband infrared laser," *Light Sci. Appl.*, vol. 7, no. 1, 2018, doi: 10.1038/s41377-018-0012-2.
[23] J. F. Ortas *et al.*, "Label-free imaging of red blood cells and oxygenation with color third-order sum-frequency generation microscopy," *Light Sci. Appl.*, vol. 12, no. 1, 2023, doi: 10.1038/s41377-022-01064-4.
[24] A. Arie and N. Voloch, "Periodic, quasi-periodic, and random quadratic nonlinear photonic crystals," *Laser Photonics Rev.*, vol. 4, no. 3, pp. 355–373, 2010, doi: 10.1002/lpor.200910006.
[25] N. Savage, "Nonlinear crystals," *Nat. Photonics*, vol. 2, no. 6, pp. 380–381, 2008, doi: 10.1038/nphoton.2008.97.
[26] M. Marangoni, A. Gambetta, C. Manzoni, V. Kumar, R. Ramponi, and G. Cerullo, "Fiber-format CARS spectroscopy by spectral compression of femtosecond pulses from a single laser oscillator," *Opt. Lett.*, vol. 34, no. 21, p. 3262, 2009, doi: 10.1364/ol.34.003262.
[27] N. Savage, "Optical parametric oscillators," *Nat. Photonics*, vol. 4, no. 2, pp. 124–125, Feb. 2010, doi: 10.1038/nphoton.2009.283.
[28] T. Steinle *et al.*, "Synchronization-free all-solid-state laser system for stimulated Raman scattering microscopy," *Nat. Publ. Gr.*, no. December 2015, pp. 1–6, 2016, doi: 10.1038/lsa.2016.149.
[29] F. Crisa, V. Kumar, A. Perri, M. Marangoni, G. Cerullo, and D. Polli, "Spectrochimica Acta Part A : Molecular and Biomolecular Spectroscopy Multimodal nonlinear microscope based on a compact fi ber-format laser source," vol. 188, pp. 135–140, 2018, doi: 10.1016/j.saa.2017.06.055.
[30] J. Nilsson, "High power fiber lasers," *Opt. InfoBase Conf. Pap.*, vol. 20, no. 5, 2010, doi: 10.1364/cleo.2010.ctuc1.
[31] C. Xu and F. W. Wise, "Recent advances in fibre lasers for nonlinear microscopy," *Nat. Photonics*, vol. 7, no. 11, pp. 875–882, 2013, doi: 10.1038/nphoton.2013.284.
[32] N. G. Horton *et al.*, "In vivo three-photon microscopy of subcortical structures within an intact mouse brain," *Nat. Photonics*, vol. 7, no. 3, pp. 205–209, 2013, doi: 10.1038/nphoton.2012.336.
[33] C. F. Kaminski, R. S. Watt, A. D. Elder, J. H. Frank, and J. Hult, "Supercontinuum radiation for applications in chemical sensing and microscopy," *Appl. Phys. B Lasers Opt.*, vol. 92, no. 3 SPECIAL ISSUE, pp. 367–378, 2008, doi: 10.1007/s00340-008-3132-1.
[34] C. Poudel and C. F. Kaminski, "Supercontinuum radiation in fluorescence microscopy and biomedical imaging applications," *J. Opt. Soc. Am. B*, vol. 36, no. 2, p. A139, 2019, doi: 10.1364/josab.36.00a139.
[35] A. Labruyère, A. Tonello, V. Couderc, G. Huss, and P. Leproux, "Compact supercontinuum sources and their biomedical applications," *Opt. Fiber Technol.*, vol. 18, no. 5, pp. 375–378, 2012, doi: 10.1016/j.yofte.2012.08.003.
[36] F. Vernuccio *et al.*, "Fingerprint multiplex CARS at high speed based on supercontinuum

generation in bulk media and deep learning spectral denoising," *Opt. Express*, vol. 30, no. 17, p. 30135, 2022, doi: 10.1364/oe.463032.

[37] D. Wildanger, E. Rittweger, L. Kastrup, and S. W. Hell, "STED microscopy with a supercontinuum laser source," *Opt. Express*, vol. 16, no. 13, p. 9614, 2008, doi: 10.1364/oe.16.009614.

[38] E. Auksorius *et al.*, "Stimulated emission depletion microscopy with a supercontinuum source and fluorescence lifetime imaging," *Opt. Lett.*, vol. 33, no. 2, p. 113, 2008, doi: 10.1364/ol.33.000113.

[39] T. Chartier *et al.*, "Channeled spectrum of a fiber laser," vol. 18, no. 5, pp. 355–357, 1993.

[40] T. Shigeoka, S. Imanishi, and S. Kawata, "Development of a beat frequency tunable stabilized axial Zeeman laser," *Japanese J. Appl. Physics, Part 1 Regul. Pap. Short Notes Rev. Pap.*, vol. 36, no. 5 A, pp. 2681–2684, 1997, doi: 10.1143/jjap.36.2681.

[41] D. Naidoo *et al.*, "Controlled generation of higher-order Poincaré sphere beams from a laser," *Nat. Photonics*, vol. 10, no. 5, pp. 327–332, 2016, doi: 10.1038/nphoton.2016.37.

[42] J. Junghans, M. Keller, and H. Weber, "Laser resonators with polarizing elements—eigenstates and eigenvalues of polarization: addendum," *Appl. Opt.*, vol. 14, no. 8, p. 1758, 1975, doi: 10.1364/ao.14.001758.

[43] F. Bretenaker and A. Le Floch, "Laser eigenstates in the framework of a spatially generalized Jones matrix formalism," *J. Opt. Soc. Am. B*, vol. 8, no. 2, p. 230, 1991, doi: 10.1364/josab.8.000230.

[44] W. Culshaw and J. Kannelaud, "Zeeman and coherence effects in the He-Ne laser," *Phys. Rev.*, vol. 133, no. 3A, 1964, doi: 10.1103/PhysRev.133.A691.

[45] H. Statz, R. Paananen, and G. F. Koster, "Zeeman Effect in Gaseous Helium-Neon Optical Maser," *J. Appl. Phys.*, vol. 33, no. 7, pp. 2319–2321, 1962, doi: 10.1063/1.1728954.

[46] H. Takasaki, N. Umeda, and M. Tsukiji, "Stabilized transverse Zeeman laser as a new light source for optical measurement," *Appl. Opt.*, vol. 19, no. 3, p. 435, 1980, doi: 10.1364/ao.19.000435.

[47] T. Baer, F. V. Kowalski, and J. L. Hall, "Frequency stabilization of a 0633-μm He–Ne longitudinal Zeeman laser," *Appl. Opt.*, vol. 19, no. 18, p. 3173, 1980, doi: 10.1364/ao.19.003173.

[48] S. Zhang, Y. Tan, and Y. Li, "Orthogonally polarized dual frequency lasers and applications in self-sensing metrology," *Meas. Sci. Technol.*, vol. 21, no. 5, 2010, doi: 10.1088/0957-0233/21/5/054016.

[49] M. Brunel, O. Emile, F. Bretenaker, A. LeFloch, B. Ferrand, and E. Molva, "Tunable two-frequency lasers for lifetime measurements," *Opt. Rev.*, vol. 4, no. 5, pp. 550–552, 1997, doi: 10.1007/s10043-997-0550-y.

[50] W. Holzapfel and W. Settgast, "Precise force measurement over 6 decades applying the resonator-internal photoelastic effect," *Appl. Phys. B Photophysics Laser Chem.*, vol. 49, no. 2, pp. 169–172, Aug. 1989, doi: 10.1007/BF00332278.

[51] S. Zhang, M. Lu, G. Jin, and M. Wu, "Laser frequency split by an electro-optical element in its cavity," *Opt. Commun.*, vol. 96, no. 4–6, pp. 245–248, 1993, doi: 10.1016/0030-4018(93)90269-B.

[52] R. G. Johnston, S. B. Singham, and G. C. Salzman, "Phase differential scattering from microspheres," *Appl. Opt.*, vol. 25, no. 19, p. 3566, Oct. 1986, doi: 10.1364/AO.25.003566.

[53] Roger G. Johnston, "US4764013A -Interferometric apparatus and method for detection and characterization of particles using light scattered therefrom," 1988.

[54] R. Liao, H. Tian, W. Liu, R. Li, Y. Song, and M. Hu, "Dual-comb generation from a single laser source: principles and spectroscopic applications towards mid-IR—A review," *J. Phys. Photonics*, vol. 2, no. 4, p. 042006, Sep. 2020, doi: 10.1088/2515-7647/aba66e.

[55] S. Schiller, "Spectrometry with frequency combs," *Opt. Lett.*, vol. 27, no. 9, p. 766, 2002, doi:

10.1364/ol.27.000766.
[56] I. Coddington, N. Newbury, and W. Swann, "Dual-comb spectroscopy," *Optica*, vol. 3, no. 4, p. 414, Apr. 2016, doi: 10.1364/OPTICA.3.000414.
[57] T. Mizuno *et al.*, "Full-field fluorescence lifetime dual-comb microscopy using spectral mapping and frequency multiplexing of dual-comb optical beats," *Sci. Adv.*, vol. 7, no. 1, pp. 1–12, Jan. 2021, doi: 10.1126/sciadv.abd2102.

3 - Zeeman Laser

This section shows the development and performance obtained with a Zeeman Laser (ZL) based on the Longitudinal effect. As anticipated, a Zeeman Laser can generate a dual-polarization output when an external magnetic field is applied to it. We employed such technology to obtain the DFDP laser output made by two orthogonally polarized beams with a tiny and fixed frequency difference. Such emission is needed to achieve the fast generation of polarization states. However, in order to reach such emission in a stable way, an active stabilization of the cavity length is needed. The Zeeman laser system I developed is based on a handmade kit made by Samuel M. Goldwasser [1]. This kit is intended for the assembly and use of a Zeeman laser both for research and for hobbyist purposes. His website is a truly all-encompassing source of information and a guide to assembling such a device. This Chapter shows the development and performances of the laser device, how we applied the magnetic field needed to trigger the Zeeman effect and how the cavity length has been stabilized. Finally, the DFDP radiation has been used to reproduce a polarimetric method to measure the polarimetric response of semitransparent samples.

3.1 - Development and performances

The devices I realized were based on a laser kit intended to be used to assemble longitudinal or axial Zeeman effect laser. Table 2 shows the opto-electronical components contained in such kit.

HV power supply	Silicon (Si) photodiodes	HeNe laser tube	Linear polarizer (LP)
adhesive foil heater	Electronic prototyping board	Polarizing beam splitter (PBS)	Quarter wave plates (QWPs)
Arduino microprocessor board	Several resistors, capacitors, heater driver transistor, LEDs	Rare earth magnets	

Table 2 - List of components of the Zeeman laser kit

I started with a simple Helium-Neon (HeNe) laser. Its resonator is made by a 15-cm long tube containing a thin capillary with the gas mixture active as active medium and the cavity ending mirrors. A high voltage (HV) Power Supply drives the pumping mechanism based on the plasma gas discharge. A custom holder, shown in Figure 5, provides mechanical stability. It will later be used to place also the rare-earth rods generating the magnetic field.

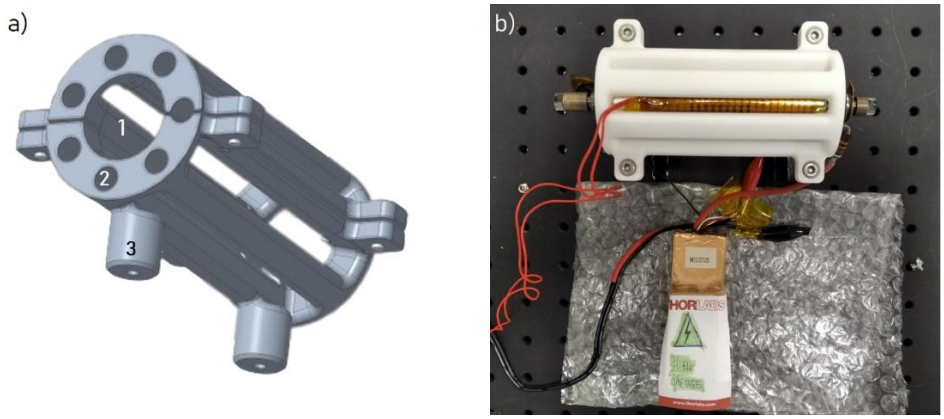

Figure 5 – a): Sketch of the custom laser holder with the big central hole to seat the HeNe tube (1), the side holes hosting the magnetic rods (2) and the screw hole to fix the holder to the optical table. b): a picture of the actual laser inside the custom holder

I firstly characterized the electrical properties of the HV power supply by using a multimeter and a HV probe (Agilent N2771A). The power supply is made by 2 main elements, the wall power adapter, that transform the 220V voltage into a 5 V - 2 A output and the HV transformer, which give a high voltage-low current output to the laser tube. The HV voltage output given by the HV Transformer is around 8 kV when it works as open circuit, whereas it drops to the stationary value of 1 kV when it is connected to the He-Ne Tube. The HV Probe was linked to a digital oscilloscope (Tektronix TDS1001B) to monitor the voltage levels.

Then, I characterized the steady-state operation of the laser working without any magnets or active stabilization system. During its operation, the HeNe laser emits two light outputs at 632.8 nm and I characterized them by means of a powermeter (Thorlabs, S121C). The main one on the front side, associated with the cavity Output Coupler (OC) and a secondary one on the rear side that is a low power leakage due to the imperfect high reflectivity (ideally 100%) of the other cavity ending mirror. Table 3 reports the results of these characterizations.

Output Type	Average Power	Standard Deviation
Front	1.175 mW	0.016 mW
Rear	45.318 µW	0.881 µW

Table 3 – Results of the power monitoring of the two outputs of the HeNe laser

The laser was working in contact with the environmental air, as one can observe in Fig.5-b. I also characterized both the temperature of the lab and on the laser with a simple thermocouple (Keysight U1186A) fixed on the laser tube. While the room temperature was around 22°C, the laser tube surface reached 40 °C after 30 min of operation.

The cavity length (15 cm) and the gain bandwidth of the HeNe allow single-longitudinal-mode oscillation. The laser cavity selects and amplifies only one resonating mode from the combined action of the resonator and active medium gain. Therefore, the output spectrum is made by a single laser line. However, in this configuration, the polarization of the output beam continuously switches from a certain state to the other, even if the overall output power is constant. This is

due to a phenomenon known as mode-sweeping and it is caused by the micro thermal expansion of the cavity length, which is deepened in Annex B. Fig.6 shows the switching of the power between the two modes during such a process.

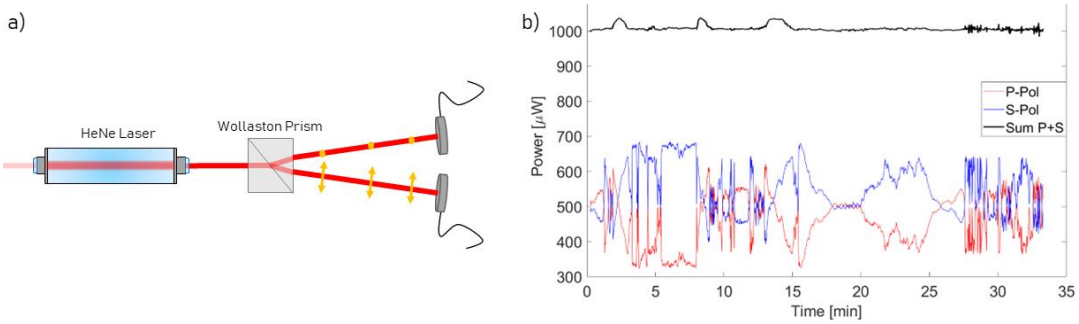

Figure 6 – (a) The experimental setup used for monitoring the power fluctuations with the respect of the polarization state. (b) Power switch between modes with different polarizations

Then, I put in the peripheral holes of the laser holder 7 rods made by 7 cylindrical magnets 6x10 mm. The magnets have been placed in order that each rod have the same orientation in terms of magnetic poles, creating the magnetic flux parallel to the cavity axis, as shown in the scheme in fig.7.

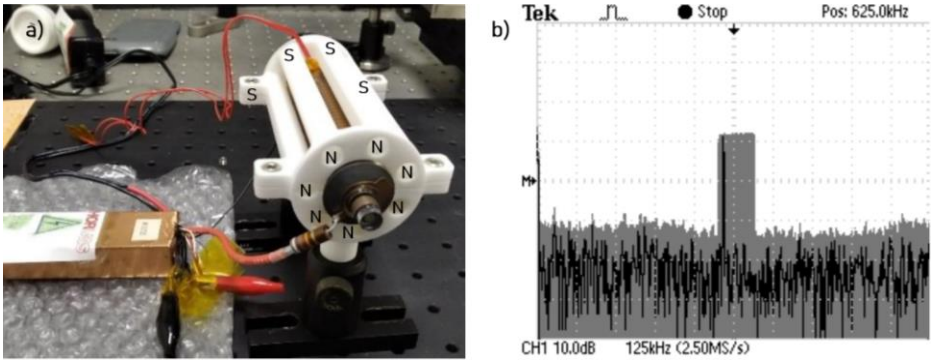

Figure 7 - a) Custom holder of the He-Ne tube with the seats for the magnetic bars (N-S denotes the orientation of the magnetic poles of the magnets) - b) frequency sweeping of the beating signal generated by the interference of the two Zeeman components.

Thus, the magnetic field is parallel to the cavity axis and the cavity mode degeneracy leads to the oscillation of two Orthogonal Circularly Polarized (OCP) light components with a slight frequency shift. The electric field associated with the dual-frequency, dual-polarization emission of the two beams, with ω_R, ω_L and k_R, k_L as optical frequencies and wave vector respectively, is described by Eq. 1.

Eq. 2) $$\overrightarrow{E_i} = \overrightarrow{E_R} + \overrightarrow{E_L} = A_R \cdot \overrightarrow{V_R} \cdot e^{-i(\omega_R t - k_R z)} + A_L \cdot \overrightarrow{V_L} \cdot e^{-i(\omega_L t - k_L z)}$$

where $\overrightarrow{V_R}$ and $\overrightarrow{V_L}$ are the Jones vectors of the two circularly polarized waves $(\overrightarrow{E_R}, \overrightarrow{E_L})$ with amplitudes A_R, A_L. The frequency shift between the two orthogonally polarized components can be detected by sending the DFDP beam onto a photodetector covered by a linear polarizer. The

projection of the two circularly polarized laser lines forces the two orthogonal components to vibrate on the same plane and thus to interfere. Eq. 2-3 shows the generation of the intensity beating signal at $\omega_z = \omega_R - \omega_L$ rising from the interference between the two components of the DFDP emission.

Eq. 3) $\overrightarrow{E_F} = [J_H] \cdot (\overrightarrow{E_R} + \overrightarrow{E_L})$

Eq. 4) $I_o(t) \propto \left|\overrightarrow{E_o}\right|^2 = I_{DC} + I_{AC}\, cos\,(\omega_z t - \varphi)$

where $[J_H]$ is the Jones matrix of a linear polarizer at 0°. The photodiode placed after the polarizer detects a signal ($I_o(t)$) with a constant component (I_{DC}) and a sinusoidal oscillation. The frequency of such oscillating beating signal with amplitude I_{AC} is determined by the frequency difference between the two optical components.

Without any active stabilization of the cavity length, such oscillating frequency is sweeping in the range around 550 kHz and 700 kHz, as one can see in Fig.7. Its sweeping is due to the instability introduced by the thermo-mechanical expansion of the cavity length because of the heat dissipation that occurs during the pumping process of the laser. Our custom Zeeman Laser requires an external stabilization electronics with feedback action on the light source. Such Stabilization Unit (SU), shown in Fig. 8, is made up of Polarizing and Unpolarizing Beam Splitters (PBS/UBS), a QWP, a LP and three photodiodes. The OCP light is transformed into Orthogonal Linearly Polarized (OLP) light by means of the QWP, whose fast axis has been oriented in order to match the direction of the linearly polarized components with the axes of the PBS. So, the PBS multiplex the two modes with different optical frequencies by exploiting their orthogonal polarization states. The two photodiodes after the PBS are used to monitor the power of the two longitudinal modes and these monitor signals are provided to the microcontroller (µC). Then, it drives the current for the foil heater according to the two monitor signals, in order to minimize their fluctuations and equalize their power.

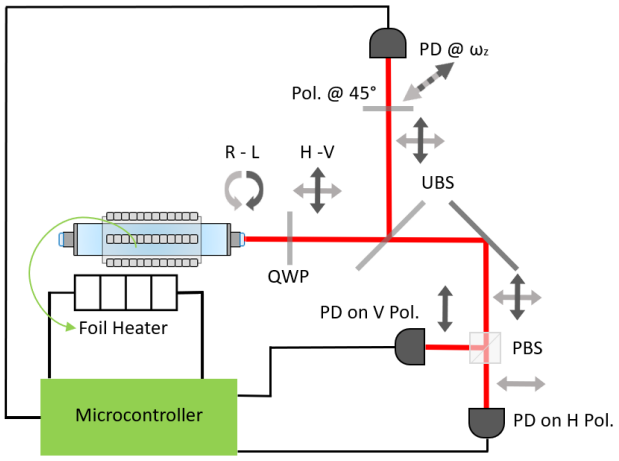

Figure 8 – Schematic of the Stabilization Unit with its main components

The fine adjustment of the cavity length is achieved by heating the laser tube through the foil heater and minimizing its temperature variations. Finally, the third photodiode is used in

combination with a linear polarizer to generate the beating signal. It monitors and minimize the variation of the beating frequency, acting so as frequency counter (FC). A microcontroller (µC) receives these feedback signals and drives a foil heather (FH) to obtain the laser stability.

The stabilization algorithm is meant to make the laser insensitive to environmental temperature variations. Initially, the laser tube alone reaches its thermal steady state because of the heat dissipation during the pumping discharge process. Therefore, the first warm up step implies to heat up the laser tube above this temperature. Then, the SU controls the cavity length by heating the tube through the foil heater wrapped around it or by cooling it down exploiting air convection. Once the Zeeman Laser has been assembled and stabilized, it is able to emit two slightly separated OCP longitudinal modes, whose distance in frequency is around 700 kHz.

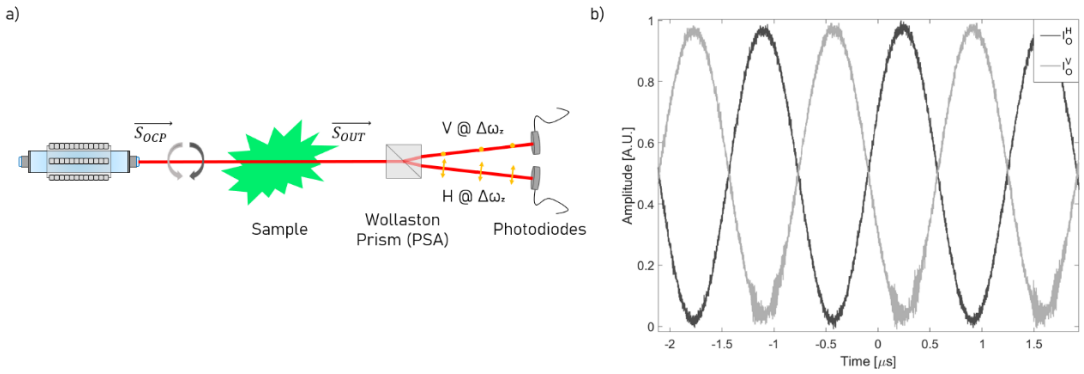

Figure 9 – a) Schematic of the setup for the single-point characterization of the polarimetric response of a sample. b) The stabilization of the frequency distance between the two optical components of the Zeeman laser emission leads to the formation of two clean anti-phase sinusoidal signals.

A Wollaston Prism (WP10, Thorlabs, US), used as Polarization State Analyzer, and a pair of photodiodes (PDA36A-EC, Thorlabs, US) are used to generate a couple of beating signals. They are formed for the same principle exploited for the frequency counter photodiode in the Stabilization Unit. This stage returns a digital signal used to monitor the oscillation frequency of the beating between the two optical components. Thus, the optical setup shown in Fig.9 is used to encode the optical anisotropies of samples in such interferometric signals. Their analysis leads to the identification of the Mueller coefficients, as explained in the next section.

3.2 – Stokes-Mueller description of the beating signal

The DFDP emission of the Zeeman laser has been already shown by eq. 1. The description of its polarization state is carried out by the Jones vectors $\overrightarrow{V_R}, \overrightarrow{V_L}$. However, the different oscillation frequencies of the two components of such electric field leads to a time-varying phase relation between the two orthogonal components. The orthogonality relation and the time-evolving phase term between the two optical components leads to a time-varying polarization state. Therefore, it would be more convenient to embed the evolving terms in the description of the polarization states. The resulting Jones vector is shown in Eq. 4, where I assumed the reference frame with respect to the R/L basis and the amplitude of the two waves to be equal (A_Z).

Eq. 5) $\overrightarrow{V_Z} = A_Z \cdot \begin{bmatrix} e^{-i(\omega_R t - k_R z)} \\ e^{-i(\omega_L t - k_L z)} \end{bmatrix}$

The elements of the Stokes vector associated to the DFDP emission can be easily obtained by using the definition based on the electric field (reported in Annex A) or through the Pauli matrices and the following procedure.

Eq. 6) $[\sigma_1] = \begin{bmatrix} 1 & 0 \\ 0 & 1 \end{bmatrix}$ $[\sigma_2] = \begin{bmatrix} 1 & 0 \\ 0 & 1 \end{bmatrix}$ $[\sigma_3] = \begin{bmatrix} 1 & 0 \\ 0 & 1 \end{bmatrix}$ $[\sigma_4] = \begin{bmatrix} 1 & 0 \\ 0 & 1 \end{bmatrix}$

Eq. 7) $S_j = \langle \sigma_j | \overrightarrow{V_Z} | \sigma_j \rangle$

The final result for OCP light highlights the effect of the frequency shift between the two orthogonal components in the overall polarization state. The final polarization state is a time-evolving linearly polarized state that is rotating at the frequency difference between the two optical components.

Eq. 8) $\overrightarrow{S_{OCP}} = \begin{bmatrix} S_1 \\ S_2 \\ S_3 \\ S_4 \end{bmatrix} = \begin{bmatrix} 1 \\ cos(\omega_Z t) \\ sin(\omega_Z t) \\ 0 \end{bmatrix}$

Such rotation rate depends upon the magnitude of the frequency difference and in the case of the Zeeman laser I developed is around 700 kHz. Such value allows to monitor the evolution of polarization state in time with simple optoelectronics devices such as photodiodes and coaxial cables but it is still significantly faster than the polarization modulation obtained with most of the active devices presented in the Ch.2.2.

For sake of completeness, the similar description of the time-evolving polarization state can be applied also to OLP light. To do so, one can substitute the Jones vectors $\overrightarrow{V_R}, \overrightarrow{V_L}$ associated with circularly polarized waves to $\overrightarrow{V_H}, \overrightarrow{V_V}$ or $\overrightarrow{V_D}, \overrightarrow{V_A}$ associated with linear polarizations, respectively horizontal-vertical or diagonal-antidiagonal. Then, the resulting Stokes vector can be calculated by using again eq.6 and the final expressions are reported by eq.8,9.

Eq. 9) $\overrightarrow{S_{OLP}^{H-V}} = \begin{bmatrix} S_1 \\ S_2 \\ S_3 \\ S_4 \end{bmatrix} = \begin{bmatrix} 1 \\ 0 \\ cos(\omega_Z t) \\ sin(\omega_Z t) \end{bmatrix}$

Eq. 10) $\overrightarrow{S_{OLP}^{D-A}} = \begin{bmatrix} S_1 \\ S_2 \\ S_3 \\ S_4 \end{bmatrix} = \begin{bmatrix} 1 \\ cos(\omega_Z t) \\ 0 \\ sin(\omega_Z t) \end{bmatrix}$

3.3 - Fast polarization encoding in the beating signal of a Zeeman laser

The DFDP emission of the Zeeman Laser defined in Eq.7 has been used to characterize the Mueller coefficients of anisotropic samples. In this thesis work, the Mueller matrix of the sample ($[M_S]$) has been modelled without any specific assumption so it has been considered has much general as possible (Eq. 10).

Eq. 11) $$[M_S] = \begin{bmatrix} m_{00} & m_{01} & m_{02} & m_{03} \\ m_{10} & m_{11} & m_{12} & m_{13} \\ m_{20} & m_{21} & m_{22} & m_{23} \\ m_{30} & m_{31} & m_{32} & m_{33} \end{bmatrix}$$

The scheme in Fig. 9 represents the optical setup I used to characterize the polarimetric response of the samples through the characterization of their Mueller coefficients. The polarization states in the two output channels (H-V) of the Polarization State Analyzer stage can be described by the Stokes vector expressed in Eq.11. Such expression takes into account the effect on the light polarization of all the polarizing elements in the optical setup. Finally, the photocurrent detected by two photodiodes is expressed by Eq.12 and it is proportional to the first element of $\overrightarrow{S_{OUT}^{H-V}}(t)$.

Eq. 12) $$\overrightarrow{S_{OUT}^{k}}(t) = \left[M_{PSA}^{k}\right] \cdot [M_S] \cdot \overrightarrow{S_{OCP}}$$

Eq. 13) $$I_{OUT}^{k}(t) = m_{00} \pm m_{10} + (m_{01} \pm m_{11})\, cos(\omega_z t) + (m_{01} \pm m_{11}) sin\,(\omega_z t)$$

Where the value of k depends upon the signal associated with one of the two photodiodes aligned on the respective output channel of the PSA. These channels correspond to the measurement of intensity of the amount of H or V polarized light respectively. In this compact notation, the sign of in the linear combinations of Mueller coefficients is plus (+) when $k = H$, whereas it is minus (-) when $k = V$. In this compact notation, the light polarization in the two output channels of the PSA (H-V) is described by changing the Mueller matrix of the PSA. Being the PSA a Wollaston prism, such matrix is defined as those of an ideal linear polarizer whose transmission axis is oriented along H and V respectively and their definition can be found in the Annex A. With a single Wollaston Prism (WP) and two photodiodes, only the first element of the Stokes vector coming from the sample alteration is measured. The analysis of the harmonic content of the signals described by Eq.11 provides the identification of the six Mueller coefficients influencing the amplitude of the constant (DC) and oscillating (AC) components of the photocurrents. The signals in Fig-9-10 shows the signals detected to perform the polarization measurement. The reference signal in the upper plot is extracted by the frequency counter photodiode in the SU. It is used as a reference for the phase shifts of the signals in the measurement arm (H-V). Since the light impinging on it is not passing through any sample, this signal represents an unperturbed condition. Then, the signals from the H-V photodiodes are represented in the lower panel. Their oscillation is in antiphase as it can be seen in Eq.11 and further phase shifts from the reference signal will be associated with the presence of some anisotropy as a fingerprint of the sample.

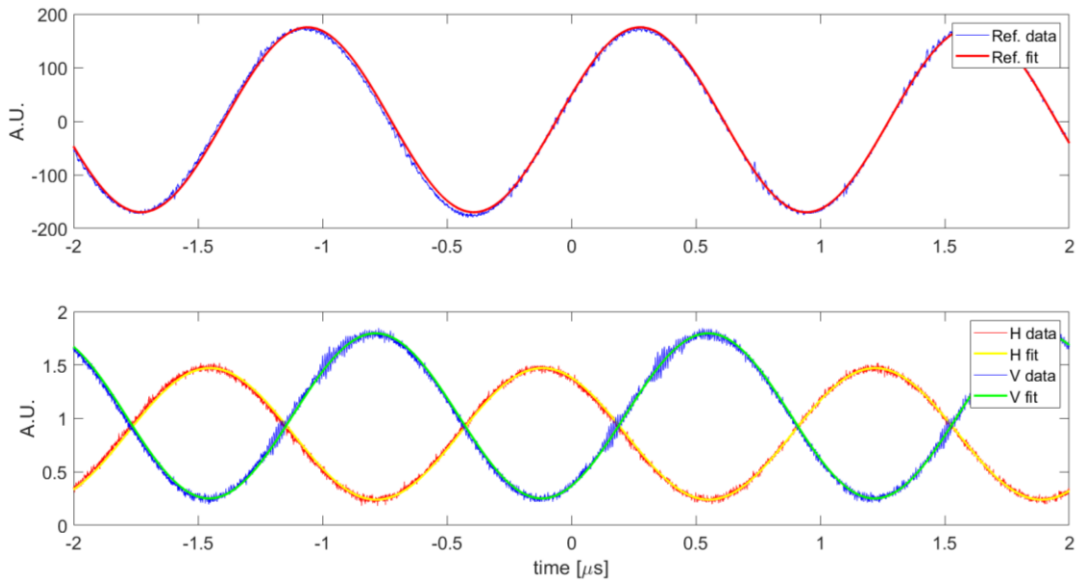

Figure 10 - Example of the three signals detected to perform the measurement of the Mueller coefficients. The presence of the sample introduces the amplitude modulation of the oscillating parts and the shift between the detected signal and the unperturbed reference signal coming from the Stabilization Unit

As a calibration step, the response of the two photodiodes has to be balanced since they have slightly differences in the background noise and responsivity. Therefore, for each sample analyzed, I acquired three images for each photodiode. One with the light coming from the laser blocked ("dark" signal), one without any sample ("air" signal) and the last of the specimen itself "sample" signal). The dark signal has been used to subtract the contribution of the dark current noise to the other images. Once this offset has been removed, I had to find a calibration coefficient that allows to equalize and compare the amplitude response from both the photodiodes.

The simplest approach to determine the Mueller coefficients encoded in the photocurrents is to fit the detected signals with an equation like Eq.11. The phase of the reference signal is identified and used to identify the phase shift between it and the two photodiodes on the measurement side. Therefore, where no sample is present (air signal) the phase calibration leads to the following conditions: $\phi_{ref-H} = 0°\ and\ \phi_{ref-V} = 180°$. Then, the amplitude of the DC and AC parts are identified by fitting the pair of photocurrents recorded for each experimental configuration. The amplitude of the cosine component is named as X, whereas Y is the other in-quadrature component. The subscripts H and V refer to the two photocurrents detected by the photodiode aligned on the two output channels of the PSA. Then, such amplitudes are summed and subtracted to find the values of the individual Mueller coefficients.

Eq. 14) $m_{00} = \frac{DC_H + DC_V}{2}$

Eq. 15) $m_{10} = \frac{DC_H + DC_V}{2}$

Eq. 16) $m_{01} = \frac{X_H + X_V}{2}$

Eq. 17) $m_{11} = \frac{X_H - X_V}{2}$

Eq. 18) $m_{02} = \frac{Y_H + Y_V}{2}$

Eq. 19) $m_{12} = \frac{Y_H - Y_V}{2}$

However, the fit procedure may be relatively slow and not so efficient for fast imaging applications. Alternatively, an easier but more effective method relying on the demodulation realized by means of a commercial lock-in amplifier (LA, HF2LI, Zurich Instruments, CH) allows to identify the six Mueller coefficients of Eq.11 in a more efficient way. Such method is shown in Ch.5 that is dealing with the actual development of the imaging system using the Zeeman laser as illumination stage. The identification of the other elements can be obtained by applying a lock-in detection scheme [2] to analyze the amplitude of the oscillating components of the detected signals. The lock-in demodulation is used to separate the amplitude of the cosine and sine components associated with the in phase and in quadrature parts. To do so, a reference signal at the same oscillating frequency has to be provided. Therefore, the signal coming from the Stabilization Unit is used to employ the heterodyne detection scheme in the lock-in detector.
Six coefficients ($m_{00}, m_{01}, m_{02}, m_{10}, m_{11}, m_{12}$) of the Mueller matrix of the sample in Eq. 11 are then identified in this specific setup architecture. By modifying the optical axis of the components, particularly the ones from the PSA other combinations of six MM coefficients are possible as shown Fig. 11. The encoding of the polarization states in the beating signal of the DFDP emission enables a high polarization generation rate. Such rate is defined by the frequency shift between the two orthogonally polarized modes and in the Zeeman laser realized such value is around 700 kHz. Therefore, by implementing a detection scheme such as that in Fig.9, the values of six Mueller elements can be determined by analyzing the signal expressed in Eq. 12 that is oscillating at 700 kHz.
Moreover, the same analysis can be performed by using the OLP illumination described in Eq.8 and 9. The results leads to the identification of a different subset of Mueller coefficients even if some of them are redundant with those identified in the OCP case.

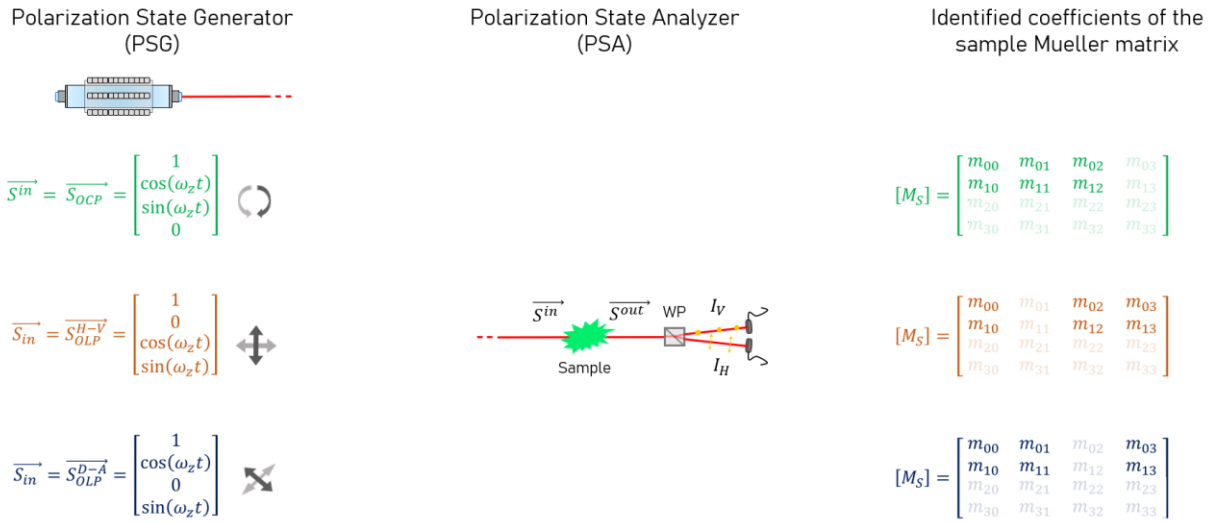

Figure 11 - Results of the identified Mueller coefficients with a partial PSA and with different illumination and PSG. The elements displayed with the fading cannot be identified with such experimental scheme.

I characterize different polarization optics, such as linear polarizer and birefringent waveplate, as reference sample with a clear polarization response (dichroism or birefringence). The Mueller coefficients have been measured with the aforementioned protocol and their values have been compared to those predicted by the theory for such optical elements. The measures have been acquired by recording the intensity of the photocurrent signals while the azimuthal angle of the sample has been rotated. Therefore, the theoretical model has been developed by predicting the evolution coefficients of the Mueller elements as function of the rotation of the azimuthal angle. For a generic sample with matrix $[M_S]$, the resulting prediction follows the relation expressed in Eq. 19, where $[R]$ and θ are the rotation matrix and the rotated azimuthal angle respectively. Annex A contains a complete list of the Mueller matrix of the standard polarization optics, such as those used to perform these characterizations, and the effect of the rotation on the values of their coefficients [3].

Eq. 20) $$[M_S] = [R(-2\theta)] \cdot [M_S] \cdot [R(2\theta)]$$

Fig.12 shows the results of these characterizations performed respectively with a linear polarizer (LP, VIS 700 BC4 CW02 ColorPol, CODIXX AG, DE) and a half wave plate (HWP, AHWP10M-600, Thorlabs, US) as reference samples. I performed such measures by using both the OCP and OLP illuminations.

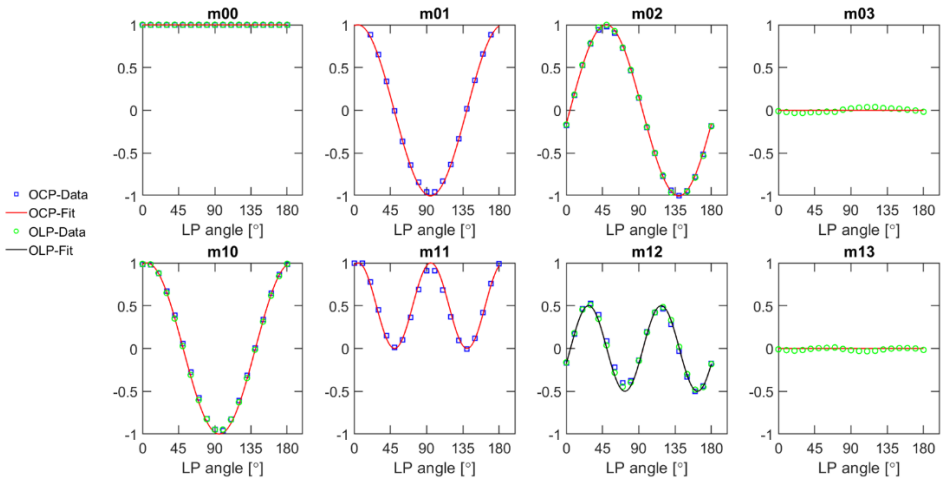

Figure 12 - Characterization of a Linear Polarizer. The eight Mueller coefficients have been identified by merging the two pairs of measurements with the OCP and OLP illumination.

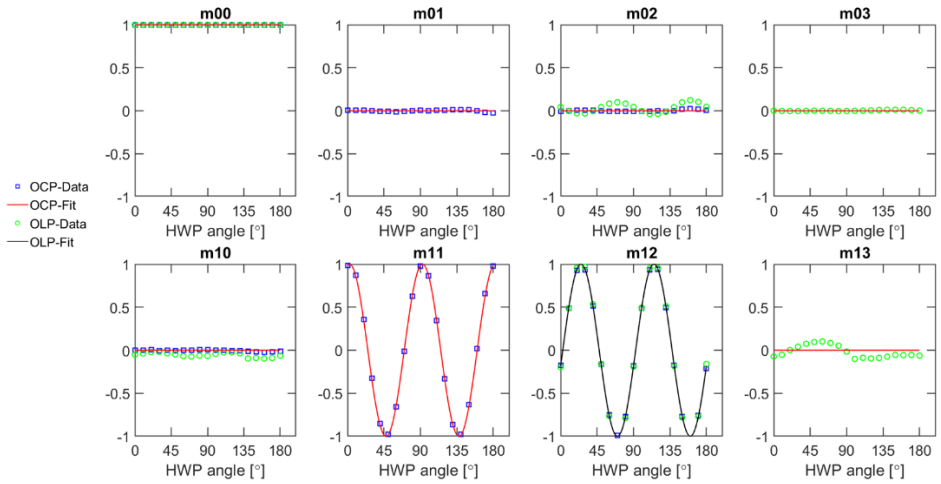

Figure 13 - Characterization of a Half Wave Plate. The eight Mueller coefficients have been identified by merging the two pairs of measurements with the OCP and OLP illumination.

The coefficients are normalized dividing their value with that of the m_{00} coefficient that is associated with the total intensity transmitted by the sample. Therefore, their value ranges from -1 to +1. These experiments have been performed by using both the OCP (in the R-L basis) and OLP (in the H-V basis) illumination modes. Each illumination modality requires two simultaneous measurements, carried out by the two photodetectors in the PSA, to identify a set of six Mueller coefficients. The third illumination modality (OLP in the D-A basis) has not been exploited since it provides a redundant result in terms of identification of Mueller coefficients, as it can be seen from Fig.11. Indeed, the merging of the results of the four measurements (two measurements for two illumination modalities) provides the identification of eight different Mueller coefficients. Some of the coefficients identified are redundant and their values is obtained twice, one for each illumination modality. The results of this validation measures allow to assess the capability of this technique to measure the Mueller coefficients by analyzing the beating signal generated through the DFDP laser.

To maintain the compactness of the setup and the simplicity in the data acquisition system, the actual measurements I carried out were based on the scheme shown in Fig. 9. However, for sake of completeness, I performed the calculation and developed the theoretical model of a setup similar to that described above but with a more complete PSA, as reported in the Supplementary Materials of [4]. The PSA stage can be modified in order to achieve the information on more Mueller coefficients. Fig. 14 shows the schemes of such optical setup where the PSA is made such that all the Stokes vectors elements of the light altered from the sample can be fully measured. The three stages of the PSA with six photodiodes allow to identify all the three components of the Stokes vector coming from the sample alteration.

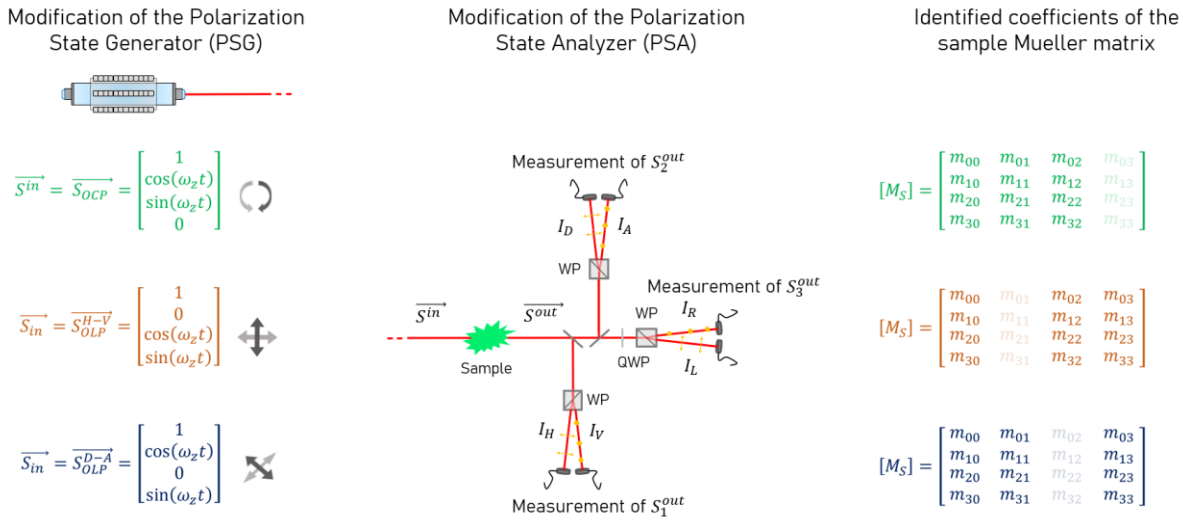

Figure 14 - Results of the identified Mueller coefficients with a complete PSA and with different illumination and PSG. The elements displayed with the fading cannot be identified with such experimental scheme.

Therefore, a subset of twelve Mueller coefficients can be identified with such experimental scheme for each illumination modality. The missing column in the reconstructed Mueller matrix is still due to the presence of a null element in the Stokes vector of the input illumination. The main difference is that the overall stages of the analyzer unlock the information on all the lines of the sample matrix, resulting in the identification of twelve elements for each setup.

3.4 - Conclusion

The method presented here enables the fast measurement of polarimetric properties of sample. The speed of the measurement is determined by the spectral distance between the two optical components of the DFDP laser. A HeNe laser can be transformed into a Zeeman laser to generate this kind of optical radiation and implement such technique. The frequency shift between its optical components is related to the magnitude of the external magnetic field applied on it. Devices able to generate a beating frequency up to few MHz have been found in literature, therefore the measurement speed can be still increased. Moreover, other DFDP source based on a different physical principle can provide the same type of optical radiation, being so useful to implement such interferometric method. This enables the possibility to access different spectral region and to achieve even higher beating frequency values. Finally, the experimental results of the method presented here deals with a PSA stage which is only measuring one element of the Stokes vector of the light altered by the sample. This configuration allows to identify six Mueller coefficients simultaneously with only two photodiodes. By adding other measurements stages, the full parameters of the output Stokes vector can be determined. The simultaneous identification of up to twelve Mueller coefficients is so enabled without using any external active device to manipulate the polarization state.

References

[1] S. M. Goldwasser, “Instructions for Stabilized Zeeman HeNe Laser Kit 1.” [Online]. Available: http://repairfaq.org/sam/eBay/zeemins3.htm.

[2] Z. Instruments, “Principles of lock-in detection and the state of the art Zurich Instruments,” no. November, pp. 1–10, 2016.

[3] H. Fujiwara, *Spectroscopic Ellipsometry*. Wiley, 2007.

[4] F. Callegari, A. Le Gratiet, A. Zunino, A. Mohebi, P. Bianchini, and A. Diaspro, “Polarization Label-Free Microscopy Imaging of Biological Samples by Exploiting the Zeeman Laser Emission,” *Front. Phys.*, vol. 9, no. October, pp. 1–8, 2021, doi: 10.3389/fphy.2021.758880.

4 – Dual-Comb Laser

This section shows the development and performance of a single-cavity solid-state Dual-Comb laser (DCL). This project has been carried out during my visit to the Ultrafast Laser Physics (ULP) group at ETH in Zurich. Here I was trained on the development and characterizations of a Dual-Comb Laser (DCL) in order to understand the potentialities and the limits of this technology and the possibility to tailor its performances to the needs of the optical microscope. As anticipated, a single-cavity DCL generates a twin pair of ultrashort pulse trains when a multiplexing mechanism is embedded in the resonator design. We employed such technology to obtain two Optical Frequency Combs (OFCs) with tiny and fixed frequency differences emitted as a pair of parallel beams. The polarization state of each OFC has been manipulated individually and they have been combined into a cross-polarized state. I used this optical emission to develop a sensing method to probe the optical anisotropies of a semitransparent medium. The self-mixing signal generated by breaking the orthogonality between the two combs gives rise to an interference signal used to encode a time-varying polarization state. Such emission is also characterized by the broad spectrum associated to the ultrashort pulses. Therefore, the DCL emission allows to perform broadband polarimetric measurements without relying on external active devices for shaping the polarization state. This Chapter shows the development and performances of the laser device, how we modify the resonator to achieve the mode-locked operation on two laser beams simultaneously. The current section deals with the development of the single-cavity DCL laser oscillator and it is divided into two main parts: the development of the resonator operating in the various regimes (CW, ML, DCL) and the characterization of its laser performances.

4.1 – Development of the DCL oscillator

The oscillator has been assembled onto a standard breadboard with optomechanical holders, adjustable mirror mounts, and is enclosed in a plastic box. We used an Yb^{3+}:$CaGdAlO_4$ crystal (commonly known as Yb:CALGO) as an active medium. Its optical, mechanical and thermal properties [1], [2] make this material a widely adopted choice for the development of high-power ultrafast lasers. Therefore, an *a*-cut Yb:CALGO crystal has been mounted in custom copper holder fixed on a translator stage, to place it in the pump focus. A wavelength-stabilized multimode laser diode (IF-HS1 , Coherent, US) emitting at 980 nm has been used as a pump source. Its output radiation was fiber-coupled through a 100 µm diameter multimode fiber with a numerical aperture of 0.15. Its input current-output optical power characterization shown a > 2 W/A electro-optical efficiency, a threshold current of 0.4 A and maximum output power > 15 W when driven with 7.5 A. After collimation in free space, the pump polarization has been controlled by means of a birefringent half-wave plate placed before a Polarization Beam Splitter (PBS). Then, the beam transmitted through the PBS has been reshaped with a 4-f system. The fiber core has been re-imaged through of a 25-mm lens (f_P) and the gain medium has been placed in the focal position. The pump polarization has been set to match the crystal *c*-axis, where the active medium exhibits the greater absorption cross-section. Both the pump diode and the gain medium have been water-cooled and Peltier cells have been used for temperature stabilization.

Then, we tested several configurations in continuous wave regime to verify the laser operations. Main variations included testing our end-pumped resonator with different output couplers and cavity lengths. The *a*-axis of the gain crystal, where the emission cross-section is greater, has been oriented in the vertical direction so the output beam is linearly vertically polarized. The pump radiation reaches the cavity through the output coupler ending mirror (OC) that is partially transmissive for the laser band (2.6 % transmission @ 1050 nm) and highly transmissive for the pump radiation. The curved mirror (M_C) and the third cavity mirror (M) folded the beam in a z-shaped path, that is closed with the ending mirror S.

In a mode locked laser, the pulse repetition rate or repetition frequency (f_R) is linked to the overall cavity length (L) to the well-known definition of the Free Spectral Range (FSR).

Eq. 21) $f_R = FSR = \frac{c}{2L}$

Where c is the speed of light. Therefore, we choose a total cavity length of 15 cm to achieve the repetition rate of 1 GHz. Such values is a good trade-off between the spectral power in each comb line and the spectral resolution, that are key quantities in the spectroscopic application of such laser source [3], [4]. The requirements of the project related to this thesis work were not demanding in term of spectral resolution. However, these features have been effectively exploited the spectroscopic measurements performed on acetylene gas performed by my hosting group after this collaboration [5].

We used a custom Matlab script to simulate the cavity mode evolution as function of the geometrical parameters of the resonator. The curved mirror and the lengths of the cavity branches have been chosen following ABCD matrix simulation of the resonator. As a design target, the cavity mode has been shaped in order achieve the proper spot size in the gain crystal and on the second ending mirror (S). The basic theory of the ABCD matrices and the results obtained for the design of this resonator are reported in Annex C.1. We identified a mode radius of 60 µm in the gain crystal and 100 µm on S as optimal working conditions. In detail, the intracavity beam size on S will be actually needed for the mode locking operation that will be detailed later in this Section. A dichroic mirror exhibiting high reflectivity @ 1050 nm and high transmission @ 970 nm separates the pump beam and the oscillator output. We route the laser output toward our custom diagnostic stage that has been prepared to monitor and characterize several properties of the laser performances. The results of these characterizations are shown in the next Section (Ch. 5.2). Once we identified the most promising configuration of our oscillator for the CW operation (Fig.15), we changed the S from a standard high-reflectivity dielectric mirror to a semiconductor saturable absorber mirror (SESAM). This device is the key element to passively mode-locked the laser emission, thanks to its intensity-dependent nonlinear reflectivity. The higher the intensity the higher the reflectivity so, laser operation in which the longitudinal modes constructively interfere is favored [6]. It has been designed and fabricated in-house and its saturation fluence and modulation depth were 21 µJ/cm^2 and 1.2% respectively. The SESAM has been mounted on a copper holder fixed on a heat sink to remove excessive heat through air convection, whereas its temperature has been stabilized via Peltier cooling.

Then, we employed Gires-Tournois Interferometer (GTI) mirrors to introduce the wavelength-dependent phase shift. The engineered structure of these mirrors introduces a certain amount of negative Group Delay Dispersion (GDD) used to balance the broadening effect of the Self-Phase Modulation (SPM). A more detailed explanation of the design constraint for the mode locking regime is given in Appendix C. The mirrors employed in the cavity are actually GTI mirrors, acting so as lumped stages for introducing the negative GDD. In the optimal-configuration we tested, the overall negative GDD introduce in a complete roundtrip was -800 fs^2.

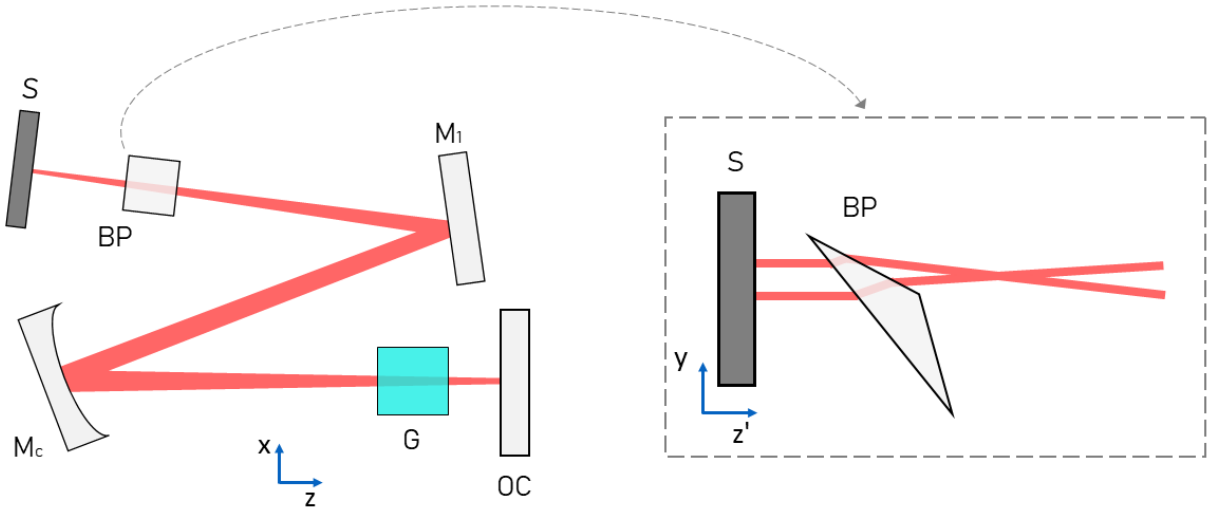

Figure 15 – Schemes of the z-shaped cavity. OC: Output Coupler, G: Gain Crystal, Mc: Curved Mirror, M1: Cavity Mirror, S: Ending Cavity Mirror (replaced with the SESAM for the ML and DCL operation), BP: Brewster-oriented biprism (179° apex angle), The intracavity biprism is oriented such that the Brewster condition is obtained for vertically polarized light. The beams transmitted through the two facets are deflected vertically as shown in the dashed box.

Then, we modify the setup in order to achieve the dual-comb operation. These variations included an alteration of the stage used to deliver the pump radiation to the cavity and the insertion of an intracavity biprism (BP). The pump beam has been sent into a pump routing stage, intended to be used for pumping to twin regions in the gain crystal. Each pumped area is necessary to generate a comb beam. A 50:50 beam splitter separates the pump radiation into two identical parts. So, we needed to double the overall output power delivered by our pump diode in order to reach the same performance we verified in the mode locking regime with a single lasing beam. The two components have been separated in the vertical direction and redirected in the gain crystal and a 4-f telescope provides unitary magnification of the fiber core size. Then, a biprism working in transmission has been used as a multiplexing element. It has been introduced in the cavity as shown in the dashed box in Fig. 15. With this pumping geometry, the two pumped regions are separated in the vertical direction. Therefore, the light beams they generate experience different optical paths when they propagate through the biprism. Indeed, the biprism thickness in the propagation direction is function of the vertical position because of its wedged geometry. The small amount of difference in the overall roundtrip length is enough

to provide a slightly different repetition rate, as the two combs experience different cavity lengths, as stated by eq. 20.

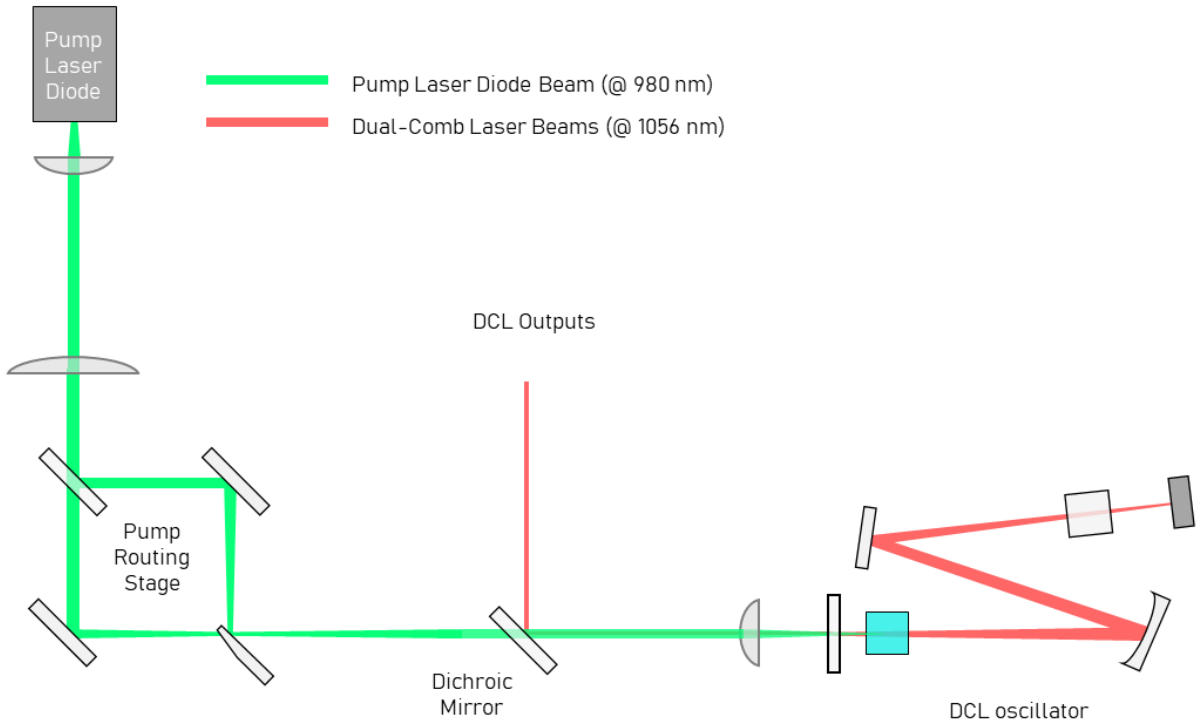

Figure 16 – Scheme of the complete optical setup of the DCL oscillator. The pump routing stage split the pump radiation into two identical and parallel beams, separated in the vertical direction.

Moreover, the biprism has been mounted on a translation stage to control its vertical position. Therefore, the amount of shift between the two repetition rates can be tuned by moving the biprism vertically. The DCL oscillator emits two vertically separated but parallel laser beams. Their optical properties have been analyzed with the same diagnostic setup used to characterize the mode-locking operations. The main difference consists in the measurement procedure that required the characterization of each comb separately.

4.2 - Characterization of the laser oscillator

The optical properties of the laser emission have been monitored with a diagnostic setup made by several stages. A commercial power meter (Uno, Gentec, US), optical spectrum analyzer (indicated as OSA, 70004A, HP, US) and coupled-charged device camera (CCD, WincamD, DataRay Inc, Us) have been used to monitor the output power, the spectrum and the spatial profile of the laser beam respectively. A wedged prism and a partially reflective mirror have been used to split the beam into attenuated replicas that are feeding each instrument. The most intense portion has been measured with a thermal sensor which may handle high power levels (UP19K-30H-H5-D0, Gentec, US), whereas the two weaker reflections have been redirected toward the OSA and the CCD. A slightly different setup including the detection of the radio frequency (RF) spectrum and the pulse duration has been implemented for the mode-locked and dual-comb operating regimes. We used a microwave spectrum analyzer (also named MSA,

8592L, HP, US) coupled with a fast photodiode (1014, NewFocus, US), a preamplifier (87405C, Agilent, US) and a DC blocker to characterize the RF spectrum. The pulsewidth have been measured by means of an optical autocorrelator (FR-103MN, Femtochrome Researc Inc., US) and a digital oscilloscope (TDS 3052B, Tektronix, US) have been used to monitor the repetition rate signal and the pulse duration respectively. The schematic of such a diagnostic setup has been reported in Fig. 17.

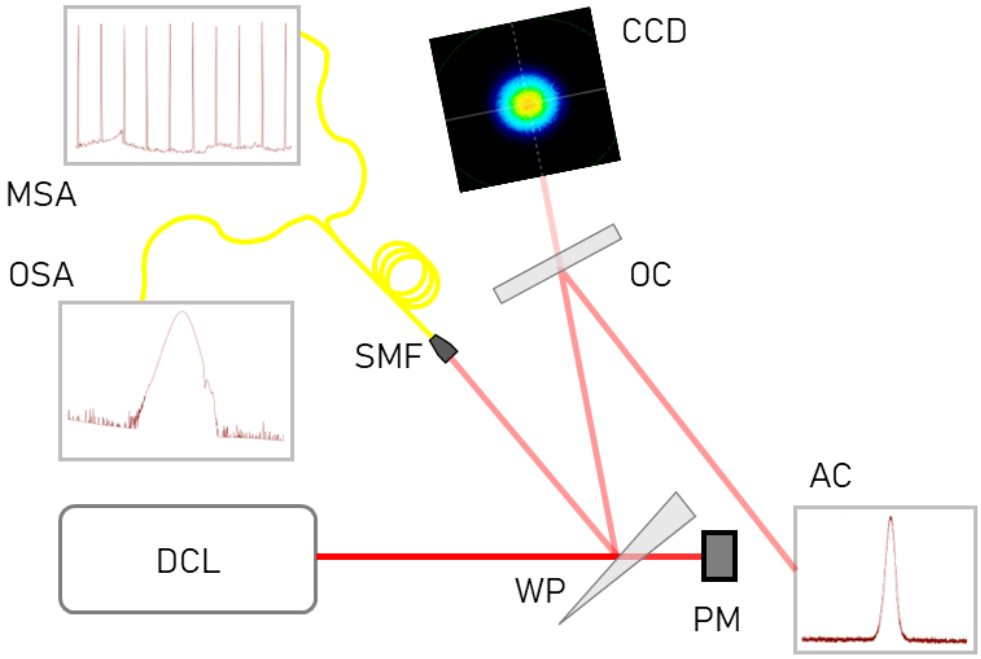

Figure 17 - Scheme of the diagnostic setup used to perform the optical properties of the laser beam. Most of the power is detected with a power meter (PM) which is monitoring the output power. One portion of the light beam is coupled with a single mode fiber (SMF) to feed the OSA and MSA. The other attenuated component is further attenuated and directed toward the beam profiling CCD and the optical autocorrelator (AC)

We characterized such optical properties as function of the pump power and such characterizations are reported in Fig. 18-23.

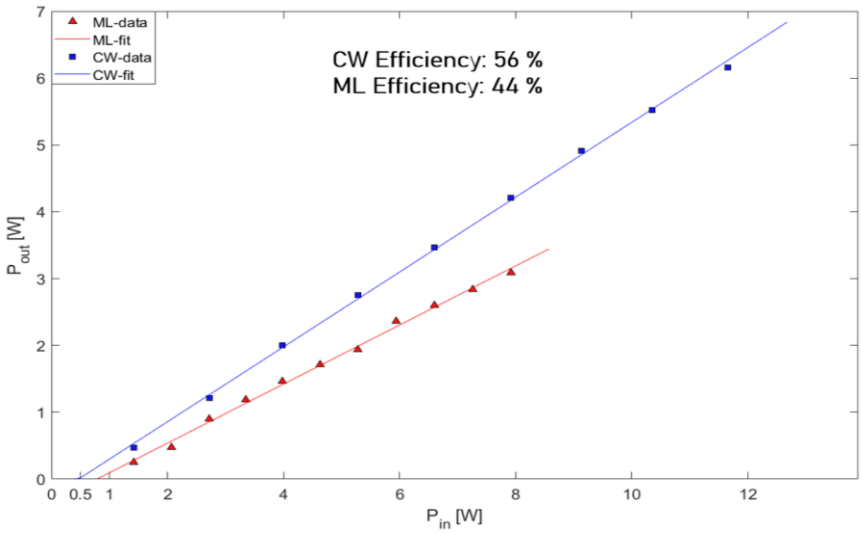

Figure 18 - Experimental data and linear fit of the laser P_{in}-P_{out} characteristics in the two different regimes.

Fig.18 shows the variation of the output power of our oscillator as function of the pump power for both the operating regimes. A mode locked laser beam with 3 W of output power is emitted by pumping with a power of 8 W. The output spectra of the CW and ML operating regimes are shown in Fig.19. It can be clearly seen the broadening of the bandwidth whose width is increased from less than 1 nm up to 10 nm. The trigger of the ML operation causes the in-phase oscillation of several longitudinal modes, leading so to the grater optical bandwidth necessary to sustain the ultrashort pulses.

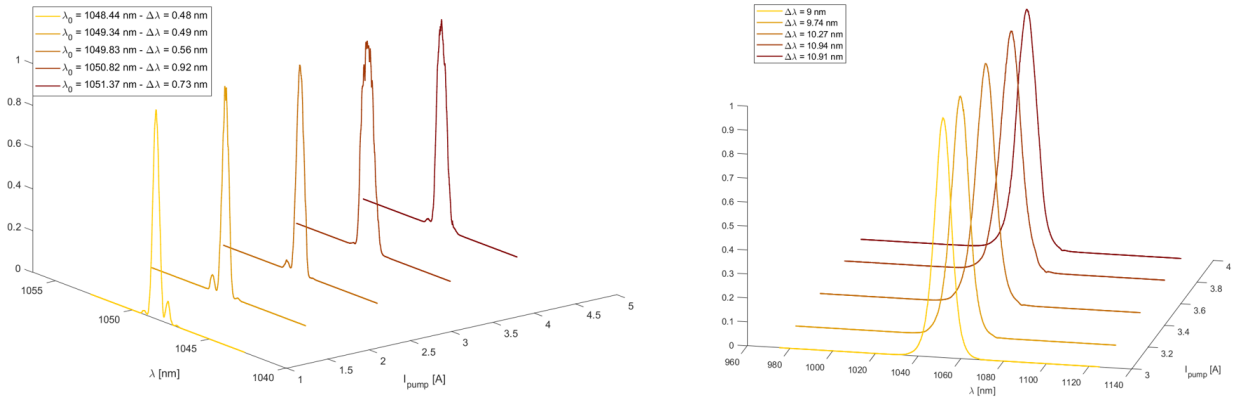

Figure 19 – The optical spectra at different pumping levels in the two different regimes of emission (CW on the left and ML on the right) clearly shows the widening of the spectral bandwidth.

The broad optical bandwidth of the ML regime is related to ultrashort pulse duration. Moreover, the soliton regime is achieved as we can see from the left panel in Fig.19. It is showing the values of the time-bandwidth product close to the Fourier limited value predicted for a sech^2 pulse.

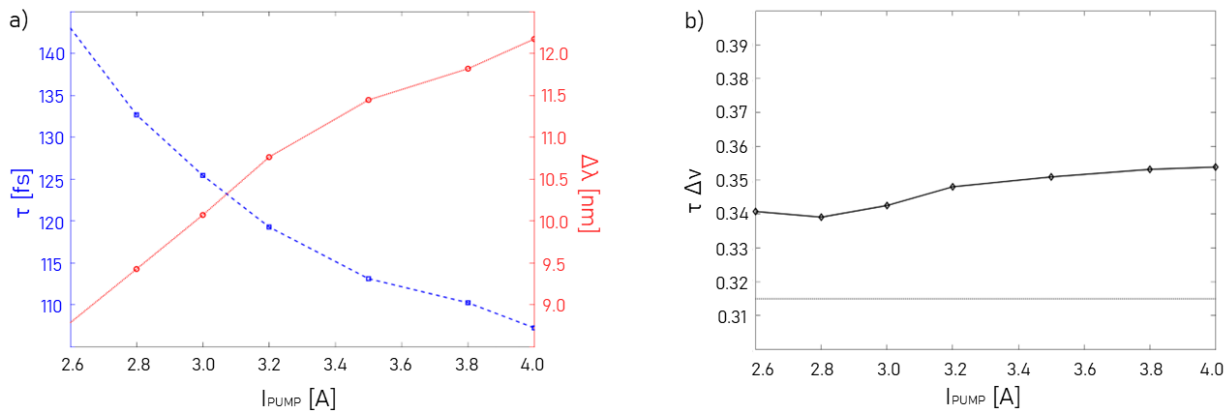

Figure 20 - a) Autocorrelation traces used to characterize the pulse duration as function of the pump current. Plot b) and c) shows the relation between the optical bandwidth and the pulse duration, whose product is close to the theoretical limit value of 0.315 for sech2-shaped pulses

Finally, we characterized the radiofrequency signal generated by the repetition rate (f_r) of the ultrashort pulse train. The clean radiofrequency spectrum of f_r and its harmonics are shown in Fig.21.

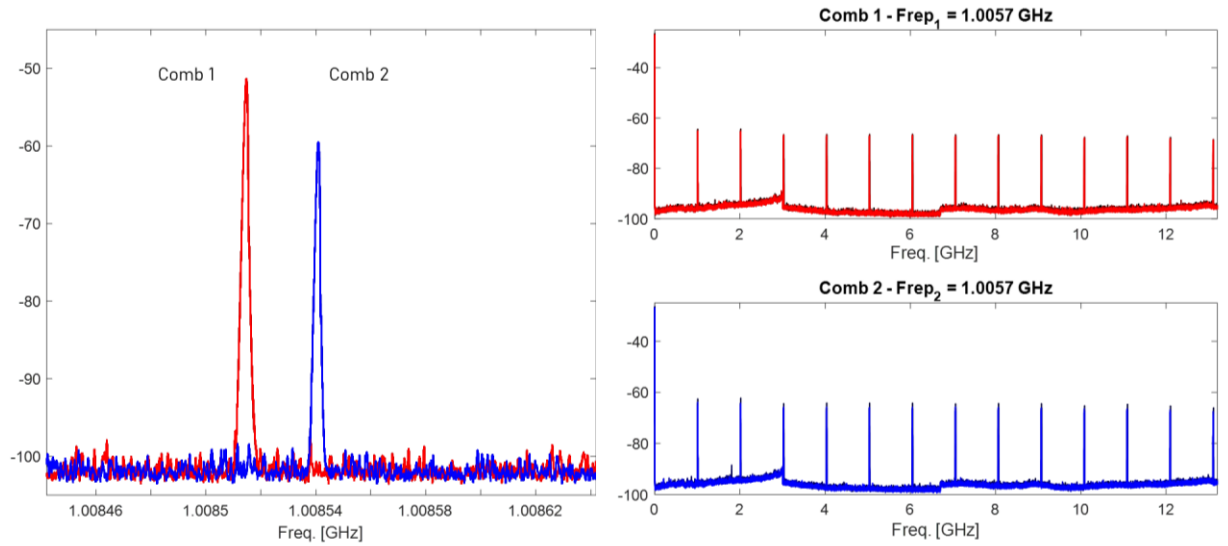

Figure 21 – Amplitude of the RF spectra of the two combs (red and blue) measured with the MSA. The zoom of their first harmonic shows the frequency difference (Δf_r) between their repetition rates (left panel, resolution bandwidth = 300 kHz). The whole RF spectra of the two individual combs (right panels, resolution bandwidth = 30 kHz) shows the clean signal of the higher order harmonics of f_r.

Then we characterized the performances of the oscillator operating in the dual-comb regime. Each characterization of the laser emission features has been performed on the individual comb beam. The similarities of the optical properties of the two combs are shown in Figs.21-23. Both beams have almost identical bandwidth, power and pulse duration and the main difference relies in their repetition rate. The presence of the intracavity biprism as multiplexing elements cause a repetition rate difference (Δf_r) that can be clearly seen around their first harmonic at ~1 GHz (Figure 21). The amount of Δf_r can be tuned by moving the vertical position of the biprism within

a certain range. We observed the laser operations were not affected while Δf_r has been tuned in the range 0-27 kHz. Above or below such values, the lasing of one of the two beams was inhibited because during its oscillation it travel through one of the edges of the biprism, increasing the losses it experiences. The limited physical extension of the prism limits the tunability range of Δf_r.

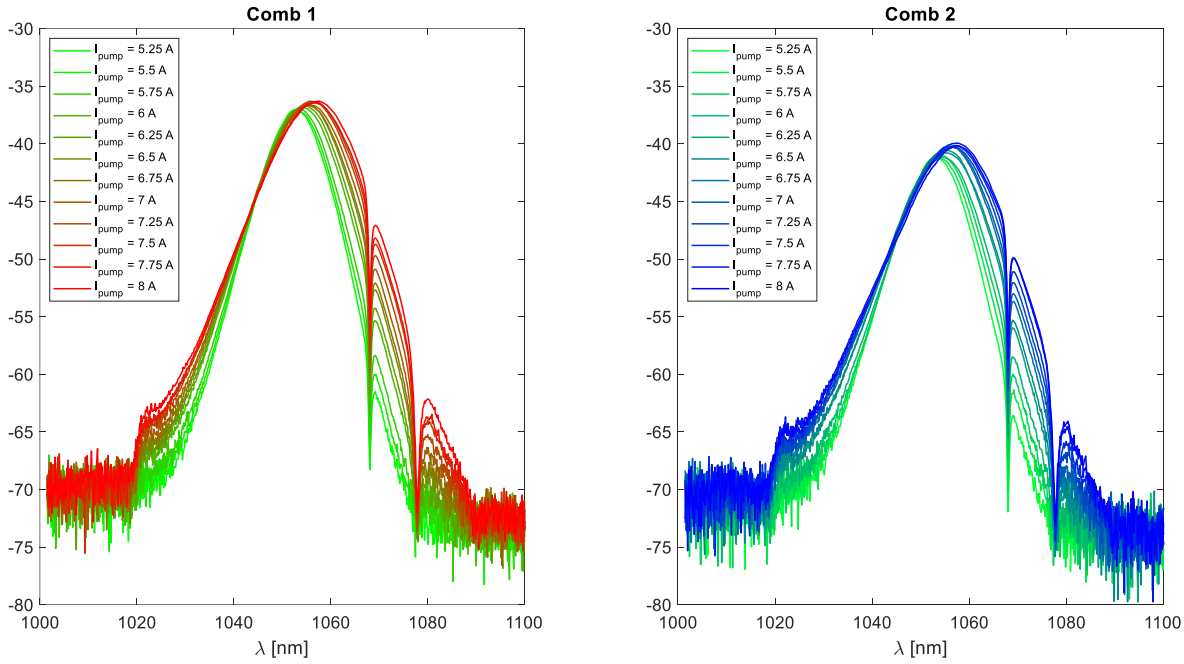

Figure 22 - Semilogarithmic representations of the optical spectra of the two combs at different pumping levels

I want to highlight the presence of some spectral dip in the optical spectra at 1068 nm reported in Fig. 15-16. This issue was present in the DCLs output because of a small misalignment of the birefringent element in the cavity (i.e., the active medium). A further development of the laser source was done to improve the alignment and the spectral dip at 1068 nm disappeared. The cleaner spectrum and the other feature of the laser emission after this improvement are reported in [5]. In short, the overall width of the laser spectra increased from 12 to 15 nm after the removal of that dip.

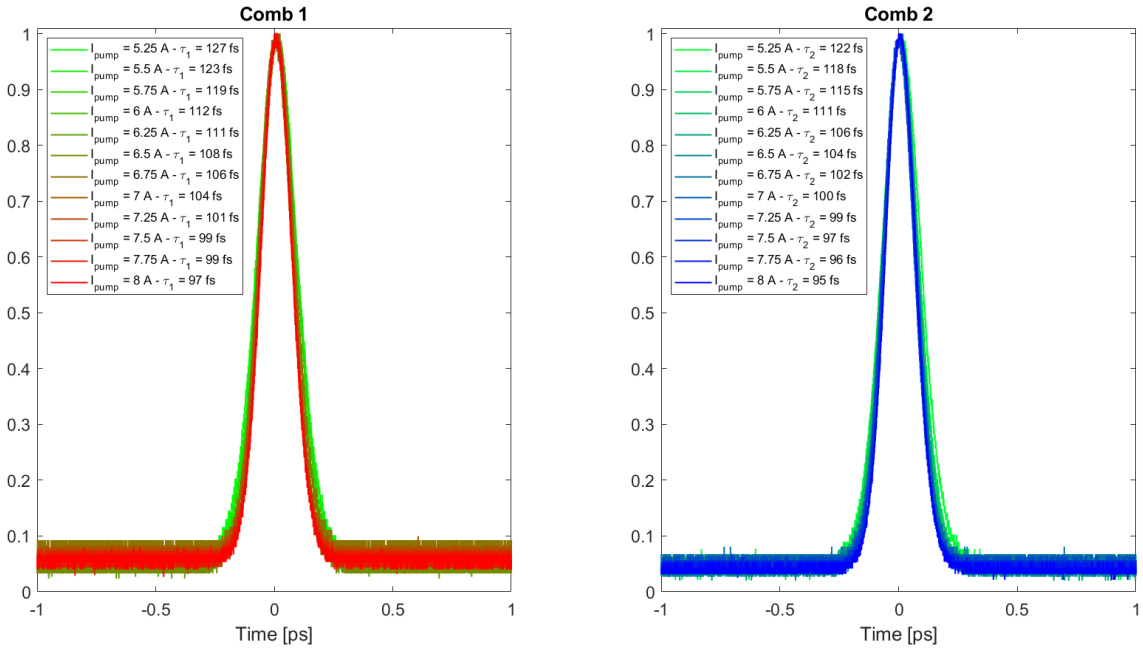

Figure 23 - Temporal traces recorded with a commercial autocorrelator showing the variation of the pulsewidth as function of the pumping current.

Even the temporal feature of the pulse benefitted from the removal of the spectral dip. Indeed, the pulse duration of the two combs has been reduced from 100 fs (as reference value of the characterizations reported in Fig. 23) to 78 fs with a total pump power of 18.5 W.

4.3 - Broadband characterization of optical anisotropies

Once the DCL has been assembled and characterized, we used its optical emission to realize a sensing technique for the characterization of the optical anisotropies of sample within the whole output spectrum of the laser. This method exploits the mutual coherence of the two combs to generate a pair of interferometric signals through self-mixing. The interference between two mutually coherent OFC provides a direct link between the radiofrequency spectrum and the optical spectrum and it has been exploited in several spectroscopic applications [3], [4]. Here, I report from the Chapter 2.3 the time and frequency description of the electric field associated with the DCL.

Eq. 22) $E_k(t) = \left(A(t) \cdot e^{i\omega_{0,k}t}\right) * \left[\sum_n \delta\left(t - nT_{R,k}\right) \cdot e^{i\omega_{CEO,k}t}\right] + c.c.$

Eq. 23) $\tilde{E}_k(\omega) = \left(\tilde{A}\left(\omega - \omega_{0,k}\right)\right) \cdot \left[\sum_n \delta\left(\omega - n\omega_{R,k} - \omega_{CEO,k}\right)\right] + c.c.$

In a DCL, the coherence between the two beams with different index (k=1,2 for comb 1 and 2 respectively), grants they can interfere. Their superimposition results in an interferograms train and its intensity is described by Eq. 23.

Eq. 24) $i(t) = |E_1(t) + E_2(t)|^2 \propto \sum_n cos(n\Delta\omega_r t)$

Where $\Delta\omega_r = \omega_2 - \omega_1$ is the repetition rate difference between the two combs ($\Delta\omega_r = 2\pi\Delta f_r$). Considering our oscillator, it emits two pulse trains with a repetition rate of 1 GHz and their

difference is tunable from 0 to 27 kHz. Therefore, the photocurrent in eq. 23 contains the harmonics of $\Delta\omega_r$ whose value is in the RF and it can be detected with relatively simple electronics components, such as photodiodes and BNC cables. In addition, since its spectrum is the down-converted replica of the optical spectrum described in eq. 22., the variations of the optical spectrum can be detected without relying in bulky and expensive instruments (such as spectrometers or optical spectrum analyzers).

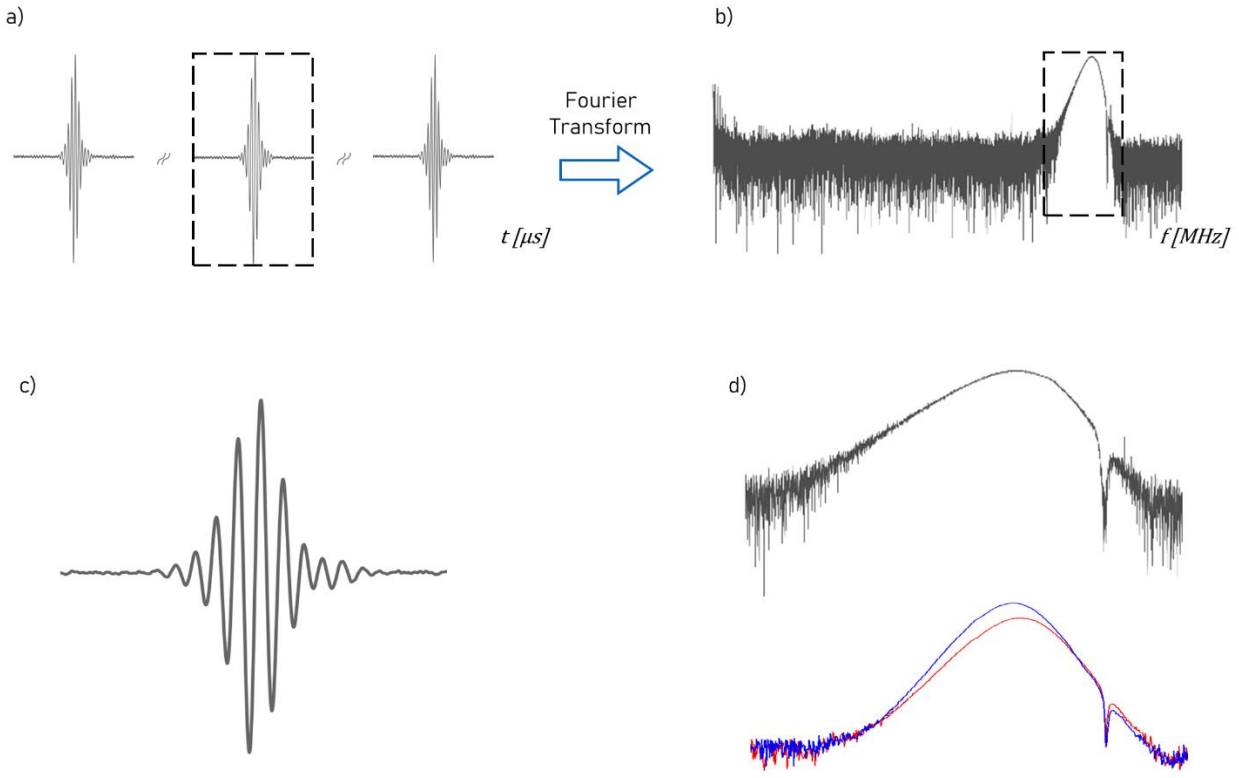

Figure 24 – The interferograms train generated through the self-mixing of the two combs a) and the zoom of a single interferogram c). The associated RF spectrum obtained by Fourier-transforming the measured photocurrents. The similarity between the RF spectrum (grey) and the optical spectra of the two combs (red and blue) is evident in d).

We added the vectorial description of the light beams to this approach by playing with the polarization state of the two combs. When two orthogonally polarized laser beams with a slightly different optical frequency interact with a sample, a beating signal containing information about the polarization response of the sample can be detected with a heterodyne scheme. This is the principle exploited in the measurements of the Mueller Matrix coefficient encoded in the RF beating of the emission of the Zeeman Laser already explained in the Ch.4 [7], [8]. In that scenario, two well-defined laser lines, generated by triggering the Zeeman effect in the active medium, are both emitted as two overlapped CW laser beams. Their polarization state is orthogonal and the breaking of such orthogonality relation generates a time-evolving polarization state. Such combined polarization state can be described as a time-varying Stoke vector and the frequency of such variation is the frequency difference between the laser lines. This beating interaction can be exploited also by generating many beating signals rising from

the interference of the several discrete spectral lines of a pair of OFCs. So, we can think about this approach as a parallelization in the spectral domain of the method implemented with the DFDP laser.

The Dual-Comb emission realized with these laser sources can be used to have a spectral signature of the Mueller coefficients encoded in the polarization-resolved self-mixing signals. As in the case of the Zeeman laser, such approach allows to merge the role of the Polarization State Generator with that of the illumination source to perform this type of polarization measurement. The scheme in Fig. 25 shows the setup I realized to perform such measurements with our custom-built DCL source. The two beams emitted by our DCL are mitted parallelly, with a tiny space separation and with the same polarization state. We steered them toward an optical setup realized to change independently their polarizations and to combine them.

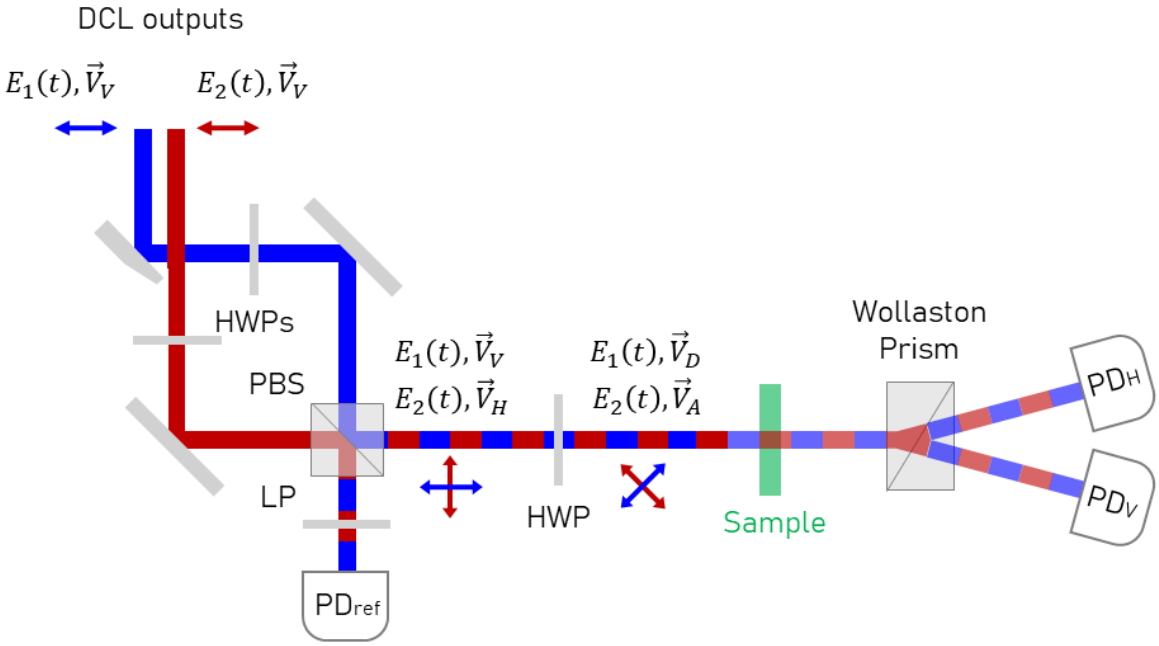

Figure 25 - (a) Comb 1 ($E_1(t)$ in blue) and comb 2 ($E_2(t)$ in red) with their respective polarization states (double-sided arrows). The labels with the $E_k(t), \vec{V}_k$ pairs describe the evolution of the polarization state associated with the k-th comb at different stages of this optical setup.

We set them in two linear and orthogonal states by using a half-wave plate (HWP) placed in each arm of the setup shown in Fig. 25. Then they have been combined by means of a polarizing beam splitter (PBS) whose main axes are matched with the direction of the two input states (0°-90° for the H-V polarization). The final beam is the overlap of two orthogonally polarized beams, each one associated with an OFC. Then we rotated the polarization of the combined combs at ±45° with the respect to the PBS axes by using another HWP placed after it ($[J_{HWP}]$). The final cross-polarized state can be described with Eq. 24.

Eq. 25) $E_{in}(t) = [J_{HWP}] \cdot (E_1(t) \cdot \vec{V}_V + E_2(t) \cdot \vec{V}_H)$

Where $E_1(t), E_2(t)$ are the electric field associated with the two combs. Each pair of comb lines associated with the same index n in this state has a Stokes vector that can be described by Eq. 25.

Eq. 26) $\vec{S}_{in,n} = \begin{bmatrix} S_{1,n} \\ S_{2,n} \\ S_{3,n} \\ S_{4,n} \end{bmatrix} \propto \begin{bmatrix} 1 \\ cos(n\Delta\omega_r t) \\ 0 \\ sin(n\Delta\omega_r t) \end{bmatrix}$

The repetition rate difference between the two combs determines the rate of variation of the overall polarization state. The n-th pair of spectral components generates a contribution to the overall polarization state that is oscillating at $n\Delta\omega_r = n2\pi\Delta f_r$. We assumed the value of Δf_r (tunable from 0 to $27\ kHz$) is such that $\Delta f_r \ll f_r$ (that is equal to $1\ GHz$) in eq. 21 and that there is no carrier-envelope offset frequency difference for simplicity. As anticipated in the previous section, the repetition rate difference can be tuned by moving the biprism along the vertical position with the respect to the cavity axis. For the following polarimetric characterization, we move it to set $\Delta f_r \approx 2\ kHz$. The optical anisotropies of the samples modify the polarization state in Eq. 25 while the cross-polarized light travels through it. Finally, a couple of fast photodiodes (DET01CFC, Thorlabs, US) aligned on the two outputs of a Polarization State Analyzer (PSA) are used to detects the variation of the polarization state. The Wollaston prism used as PSA is aligned at 0°-90° so, it breaks the orthogonality of the cross-polarized combs even when the sample is purely isotropic. Therefore, the polarization states of the two combs are projected onto the same planes so, they can interfere. The overall evolution of the polarization state within this final stage of the optical setup is described by Eq. 26.

Eq. 27) $\overrightarrow{S_{OUT}^{H-V}}(t) = [M_{PSA}^{H-V}] \cdot [M_S] \cdot \vec{S}_{in}$

Where the superscript $H-V$ indicates the output channel of the Wollaston prism associated with the H and V polarization component, respectively. The photodiodes detect a couple of photocurrent signals describing the interferogram trains generated by the self-mixing interference of the two combs. The generation of these signals is modeled with the Stokes-Mueller formalism and their analytical expression is defined by Eq. 27. We analyze the associated photocurrents $i_k(t)$, proportional to the first element of $\overrightarrow{S_{OUT}^{H-V}}(t)$. Each pair of spectral lines in the two combs with the same index n, gives rise to a beating component in the photocurrent signal, as stated by eq. 27.

Eq. 28) $i_n^k(t) \propto a_n^k + b_n^k \cdot cos(n\Delta\omega_r t) + c_n^k \cdot sin(n\Delta\omega_r t)$

The analysis of these photocurrent signals leads to the identification of six Mueller coefficients similarly to what has been explained in the Ch.4 in the method developed with the Zeeman laser. Indeed, the coefficients $a_{k,n}^{H-V}, b_{k,n}^{H-V}, c_{k,n}^{H-V}$ are sum and differences of Mueller coefficients and the sign of their linear combinations depends by the output channel of the PSA ($H \to +, V \to -$).

Eq. 29) $a^k(\omega) = a_n^k = m_{11}(\omega) \pm m_{21}(\omega)$
Eq. 30) $b^k(\omega) = b_n^k = m_{12}(\omega) \pm m_{22}(\omega)$

Eq. 31) $c^k(\omega) = c_n^k = m_{13}(\omega) \pm m_{23}(\omega)$

This method allows to identify the values of such Mueller coefficients within the whole RF spectrum associated with the interferograms. The Fourier transformation of the photocurrent in eq. 27 allows the spectral reconstruction of the Mueller coefficients in the RF range. As anticipated, the signals generated by the interference of the DCL radiation are linked to the laser optical spectrum. Therefore, the Fourier transform of each interferograms represents a frequency-shifted replica of the laser spectrum in the radiofrequency range. Similar approaches have been reported in [9], [10] but none of them have been implemented by exploiting a single-cavity dual-comb laser.

We repeated the same validation experiments performed with the Zeeman Laser to validate this polarimetric sensing method. A polarizing optical element has been used as a reference sample to perform the polarimetric characterization of its transmission while its azimuthal angle has been varied. I recorded three interferograms for each measurement and each recording have been performed by rotating the sample by 10°. Two signals are coming from the polarization-resolved measurement stage whereas the third photodiode detects an unperturbed portion of the beam that is used as a reference. A linear polarizer at 45° generates the signal used as a reference in the scheme of Fig. 25. The photocurrent signals have been recorded by means of three fast photodiodes and their time-trace has been stored by using a commercial oscilloscope. I analyzed the spectral content of these temporal traces by using a Python script performing the Fourier analysis on them. Through the Fourier transform, the dual description of the photocurrent spectrum allows to describe the spectral response of the Mueller coefficients, as shown eq. 31.

Eq. 32) $I^k(\omega) \propto A^k + \sum_n (\delta(\omega - n\Delta\omega_r) \cdot (B_n^k + jC_n^k))$

The three amplitude terms (A^k, B^k, C^k) of the photocurrent harmonics are linked to the Mueller coefficients of the sample. As a reference sample (indicated in green in Fig. 25) I used a zero-order quarter waveplate (WPQ05M-1053, Thorlabs, USA). When a sample does not contain any anisotropy, the signals detected can be described by the eq. 23 (that is eq. 27 with $c_n^k = 0$). The Fourier spectra associated with the signals detected in such condition are an exact replica of the optical spectra of the two combs in the RF range. Conversely, if the sample alters the light polarization, the Fourier-transformed interferograms are modified with the respect of that condition. The value of the Mueller coefficients is affected by the presence of an amplitude or phase modulation term in the optical response of the sample.

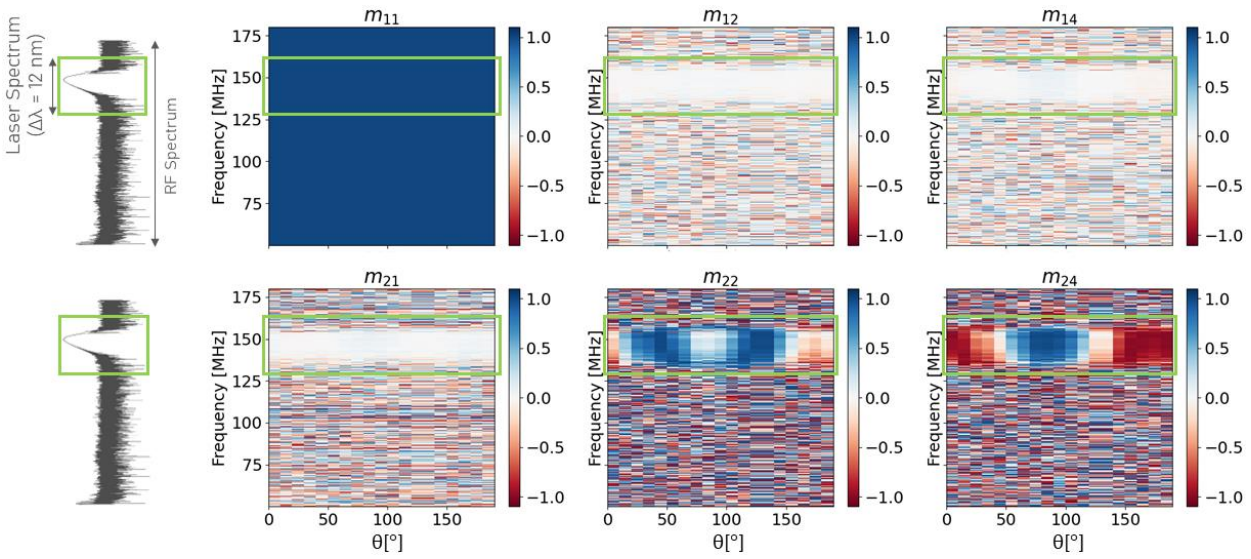

Figure 26 – The left side of this panel reports the amplitude of the Fourier transform of the detected signals containing the polarization fingerprint of the QWP. The green boxes highlight the variation of the values of the Mueller coefficients vs the azimuthal angle of the optics in the spectral region of interest.

The spectral maps in Fig. 26 represents the frequency response of the Mueller coefficient of the quarter-wave plate as function of its azimuthal angle. The spectral region highlighted in the green box corresponds to the RF band between 135 and 160 MHz. As explained before, the DCL output spectra with 12 nm full width half maximum is down-converted into these spectral range through interference. The red and blue optical spectra of the two combs have been already reported in Fig. 24-d, below the associated RF spectrum. There is a narrow spectral region with low laser power, as it can be seen at the spectral dip around 155 MHz. The low signal level at this frequency hinders a proper identification of the Mueller elements at that frequency. Indeed, values of the Mueller coefficients at this frequency is noisy as for the frequency out of the laser bandwidth i.e., outside the 135 and 160 MHz band.

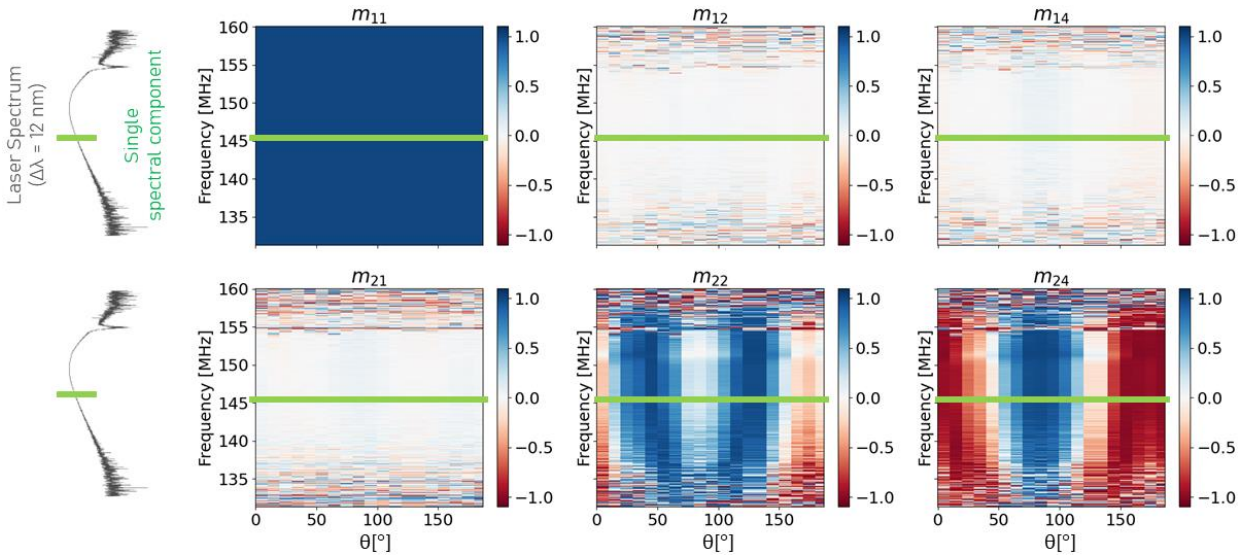

Figure 27 – Spectral map of the Mueller coefficients vs the azimuthal angle of the QWP zoomed in the spectral region of interest corresponding to the optical spectra of the two combs. The green line refers to the frequency used to evaluate the Mueller coefficients in the plots reported in Fig. 28

The m11 element is used for normalization since it corresponds to the total collected light. Mueller coefficients associated with dichroism (m_{12}, m_{21}, m_{14}) are null, as expected for a purely retarding plate. Conversely, those associated with depolarization and linear birefringence (m_{22}, m_{24}) exhibit the sinusoidal variation as expected with a birefringent waveplate. The description of this elements as function of the angle has been reported in Annex A.

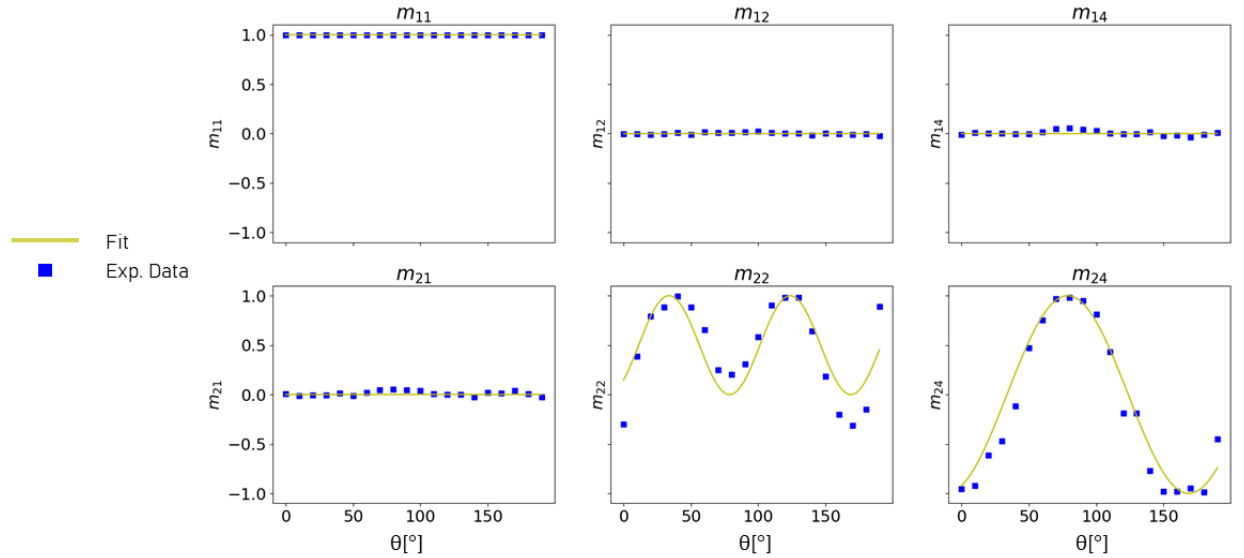

Figure 28 – Comparison between the Mueller coefficient identified with the spectral reconstruction at a single frequency and the theoretical value. Similar plots can be obtained for each frequency in the spectral maps in Fig. 27.

4.4 - Conclusion

DCLs are employed in several spectroscopic applications requiring fast and precise spectral measurements. We developed a custom-built single-cavity DCL with GHz repetition rate and 3 W of output power for each comb. We exploit the optical radiation of this laser source to develop a method for measuring the optical anisotropies of samples. This approach exploits the fast modulation of the polarization state encoded in the interferogram generated by self-mixing the spectral components of the two combs. This method does not require the use of any external device to manipulate the polarization state and it can be applied to any DCL source. Moreover, the dual-comb spectra can be broadened and shifted using nonlinear optical conversion stage to achieve different spectral region with distinctive fingerprint. Both spectral and timing properties of DCL emission allow the implementation of several spectroscopic investigations simplifying the structure of the measurement setup. Therefore, DCLs can be used to develop a multimodal sensing platform combining different techniques to probe different physical properties of samples. The rich content of the electromagnetic field of a DCL provide several degrees of freedom in the beam properties. Therefore, it is possible to tailor the laser light generated by such devices in other ways. In particular, these sources have been also exploited to develop innovative optical imaging techniques [11], [12]. Thanks to the compactness and the cost reduction achievable through the single-cavity design, it is reasonable to expect the spreading of such devices in several application fields.

References

[1] P. O. Petit, J. Petit, P. Goldner, and B. Viana, "Inhomogeneous broadening of optical transitions in Yb:CaYAlO4," *Opt. Mater. (Amst).*, vol. 30, no. 7, pp. 1093–1097, 2008, doi: 10.1016/j.optmat.2007.05.017.

[2] P. Loiko, F. Druon, P. Georges, B. Viana, and K. Yumashev, "Thermo-optic characterization of Yb:CaGdAlO_4 laser crystal," *Opt. Mater. Express*, vol. 4, no. 11, p. 2241, 2014, doi: 10.1364/ome.4.002241.

[3] S. Schiller, "Spectrometry with frequency combs," *Opt. Lett.*, vol. 27, no. 9, p. 766, 2002, doi: 10.1364/ol.27.000766.

[4] I. Coddington, N. Newbury, and W. Swann, "Dual-comb spectroscopy," *Optica*, vol. 3, no. 4, p. 414, Apr. 2016, doi: 10.1364/OPTICA.3.000414.

[5] C. R. Phillips *et al.*, "Coherently averaged dual-comb spectroscopy with a low-noise and high-power free-running gigahertz dual-comb laser," *Opt. Express*, vol. 31, no. 5, p. 7103, 2023, doi: 10.1364/oe.479356.

[6] U. Keller, *Ultrafast Lasers*. Cham: Springer International Publishing, 2021.

[7] W. M. McClain, W.-H. Jeng, B. Pati, Y. Shi, and D. Tian, "Measurement of the Mueller scattering matrix by use of optical beats from a Zeeman laser," *Appl. Opt.*, vol. 33, no. 7, p. 1230, 1994, doi: 10.1364/ao.33.001230.

[8] F. Callegari, A. Le Gratiet, A. Zunino, A. Mohebi, P. Bianchini, and A. Diaspro, "Polarization Label-Free Microscopy Imaging of Biological Samples by Exploiting the Zeeman Laser Emission," *Front. Phys.*, vol. 9, no. October, pp. 1–8, 2021, doi: 10.3389/fphy.2021.758880.

[9] K. A. Sumihara, S. Okubo, M. Okano, H. Inaba, and S. Watanabe, "Polarization-sensitive dual-comb spectroscopy," *J. Opt. Soc. Am. B*, vol. 34, no. 1, p. 154, Jan. 2017, doi: 10.1364/JOSAB.34.000154.

[10] T. Minamikawa *et al.*, "Dual-comb spectroscopic ellipsometry," *Nat. Commun.*, vol. 8, no. 1, 2017, doi: 10.1038/s41467-017-00709-y.

[11] T. Mizuno *et al.*, "Full-field fluorescence lifetime dual-comb microscopy using spectral mapping and frequency multiplexing of dual-comb optical beats," *Sci. Adv.*, vol. 7, no. 1, pp. 1–12, Jan. 2021, doi: 10.1126/sciadv.abd2102.

[12] E. Vicentini, Z. Wang, K. Van Gasse, T. W. Hänsch, and N. Picqué, "Dual-comb hyperspectral digital holography," *Nat. Photonics*, vol. 15, no. 12, pp. 890–894, Dec. 2021, doi: 10.1038/s41566-021-00892-x.

5 – Mueller matrix microscopy with the Zeeman Laser

This section shows the realization of the custom Mueller matrix microscope realized with the Zeeman Laser as both illumination stage and Polarization State Generator. The dual-frequency, dual-polarization emission of such device has been exploited to encode the polarimetric fingerprint of the specimens in a laser-scanning architecture. The interferometric signals rising from the beating of the two optical components of the ZL have been detected by two single-element detectors. Finally, the harmonic contents of the photocurrent signals have been analyzed to extract the information about individual Mueller coefficients and to form the associated images. This Chapter shows the development of this imaging platform and the imaging results obtained on anisotropic biological samples.

5.1 – Microscope development

The realization of a Mueller matrix microscope requires two main stages to the architecture of a generic optical microscope, namely a Polarization State Generator and an Analyzer (PSA). The scheme reported in Fig. 29 shows the general scheme of such an imaging instrument.

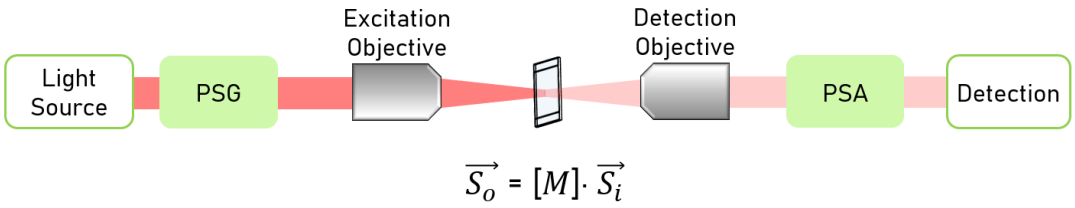

Figure 29 - Typical scheme of an optical microscope where the two stages dealing with the handling of the polarization state (PSG and PSA) are highlighted (in green)

There are many generation and analysis strategies in terms of multiplexing the polarization information and probe the sample with different states. The main approaches exploit spectral, spatial or temporal multiplexing of the polarization states. However, the single-element detector used in a laser-scanning microscope introduces a constraint in the encoding strategy of the polarization states. Both the spatial and spectral information are averaged if a simple single element detector is used. Array detectors in combination with other optical elements can overcome this limitation but at the expense of the simplicity and compactness of the system. Therefore, I choose to exploit the generation in time of different polarization states to perform Mueller matrix imaging in our laser scanning microscope. This approach has been also widely used in several optical setups exploiting an external device to perform the function of PSG [1]. As anticipated, the Zeeman Laser can perform both the role of the light source and the PSG. Its optical emission is made by two orthogonally polarized components with a tiny frequency shift. When the orthogonality between these two components is broken, for instance by the sample anisotropies and then by the PSA, these two components can interfere. The analysis of the interferometric signals lead to the identification of the Mueller coefficients describing the polarimetric response of the sample. The PSA used here is made by a simple Wollaston prism. This passive optical device acts as a polarizing beam splitter where the two-output channels are separated with a certain angle (±10° with the respect to an input ray at normal incidence at

633 nm). The polarization of the incoming light altered by the specimen is projected into two orthogonal components with a high polarization extinction ratio (100'000:1). Fig. 30 shows the complete optical setup of the laser-scanning microscope I realized to perform Mueller imaging.

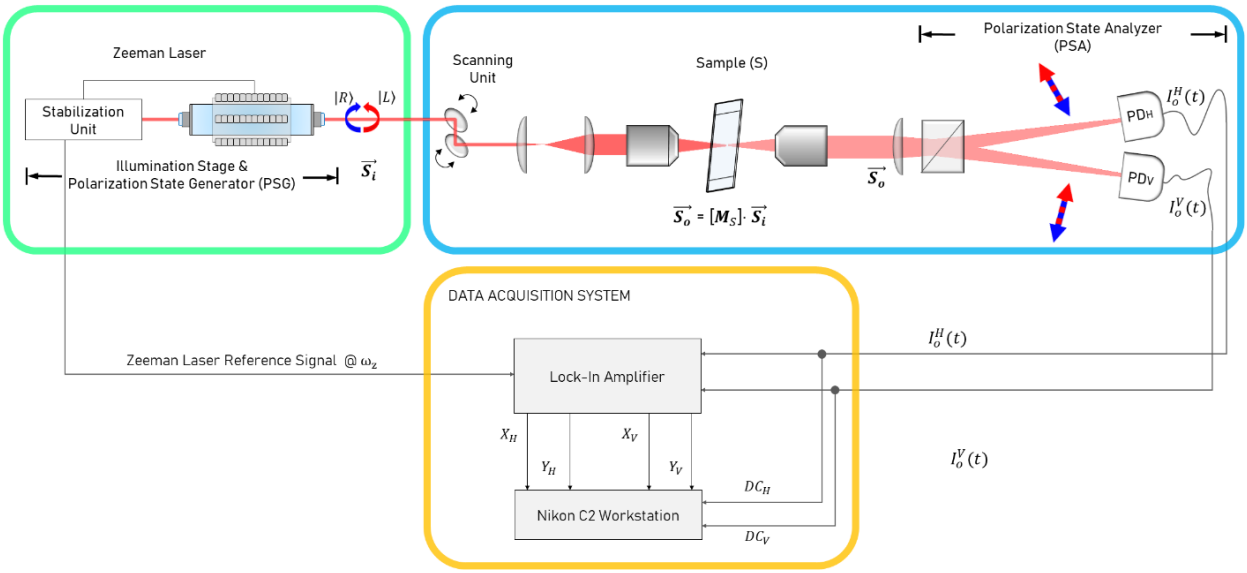

Figure 30 - Scheme of the laser scanning microscope use to perform Muller imaging. In green, the illumination source acting also as PSG. Then, the blue box contains the optoelectronic components of the imaging instruments. Finally, the electronic for the analysis of the signals and their acquisition is inside the yellow box.

In Section 4.1, we have already introduced the concept of explained the Zeeman laser and its stabilization unit here reported inside the green box. Then, in blue, the optical components of the laser scanning microscope. I used a pair of galvo mirrors as scanning unit (C2+, Nikon Instruments, JA) connected with its workstation and data acquisition electronics for image reconstruction. The scanned spot is relayed with a 60 mm scan lens and a 200 mm tube lens to fill the back aperture of the excitation objective (20X/0.5NA, DIC-M Plan Fluor, Nikon Instruments, JA). Then, the light travels through the sample, and its transmitted components are collected by another objective (4X/0.13NA, CFI Plan Fluor, Nikon Instruments, JA). Finally, a Wollaston Prism (WP10, Thorlabs, US) acts as a PSA and it has been used to analyze the polarization alteration induced by its interaction with the sample. The resulting intensities at the two outputs of the PSA are recorded by means of two photodiodes (PDA36A-EC, Thorlabs, US). A further lens has been used as a tube lens to focus the scanned area into the photodetector area in this non-descanned configuration. A calibration procedure has been applied to remove the offset of the dark current noise and equalize the response of the two photodiodes. Here I recall the Eq.12 in Ch. 3 that is expressing the photocurrents associated with the light detected by the two photodiodes after the Wollaston prism.

$$I_{OUT}^{k}(t) = m_{00} \pm m_{10} + (m_{01} \pm m_{11})\cos(\omega_z t) + (m_{02} \pm m_{12})\sin(\omega_z t)$$

Where $k = H, V$ depending upon the signal associated with one of the two photodiodes aligned on the respective output channel of the PSA. These channels correspond to the measurement of intensity of the amount of H or V polarized light respectively. In this compact notation, the sign

of in the linear combinations of Mueller coefficients is plus (+) when $k = H$, whereas it is minus (-) when $k = V$. It can be noticed that a subset of Mueller elements (m_{00}, m_{10}) only affects the amplitude of the DC component for both the photodiodes. Similarly, also the amplitude of the cosine and sine components are influenced by specific Mueller elements, namely $m_{01}, m_{11}, m_{02}, m_{12}$. A coaxial cable from each photodiode splits the photocurrent signal into two parts. As shown in the orange box of Fig. 30, the signals coming from the two photodiodes are split into two parts. One portion is averaged through the integration time of the data acquisition system of the Nikon C2 workstation, whereas the other is processed by a commercial lock-in amplifier (LA, HF2LI, Zurich Instruments, CH). The extraction of the coefficients associated with the DC can simply done by averaging the oscillating signal, so that:

$$DC_k = \langle I_{OUT}^k(t) \rangle = \int I_{OUT}^k(t)\, dt = m_{00} \pm m_{10}$$

Therefore, these two components (DC_H, DC_V) are used as quantities to generate two images. In one case the grey scale level is the sum of these two Mueller coefficients (m_{01}), whereas in the other it is the difference (m_{01}). Once these images are acquired, the identification of the isolated contribution of the Mueller elements can be simply performed by combining the sum/difference relation. The other portions of the photocurrent signals are sent to a LA. The demodulation also needs a reference external signal oscillating at the same frequency to perform the homodyne detection. I used a portion of the frequency counter signal coming from the stabilization unit of the Zeeman laser to feed the external trigger port of the LA [2]. The amplitude of the harmonic part has been extracted through the lock-in detection realized by the LA. The lock-in detection scheme isolates the spectral contents of the detected signals that are resonating with the reference. Moreover, it extracts the value of their in-phase (X) and in-quadrature (Y) components:

$$X_k = \langle I_{OUT}^k(t), cos(\omega_z t) \rangle = \int I_{OUT}^k(t) \cdot cos(\omega_z t + \phi)\, dt =$$

$$= \frac{1}{2}(m_{01} \pm m_{11})\, cos(\phi) + \frac{1}{2}(m_{02} \pm m_{12})\, sin(\phi)$$

$$Y_k = \langle I_{OUT}^k(t), sin(\omega_z t) \rangle = \int I_{OUT}^k(t) \cdot sin(\omega_z t + \phi)\, dt =$$

$$\frac{1}{2}(m_{02} \pm m_{12})\, cos(\phi) - \frac{1}{2}(m_{01} \pm m_{11})\, sin(\phi)$$

The reference signal can be represented as a pure cosine and its π/2-shifted replica to perform the lock-in demodulation after its phase with the respect to the measured signals has been properly calibrated. I carried out the calibration of the phase (ϕ) between the measured and the reference signals, by setting the reference signal with the same phase of the measured signal in a known condition. We can assume that in absence of any sample, the air through which the laser light is travelling is a purely isotropic and non-attenuating medium. The Mueller matrix of such medium is the unitary diagonal matrix. In this case, the expression of the photocurrent signal from a certain photodiode (e.g., $I_{OUT}^{\mathrm{H}}(t)$) can be just represented by the sum of the DC and

the cosine component, since the off-diagonal term are null. Only the cosine component survives since its amplitude term depends by an element (m_{11}) of the main diagonal of the Mueller matrix.

$$I_{OUT}^{k}(t)\big|_{air} = m_{00} \pm m_{11}\, cos(\omega_z t)$$

Once the cable length is considered, the signals are aligned by setting to zero the phase shift between the reference and the measured photocurrents. On the other hand, the measured signal coming from the other photodiode is in anti-phase with respect to both the reference and the H-detector. This can be clearly seen by looking at the minus sign in the amplitude of the cosine part in the analytical expression of $I_{OUT}^{V}(t)$. To recap, after the calibration the phase shifts must be $\phi = \phi_{ref-H} = 0°$ and $\phi_{ref-V} = 180°$. This can be done by measuring the phase shift between these signals in no-sample condition and set the measured phase as a phase shift in the respective channel. The phase demodulation feature of the LA can be used for this purpose and once the phase values have been measured, they can be applied to the detected channels as shifts. After the phase calibration, the Mueller coefficients can be readily linked to the DC/AC parts of the detected signals since we have:

$$DC|_{cal} = \pm m_{00} \qquad X_k|_{cal} = \tfrac{1}{2}(m_{01} \pm m_{11}) \qquad Y_k|_{cal} = \tfrac{1}{2}(m_{02} \pm m_{12})$$

The presence of the sample can be modeled with the comparison of the non-null phase shift term, and it influences the values of the cosine and sine components of the photocurrents. Therefore, the demodulation provides the linear combination of its Mueller coefficients. The resulting images are generated by using the in-phase (X) or in-quadrature (Y) level of the measured signals as greyscale value. The table below provides a quick picture to link the Mueller coefficients and the related linear combination of demodulated components.

m_{ij}	$j = 0$	$j = 1$	$j = 2$
$i = 0$	$DC_H + DC_V$	$X_H + X_V$	$Y_H + Y_V$
$i = 1$	$DC_H - DC_V$	$X_H - X_V$	$Y_H - Y_V$

Table 4 – Recap of the relations between the components of the measured photocurrent signals and the six Mueller coefficients identified with the method implemented in this imaging setup.

The values of the individual Mueller coefficient are determined by properly summing the results of each demodulation for both the photodiodes [3]. Therefore, each image is associated with a map of the value of a specific Mueller coefficient across the field of view on the sample plane. These coefficients are normalized with respect to the value of the coefficient m_{00}, representing the total transmitted intensity, therefore their value ranges from -1 to +1. As explained in Ch.4.2 and 4.3, the DFDP illumination allows to identify six Mueller coefficients through two simultaneous measurements with a single Wollaston prism as PSA. However, this optical setup is able to realize only four over six Mueller images because of the hardware limitation of the data acquisition electronics. Indeed, the Nikon C2 controller is provided with only four channels, each one is accessible through a male BNC connector. On the other side, the information carried by the detected signals is contained in three main quantities for each signal, namely the DC component and the in-phase/in-quadrature AC parts. While performing an imaging acquisition,

I had to discard one pair of these components (the in-quadrature part from both the photodiodes) at the expense of the identification of two more Mueller elements. This problem could be overcome by realizing a detection module with custom data acquisition electronics, but this task was beyond the scope of my project.

5.2 - Mueller imaging results

The analysis protocol is similar to that adopted for the single-point characterizations presented in Ch. 4. In this section, I refer to dark image as that acquired by blocking the light from the laser, that is used to subtract the noise offset. Then, for each sample I acquire an image without any sample ("air" image) and an image of the actual specimen ("sample" image). The dark images have been used to subtract the contribution of the environmental light and detector noise to the other images. Once this offset has been removed, I had to find a calibration coefficient that allows to equalize and compare the amplitude response from both the photodiodes.

As a first step, I acquired *dark* and air *images* to obtain the images of a non-attenuating and isotropic sample (such as the air) that is associated with an identity Mueller matrix. Therefore, among the six coefficients I was able to identify with this setup and method, the images associated with the diagonal elements have to be completely bright (m_{ii} = 1), whereas those related to the off-diagonal coefficients must be completely dark images (m_{ij}= 0). This apparently trivial results were achieved by applying the calibration protocol which is imposing the ideal response of the air. The balancing of the photodiode and the normalization of the DC and AC components are used to identify the calibration coefficients that leads to obtaining ideal images of an identity matrix.

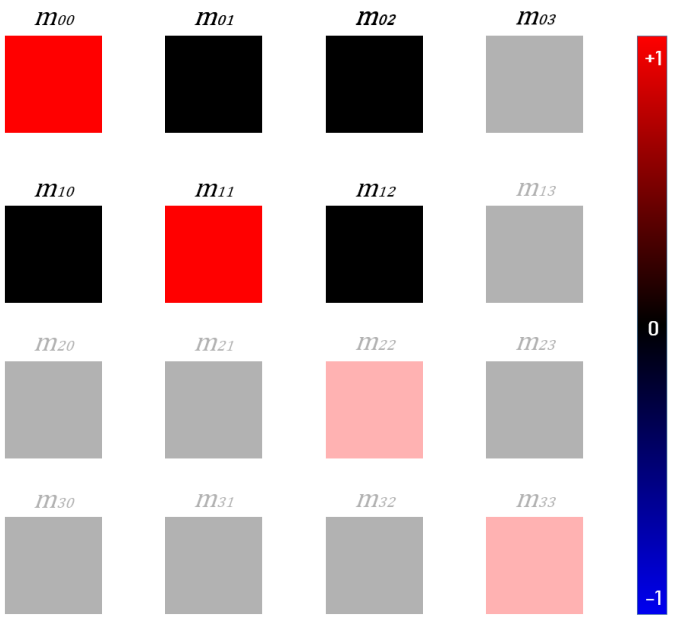

Figure 31- Theoretical results of an "air" sample that is associated with an identity Mueller matrix. These values has been imposed in the calibration of the amplitudes to balance the response of the photodiodes. The faded elements are those can't be identified with this setup, as it has been anticipated in Ch.4

Then, as a validation step, I repeated the single-point characterizations performed on polarization optics already shown in Ch.4. To quickly recall them, I recorded the images while rotating some reference polarization optics, that are a linear polarizer (VIS 700 BC4 CW02 ColorPol, CODIXX AG, DE) and a half waveplate (AHWP10M-600, Thorlabs, United States). Then, I calculated the Mueller coefficients for each angular position with a step of 10°. The main difference among these two validation experiments is that here I measured the sample response in different spatial position because of the scanning imaging configuration of this setup However, these reference sample are as much as spatially uniform as possible therefore the results were not expected to be structured in space. Therefore, the values of each Mueller coefficient have been calculated by averaging the whole "flat" images associated to the DC or AC part.

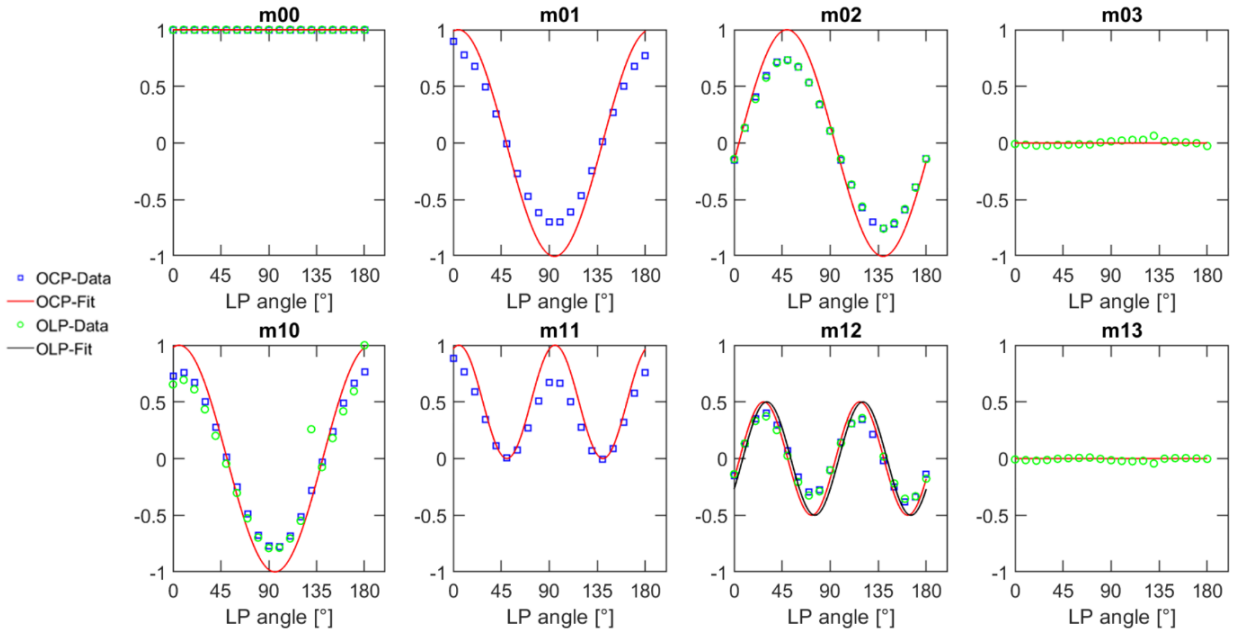

Figure 32 - Characterization of a Linear Polarizer. The eight Mueller coefficients have been identified by merging the two pairs of measurements with the OCP and OLP illumination.

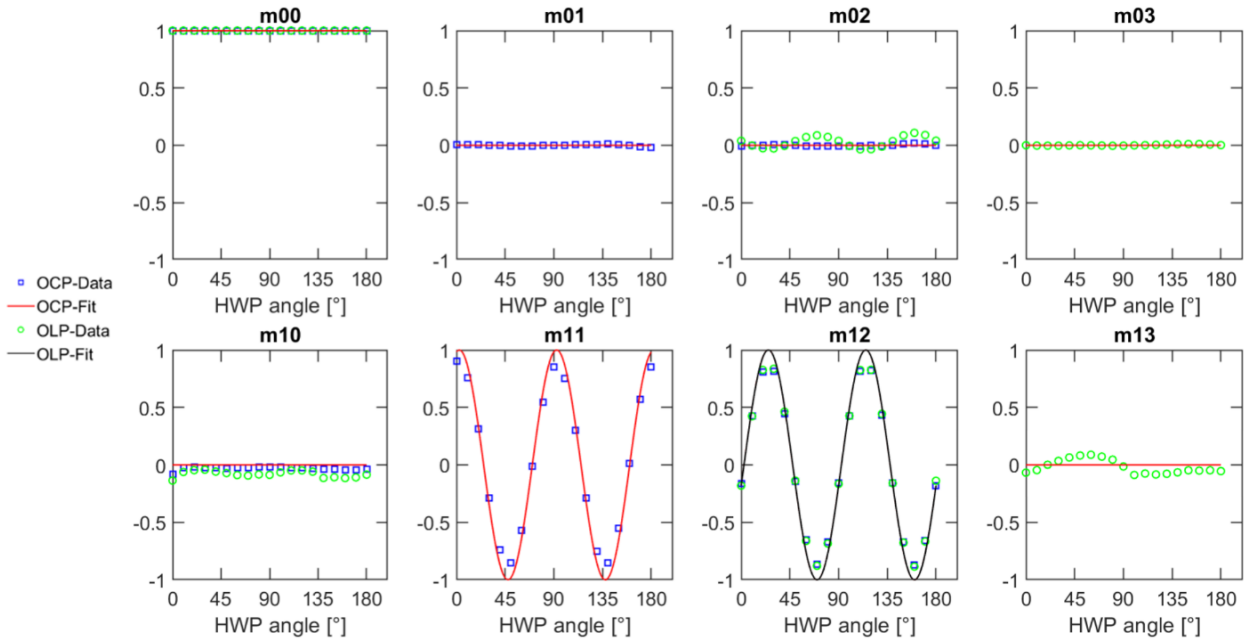

Figure 33 - Characterization of a Half Wave Plate. The eight Mueller coefficients have been identified by merging the two pairs of measurements with the OCP and OLP illuminations.

Finally, two different types of biological specimens well known for their anisotropic response have been imaged, namely starch granules and starch.

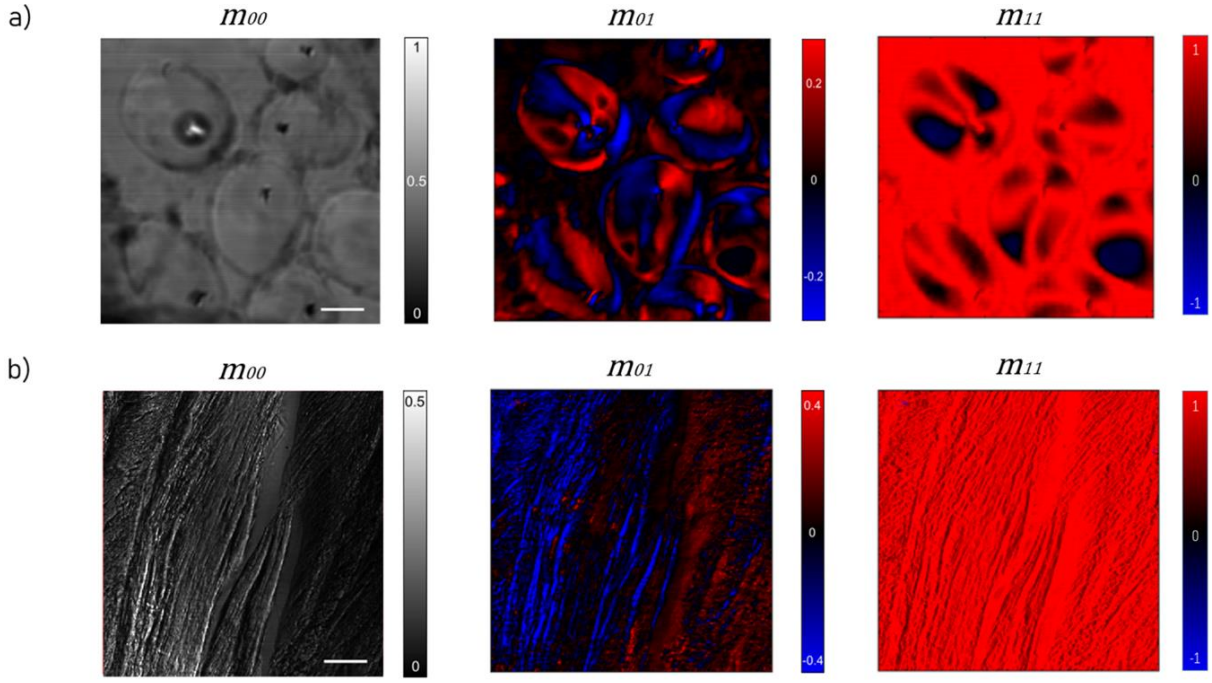

Figure 34 – Mueller images of potato starch grain a) and collagen fibers b). Scale bar size: 10 µm a) and 50 µm b). The grey scale colormap has been used to show the transmitted light (m_{00}) images. The same sample is also represented by using the other Mueller coefficients as intensity value of the pixels. The m_{01} image is associated to the linear dichroism of the sample, whereas m_{11} highlights the depolarized regions.

The first sample is made by starch granules from potato starch. Starch is a biomolecule with the function of energy storage in plants. It is made by a long chain of polymeric carbohydrates packed in semi polycrystalline granules. The organization and the orientation of the chain in the inner structure of the starch is such that it possesses regions with different birefringence [4]. Polarization-based microscopy can reveal the distribution of such zones because of its sensitivity to specimens possessing optical anisotropies. Similarly, a specimen made with collagen fibers embedded in the knee ligament of a rat provides a good case study, since the alignment and the compactness of the collagen fibers are sensitive to light polarization. Collagen is a protein complex acting as a structural network in biological tissues. Its fibers exhibit optical birefringence so their orientation can be studied with polarized light [5].

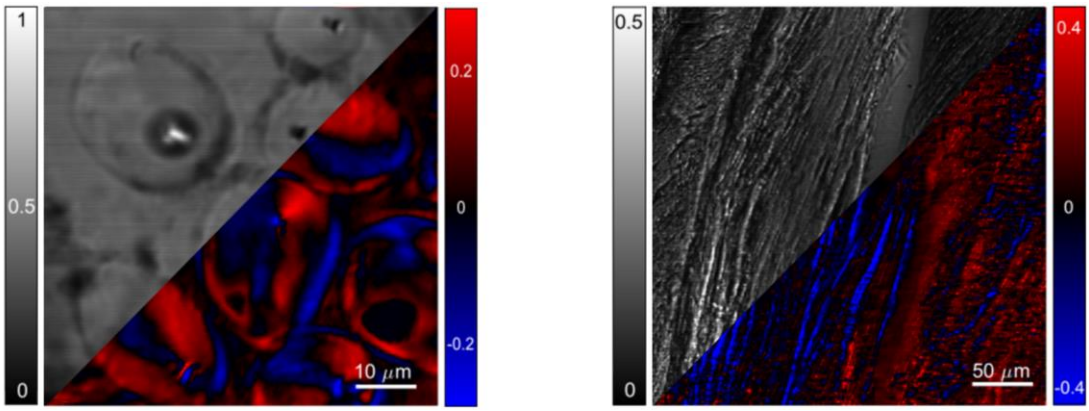

Figure 35 – Detail of Fig. 34 with the direct comparison between the transmitted light image (m_{00}) and that associated with the linear dichroism of the samples (m_{01}).

5.3 – Conclusion

The DFDP laser sources can be effectively adopted to perform polarization-based imaging in a laser scanning architecture. The feature of their optical emission allows to encode and decode the polarimetric fingerprint of semitransparent samples at a fast rate. The frequency shift between the longitudinal modes of the Zeeman laser I developed is around 700 kHz. Therefore, a minimum measurement time of 1/700 kHz = 1.4 μs allows to effectively reconstruct the sample anisotropies by analyzing the interferometric signal. The beating frequency is related to the frequency shift between the optical components contained in their laser emission. It could be further increased by increasing the magnetic flux within the laser cavity [6]–[8] or by means of different laser technologies with similar optical features [9], [10]. A faster polarimetric measurement allows the reduction of the imaging time that is a crucial issue in laser-scanning microscopes. A further advantage of this method is that the role of the Polarization State Generator is addressed to that of the illumination source. This approach avoids the need of a specific stage to manipulate the polarization state on the generation side. Therefore, there is no need to power supply, synchronize and align any other active optoelectronic device for this scope and the architecture of the instrument results simplified.

References

[1] A. Le Gratiet, A. Mohebi, F. Callegari, P. Bianchini, and A. Diaspro, "Review on complete mueller matrix optical scanning microscopy imaging," *Appl. Sci.*, vol. 11, no. 4, pp. 1–18, 2021, doi: 10.3390/app11041632.

[2] Z. Instruments, "Principles of lock-in detection and the state of the art Zurich Instruments," no. November, pp. 1–10, 2016.

[3] F. Callegari, A. Le Gratiet, A. Zunino, A. Mohebi, P. Bianchini, and A. Diaspro, "Polarization Label-Free Microscopy Imaging of Biological Samples by Exploiting the Zeeman Laser Emission," *Front. Phys.*, vol. 9, no. October, pp. 1–8, 2021, doi: 10.3389/fphy.2021.758880.

[4] H. F. Zobel, "Molecules to Granules: A Comprehensive Starch Review," *Starch - Stärke*, vol. 40, no. 2, pp. 44–50, 1988, doi: 10.1002/star.19880400203.

[5] P. Whittaker and P. B. Canham, "Demonstration of Quantitative Fabric Analysis of Tendon Collagen using Two-Dimensional Polarized Light Microscopy," *Matrix*, vol. 11, no. 1, pp. 56–62, 1991, doi: 10.1016/S0934-8832(11)80227-1.

[6] H. Statz, R. Paananen, and G. F. Koster, "Zeeman Effect in Gaseous Helium-Neon Optical Maser," *J. Appl. Phys.*, vol. 33, no. 7, pp. 2319–2321, 1962, doi: 10.1063/1.1728954.

[7] H. Takasaki, N. Umeda, and M. Tsukiji, "Stabilized transverse Zeeman laser as a new light source for optical measurement," *Appl. Opt.*, vol. 19, no. 3, p. 435, 1980, doi: 10.1364/ao.19.000435.

[8] T. Shigeoka, S. Imanishi, and S. Kawata, "Development of a beat frequency tunable stabilized axial Zeeman laser," *Japanese J. Appl. Physics, Part 1 Regul. Pap. Short Notes Rev. Pap.*, vol. 36, no. 5 A, pp. 2681–2684, 1997, doi: 10.1143/jjap.36.2681.

[9] G. W. Baxter, J. M. Dawes, P. Dekker, and D. S. Knowles, "Dual-Polarization Frequency-Modulated L,aser Source," vol. 8, no. 8, pp. 1015–1017, 1996.

[10] S. Zhang, Y. Tan, and Y. Li, "Orthogonally polarized dual frequency lasers and applications in self-sensing metrology," *Meas. Sci. Technol.*, vol. 21, no. 5, 2010, doi: 10.1088/0957-0233/21/5/054016.

6 – Conclusions

The development of optical imaging methods has been often driven by the technological advancements of light sources. There is a wide variety of laser sources available in the market that have been applied to many traditional microscopy applications. The specific structuring of light, based on the engineered alteration of its properties, may enable new and more sophisticated imaging schemes. In this thesis work, I reviewed the main innovations in the development of laser sources that may have a significant impact in microscopy. Some of these sources have been tailor-designed for specific applications. The use of such custom illumination stages helps in reducing the complexity of the optical setup as well as in optimizing the performance of the target technique.

With this spirit, I worked on two different type of laser sources which could help the spreading of polarization-based label-free microscopy. One of the key advantages of such an approach is the merging of the illumination stage with the Polarization Stage Generator (PSG) to dynamically generate states of polarized light.

One of the devices is a dual-frequency, dual polarization (DFDP) laser based on the Zeeman effect. Such a source enables high-speed generation and measurement of the polarization states of light (Ch.3). This feature makes this type of laser the ideal candidate for the realization of polarization-resolved imaging in a laser scanning microscope (Ch.5). Here, the speed of the beating signals encoding the polarization response of the sample can cope with the time constraint introduced by the short pixel dwell time required for a fast acquisition. This approach can be further extended by developing DFDP sources able to generate even faster beating signals and covering different spectral regions. In particular, this may facilitate the coupling of this class of label free methods with the ones based on fluorescence, since they require to match the excitation lines with the absorption band of the fluorescent tags.

Also, I developed a similar approach using a dual-comb laser (DCL) as illumination stage and PSG (Ch.4). Conversely to most of the traditional DCL sources, this device has been based on a single-cavity architecture. Therefore, the realization cost and complexity of this laser is reduced, helping to spread the use of this source in new fields. I used it to realize an interferometric method which allows the broadband identification of the polarimetric response of sample within the whole output bandwidth of the laser. This feature can be effectively exploited in several spectroscopic applications with the goal of studying optical anisotropies of the specimens. In imaging, these sources can be exploited to perform hyperspectral imaging based on the analysis of the self-mixing interferograms generated by the detection of the two combs. Moreover, the DCL emission is also associated with temporal properties such as the ultrashort pulsewidth and the sweeping delay between the two trains of pulses. These features can be effectively exploited to implement different nonlinear sensing and imaging techniques such as Second Harmonic Generation, Two-Photon Fluorescence and Pump-Probe imaging.

The characteristic advantage in using such sources lies in the features of its optical emission. They allow the implementation of several sensing schemes minimizing the needs for external components, such as delay-lines or intensity modulators. In conclusion, I believe that the

development of tailored laser sources may amplify the impact of established imaging techniques, as well as to enable new optical schemes. The generation of light carrying a rich information content extends the possibilities of developing new sensing principles and technologies. The technological advancement of the laser source will be always driven by the requirements of the photonics application. At the same time, the development of even newer optical instruments may be enabled by improving of the generation of tailored states of light.

Annexes

A. Mathematical formalisms for polarization description

Polarization describes the vectorial properties of an electromagnetic (EM) field in terms of the direction of its oscillation in the 3-dimensional space. As a convention, this term usually describes the vibration direction of the electric field component of the EM wave. The Jones and the Stokes-Mueller formalisms are the two main physical frameworks used to describe the state of polarized light and their interaction with a medium. In this annex, the basis of these two formalisms is provided and some application cases are addressed.

A.1 Jones formalism

The Jones formalism deals with the vectorial description of the complex electric field components. A Jones vector made by 2x1 complex elements is used to describe the state of polarization of an EM field. Considering an EM monochromatic plane wave oscillating at the optical frequency ω and propagating along $\hat{z}$, its evolution in time and space is described by the following relation.

$$\vec{E}(x,y,z,t) = \vec{E}_x(x,y,z,t) + \vec{E}_y(x,y,z,t) = A_x e^{-i(\omega t - kz - \delta_x)}\hat{x} + A_y e^{-i(\omega t - kz - \delta_y)}\hat{y}$$

Where $\hat{x}, \hat{y}$ are the unitary vectors directed defining the $x-y$ plane orthogonal to the propagation direction z. The overall field is composed of two parts oscillating in two orthogonal directions. The relation between the amplitudes (A_x, A_y) and the phases (δ_x, δ_y) of these two components defines the kind of polarization state. Its Jones vector efficiently describes the polarization state associated with such wave in a different representation.

$$\vec{V} = e^{-i(\omega t - kz)}\begin{bmatrix} A_x e^{i\delta_x} \\ A_y e^{i\delta_y} \end{bmatrix} = e^{-i(\omega t - kz - \delta_x)}\begin{bmatrix} A_x \\ A_y e^{i\delta} \end{bmatrix}$$

Where δ is their phase difference. The relative values of these two pairs of quantities define the overall polarization states. The complete evolution in time of the two components describes an ellipse in the plane orthogonal to the propagation direction, namely the $x-y$ plane. Therefore, the most generic state of polarized light is termed *elliptical polarization* state. The amplitude and phase differences determine the ratio between the ellipse axes and their orientation. In degenerated cases, if the amplitudes of the two components are equal and their phase shift is null, the light is defined as *linearly polarized*, whereas if their phase difference is $\pi/2$, the field is *circularly polarized*.

Any pair of orthogonal Jones vectors is a basis of the overall EM field, so it can describe any state of polarized light. The vectors composing the most common bases, namely horizontal-vertical, diagonal-antidiagonal and right-left (*H-V, D-A,* and *R-L*) are reported below.

$\vec{V}_H$	$\vec{V}_V$	$\vec{V}_D$	$\vec{V}_A$	$\vec{V}_R$	$\vec{V}_L$
$\begin{bmatrix}1\\0\end{bmatrix}$	$\begin{bmatrix}0\\1\end{bmatrix}$	$\frac{1}{\sqrt{2}}\begin{bmatrix}1\\1\end{bmatrix}$	$\frac{1}{\sqrt{2}}\begin{bmatrix}1\\-1\end{bmatrix}$	$\frac{1}{\sqrt{2}}\begin{bmatrix}1\\i\end{bmatrix}$	$\frac{1}{\sqrt{2}}\begin{bmatrix}1\\-i\end{bmatrix}$
↕	↔	⤢	⤡	↻	↻

On the other hand, the response of a medium upon excitation with polarized light is modeled through a 2x2 matrix with complex elements. Below I report some common examples of polarizing optical elements described through the Jones formalism.

$$[J^H_{LP}] = \begin{bmatrix} 1 & 0 \\ 0 & 0 \end{bmatrix} \qquad [J^D_{LP}] = \frac{1}{2}\begin{bmatrix} 1 & 1 \\ 1 & 1 \end{bmatrix} \qquad [J^R_{CP}] = \frac{1}{2}\begin{bmatrix} 1 & -i \\ i & 1 \end{bmatrix} \qquad [J^H_{HWP}] = e^{i\pi/2}\begin{bmatrix} 1 & 0 \\ 0 & -1 \end{bmatrix}$$

$$[J^V_{LP}] = \begin{bmatrix} 1 & 0 \\ 0 & 1 \end{bmatrix} \qquad [J^A_{LP}] = \frac{1}{2}\begin{bmatrix} 1 & -1 \\ -1 & 1 \end{bmatrix} \qquad [J^L_{CP}] = \frac{1}{2}\begin{bmatrix} 1 & i \\ -i & 1 \end{bmatrix} \qquad [J^H_{QWP}] = e^{i\pi/4}\begin{bmatrix} 1 & 0 \\ 0 & -1 \end{bmatrix}$$

A polarizer (linear, LP or circular, CP) is an object exhibiting strong dichroism, that is the selective ability to attenuate a specific polarization component while the other remains unaltered upon transmission or reflection. Similarly, a phase retarder (HWP, QWP) selectively introduces a phase shift that depends upon the relative orientation of its optical axis and the polarization components of the EM field. Such matrices describe the polarimetric response of the optical elements with a certain orientation. When these optics are rotated along their azimuthal angle, their response can be adapted by applying the proper rotation matrix to the original Jones matrix if the rotation angle is known. Similar reasoning can be done for the vector describing light polarization. The rotation matrix is defined as follows.

$$[R] = \begin{bmatrix} \cos(2\theta) & \sin(2\theta) \\ -\sin(2\theta) & \cos(2\theta) \end{bmatrix}$$

And its effect on the rotation of the optical elements or on the polarization of a light beam is defined by these two relations.

$$[J(\theta)] = [R(-\theta)] \cdot [J] \cdot [R(\theta)] \qquad V(\theta) = [R(\theta)] \cdot \vec{V}$$

A.2 Stokes-Mueller formalism

The Stokes-Mueller formalism deals directly with the intensity of polarization components of light. Therefore, both the elements of the Stokes vector, used to describe the light polarization, and those of the Mueller matrix, used to model the medium response, are represented by real value coefficients. The elements of a generic Stokes vector express the intensity difference between orthogonally polarized components, as shown in the following definition.

$$\vec{S} = \begin{bmatrix} S_1 \\ S_2 \\ S_3 \\ S_4 \end{bmatrix} = \begin{bmatrix} E_x^* E_x + E_y^* E_y \\ E_x^* E_x - E_y^* E_y \\ 2Re(E_x^* E_y) \\ 2Im(E_x^* E_y) \end{bmatrix} = \begin{bmatrix} |A_x|^2 + |A_y|^2 \\ |A_x|^2 - |A_y|^2 \\ 2A_x A_y cos\delta \\ 2A_x A_y sin\delta \end{bmatrix} = \begin{bmatrix} I_0 \\ I_H - I_V \\ I_D - I_A \\ I_R - I_L \end{bmatrix}$$

Where I_0 is the total intensity of the light and I_j is the intensity of the j^{th} polarization component (with $j = H, V, D, A, R, L$). Below I report the Stokes vector for the most common states of fully polarized light.

$$\vec{S}_{H-V} = \begin{bmatrix} 1 \\ \pm 1 \\ 0 \\ 0 \end{bmatrix} \qquad \vec{S}_{D-A} = \begin{bmatrix} 1 \\ 0 \\ \pm 1 \\ 0 \end{bmatrix} \qquad \vec{S}_{R-L} = \begin{bmatrix} 1 \\ 0 \\ 0 \\ \pm 1 \end{bmatrix}$$

Conversely to the Jones formalism, the Stokes vectors also allow the representation of partially polarized light. The polarization description is done by splitting the fully polarized and the unpolarized components as the sum of two vectors, as reported in the following relation.

$$\vec{S} = \overrightarrow{S_p} + \overrightarrow{S_u} = \gamma \begin{bmatrix} S_1 \\ S_2 \\ S_3 \\ S_4 \end{bmatrix} + (1-\gamma) \begin{bmatrix} 1 \\ 0 \\ 0 \\ 0 \end{bmatrix}$$

Here γ is the degree of polarization of the light and it is defined as $\gamma = \sqrt{S_2 + S_3 + S_4}/S_1$, whereas the coefficient $(1-\gamma)$ represents the amount of unpolarized light. For a generic Stokes vector, its elements are bounded by the inequality $S_1 \geq S_2 + S_3 + S_4$ where the two sides are equal in the case of completely polarized light ($\gamma = 1$).

Finally, the Mueller matrix of an object interacting with a beam of polarized light has sixteen real-valued coefficients expressing its anisotropy properties, such as dichroism and birefringence.

m_{ij}	*1*	*2*	*3*	*4*
1	$\frac{I_0}{I_0}$	$\frac{I_H - I_V}{I_H + I_V}$	$\frac{I_D - I_A}{I_D + I_A}$	$\frac{I_R - I_L}{I_R + I_L}$
2	$\frac{I^H - I^V}{I^H + I^V}$	$\frac{I_H^H - I_H^V - (I_V^H - I_V^V)}{I_H^H + I_H^V + I_V^H + I_V^V}$	$\frac{I_D^H - I_D^V - (I_A^H - I_A^V)}{I_D^H + I_D^V + I_A^H + I_A^V}$	$\frac{I_R^H - I_R^V - (I_L^H - I_L^V)}{I_R^H + I_L^V + I_R^H + I_L^V}$
3	$\frac{I^D - I^A}{I^D + I^A}$	$\frac{I_H^D - I_H^A - (I_V^D - I_V^A)}{I_H^D + I_H^A + I_V^D + I_V^A}$	$\frac{I_D^D - I_D^A - (I_A^D - I_A^A)}{I_D^D + I_D^A + I_A^D + I_A^A}$	$\frac{I_R^D - I_R^A - (I_L^D - I_L^A)}{I_R^D + I_L^A + I_R^D + I_L^A}$
4	$\frac{I^R - I^L}{I^L + I^L}$	$\frac{I_H^R - I_H^L - (I_V^R - I_V^L)}{I_H^R + I_H^L + I_V^R + I_V^L}$	$\frac{I_D^R - I_D^L - (I_A^R - I_A^L)}{I_D^R + I_D^L + I_A^R + I_A^L}$	$\frac{I_R^R - I_R^L - (I_L^R - I_L^L)}{I_R^R + I_L^L + I_R^R + I_L^L}$

Table 5 - Definition of a Mueller matrix as function of the intensity of polarization state of the incident light (indicated with the subscript) and of the intensity of the polarization component along the analysis basis (indicated with the superscript). The i,j indices are indicated the matrix rows and columns respectively.

The following Mueller matrices are associated with some of the most common polarizing optical elements, such as those used to validate the experimental technique presented in Chapter 4.

$$[M_{LP}^{H-V}] = \frac{1}{2}\begin{bmatrix} 1 & \pm 1 & 0 & 0 \\ \pm 1 & 1 & 0 & 0 \\ 0 & 0 & 0 & 0 \\ 0 & 0 & 0 & 0 \end{bmatrix}; \qquad [M_{LP}^{D-A}] = \frac{1}{2}\begin{bmatrix} 1 & 0 & \pm 1 & 0 \\ 0 & 0 & 0 & 0 \\ \pm 1 & 0 & 1 & 0 \\ 0 & 0 & 0 & 0 \end{bmatrix}; \qquad [M_{LP}^{R-L}] = \frac{1}{2}\begin{bmatrix} 1 & 0 & 0 & \pm 1 \\ 0 & 0 & 0 & 0 \\ 0 & 0 & 0 & 0 \\ \pm 1 & 0 & 0 & 1 \end{bmatrix}$$

$$[M_{HWP}] = \begin{bmatrix} 1 & 0 & 0 & 0 \\ 0 & 1 & 0 & 0 \\ 0 & 0 & -1 & 0 \\ 0 & 0 & 0 & -1 \end{bmatrix}; \qquad [M_{QWP}] = \begin{bmatrix} 1 & 0 & 0 & 0 \\ 0 & 1 & 0 & 0 \\ 0 & 0 & 0 & 1 \\ 0 & 0 & -1 & 0 \end{bmatrix};$$

The rotation matrix for the Stokes-Mueller formalism is:

$$[R] = \begin{bmatrix} 1 & 0 & 0 & 0 \\ 0 & \cos(2\theta) & \sin(2\theta) & 0 \\ 0 & -\sin(2\theta) & cos(2\theta) & 0 \\ 0 & 0 & 0 & 1 \end{bmatrix}$$

and its effect on the rotation of the azimuthal angle of the optical elements or on the polarization of a light beam is described as follows.

$$[M(\theta)] = [R(-\theta)] \cdot [M] \cdot [R(\theta)] \qquad \vec{S}(\theta) = [R(\theta)] \cdot \vec{S}$$

These relations have been used to model the experiments presented in Section 3.3 and 4.3. Here, I report the extended results for the case of a linear polarizer and a half-wave plate that have been used as reference test samples. Their response has been probed by varying their azimuthal angle and the following theoretical relations have been used to compare the experimental data of Fig.12-13 and 27-29 in that Section.

$$[M_{LP}(\theta)] = \begin{bmatrix} 1 & cos(2\theta) & sin(2\theta) & 0 \\ cos(2\theta) & cos^2(2\theta) & sin(2\theta)cos(2\theta) & 0 \\ sin(2\theta) & -sin(2\theta) & sin^2(2\theta) & 0 \\ 0 & 0 & 0 & 0 \end{bmatrix}$$

$$[M_{HWP}(\theta)] = \begin{bmatrix} 1 & 0 & 0 & 0 \\ 0 & cos^2(2\theta) - sin^2(2\theta) & 2cos(2\theta)sin(2\theta) & 0 \\ 0 & 2cos(2\theta)sin(2\theta) & sin^2(2\theta) - cos^2(2\theta) & 0 \\ 0 & 0 & 0 & 1 \end{bmatrix}$$

B. Helium-Neon Laser and Zeeman Laser

B.1 HeNe Laser

The helium-neon (HeNe) laser is a gas laser that operates with a gas mixture of helium (He) and neon (Ne) enclosed within a discharge tube. Both helium and neon have specific energy levels associated with their atomic or molecular structures. The gas mixture is excited by an electrical discharge, typically through the application of a high voltage. This excitation causes electrons in the helium atoms to jump to higher energy levels. Some of these excited helium atoms collide with neon atoms, transferring energy to the neon atoms and raising them to higher energy levels as well. These processes combine to generate a coherent and monochromatic laser beam at a specific wavelength typically in the red or near-infrared region. The HeNe laser is known for producing single-frequency radiation, which means it emits light at a very specific and well-defined wavelength. An optical cavity may support multiple longitudinal modes, which correspond to different standing wave patterns formed within the cavity. These modes have slightly different frequencies, resulting in a frequency comb-like spectrum. In the HeNe laser, the population inversion and gain mechanism are relatively narrowband due to the structures of the energy levels involved in the optical transition. The narrow gain, combined with the resonance condition of the cavity, helps to suppress other competing modes and favors the oscillation of a single longitudinal mode (SLM). However, a HeNe laser designed to produce single-frequency radiation, may be susceptible to mode hopping, where the dominant longitudinal mode can switch abruptly to a neighboring mode. The mode with the highest gain will tend to dominate, leading to lasing in that mode. However, small changes in the gain or loss conditions within the laser medium can cause the dominance to shift to a different mode, resulting in mode hopping. Mode hops can be caused by environmental changes, such as temperature or mechanical disturbances that are affecting the optical path length experienced by the light travelling in the cavity. The position of the SLM is determined by the cavity length through the Free Spectral Range (FSR). Therefore, a small thermal expansion of the laser tubes shifts the order of oscillating mode to the next that is associated with a different polarization state. The separation between adjacent longitudinal modes, also known as mode spacing or FSR, can play a role in mode sweeping. Mode sweeping causes the laser emission to shift or sweep across different longitudinal modes of the laser cavity. It is typically characterized by a rapid variation of the laser output frequency or wavelength. Therefore, this mode sweeping causes the laser beam to be emitted with both switching frequency and polarization state, if there is not any polarizing element in the cavity. Different adjacent longitudinal modes oscillate in time and since their polarization is usually orthogonal, the overall polarization state result emitted randomly. If the power is monitored with a polarization filter, the perturbation of the cavity causing the mode hopping generates an oscillation in the output power that is related to the polarization switching. To stabilize the laser and maintain single-frequency operation, various techniques can be employed, including temperature control with active feedback.

B.2 Zeeman Laser

The application of an external magnetic field to the HeNe splits the energy levels involved in the optical transition. Thus, the gain curve is split and the device emits a beam made by two laser lines with different frequency and orthogonal polarization state. Therefore, a Zeeman laser generates two linear orthogonal or two circular orthogonal states of polarized light, depending on the magnetic field orientation with respect of the cavity axis. When the field is applied perpendicularly to the cavity axis, the crossed-polarized states are linear and this device is called Transverse-effect Zeeman Laser. Conversely, a Longitudinal or Axial Zeeman-effect Laser emits two orthogonal counter-rotating circularly polarized components by applying a magnetic field parallel to the optical axis.

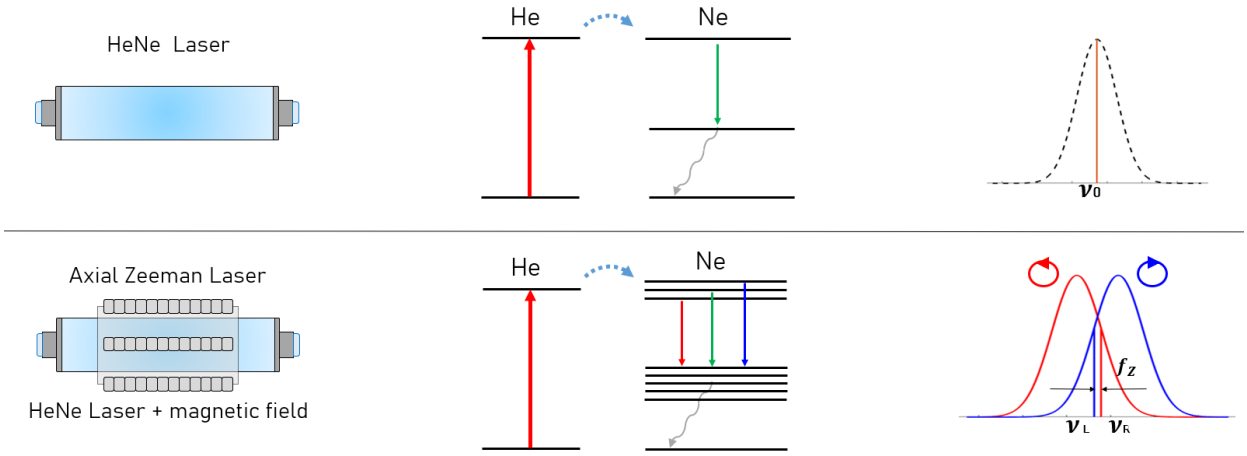

Figure 36 - Comparison between a normal HeNe laser and a Zeeman laser with respect to the structure of their energy levels and their optical emission

The thermal perturbations causing the variations of the cavity length are an issue of concern when using a Zeeman laser. The mode sweeping causes the unbalancing of the optical power associated with the two orthogonal laser modes. Moreover, it affects both their absolute and relative positions in the frequency axis, causing a variation of their frequency separation. Therefore, the beating signal generated by their interference cannot be modeled as a stable single frequency oscillation @ f_z because the oscillating term becomes unstable.

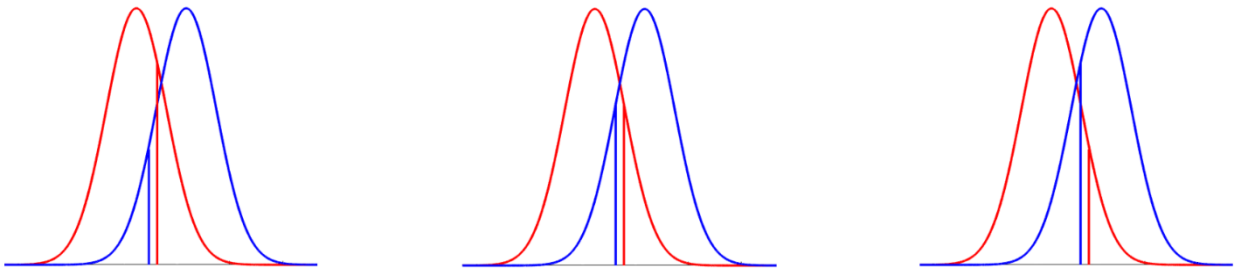

Figure 37 - Schematic representation of the frequency translation experienced by the optical lines of the Zeeman laser because of the mode sweeping. The central configuration is corresponding to the stabilized condition, whereas the two lateral spectra show the unbalanced condition that is when they experience different values of the optical gain in their respective gain curves.

C. Elements of ultrafast laser design

This section aims to quickly recall the fundamental concepts used in designing a laser oscillator. These topics have been widely treated in several graduated textbooks that have been mainly used as reference to write this annex. After the quick recall of each topic, I reported the design choices implemented in the actual case of the DCL oscillator developed during the collaboration with the ULP group.

C.1 Mode evolution in the laser resonator

The ABCD matrix formalism used to describe any optical system with a ray optics model can be adapted to describe the evolution of a gaussian beam. In geometric optics, a ray of light is modeled with two main parameters that are elements of a 2x1 vector (r_i). These elements are the position (r_1) and the angle (θ) of the ray direction with the respect to the propagation axis (z). Each optical element in the system is described with a 2x2 matrix that is modifying the values of r. Therefore, the ray (r_0) coming out from a generic optical element can be described by the following relation.

$$\begin{bmatrix} r_2 \\ \theta_2 \end{bmatrix} = \begin{bmatrix} A & B \\ C & D \end{bmatrix} \cdot \begin{bmatrix} r_1 \\ \theta_1 \end{bmatrix}$$

Laser light can be modeled as a gaussian beam that is a spherical wave under the paraxial approximation, therefore its radius of curvatures is defined by a complex quantity (q).

$$q(z) = \frac{1}{R(z)} - j \cdot \frac{\lambda}{\pi w(z)^2}$$

Where R is the radius of curvature of the associated spherical wave, and λ is the wavelength of the light and w is the waist size of the laser beam. These quantities are function of the position along the optical axis of the system. The same ABCD matrices can be used to model how the optical elements alter the values of q. When a laser beam travels through an optical element, the following relation holds true.

$$q_o = \frac{A \cdot q_i + B}{C \cdot q_i + D}$$

where A, B, C and D are still the parameters describing the optical element. When dealing with a linear optical system (os) made by several optical elements, the ABCD matrix of each optical element can be evaluated sequentially. Multiply the ray vector by the ABCD matrix of the first element ($[M_1]$), then by the ABCD matrix of the second element, and so on up to the n-th optical element ($[M_n]$). This process simulates the propagation of the laser beam through the whole optical system. Alternatively, the whole optical system can be described by the following matrix.

$$[M_{os}] = [M_n] \cdot [M_{n-1}] \cdot \ldots \cdot [M_1]$$

The evolution of a gaussian mode in a laser resonator can be described by using the same matrices reported above and considering the optical path of the light in the laser cavity. If we assume a Fabry-Perot resonator, the light travels twice through each optical element and the roundtrip matrix must be modelled accordingly.

$$[M_{RT}] = [M_1] \cdot \ldots \cdot [M_n] \cdot [M_n] \cdot \ldots \cdot [M_2]$$

where $[M_1]$ is the matrix describing the mirror acting as an output coupler of the cavity. The design of the resonator is an iterative process where the parameters of the optical elements are modified until specific values of the beam parameters are obtained. In addition, they can be used to determine the stability properties of the resonator. The mode size at the position where certain optical elements are placed is a crucial quantity. In general, it influences the local intensity of the beam, that should be taken into account to prevent optical damaging of the intracavity elements. The high intensity is often exploited to introduce the effect of nonlinear processes in a controlled way. Moreover, the mode size of sustained by the resonator plays a crucial role in determining the gain efficiency in the active medium and the spatial profile of the laser beam.

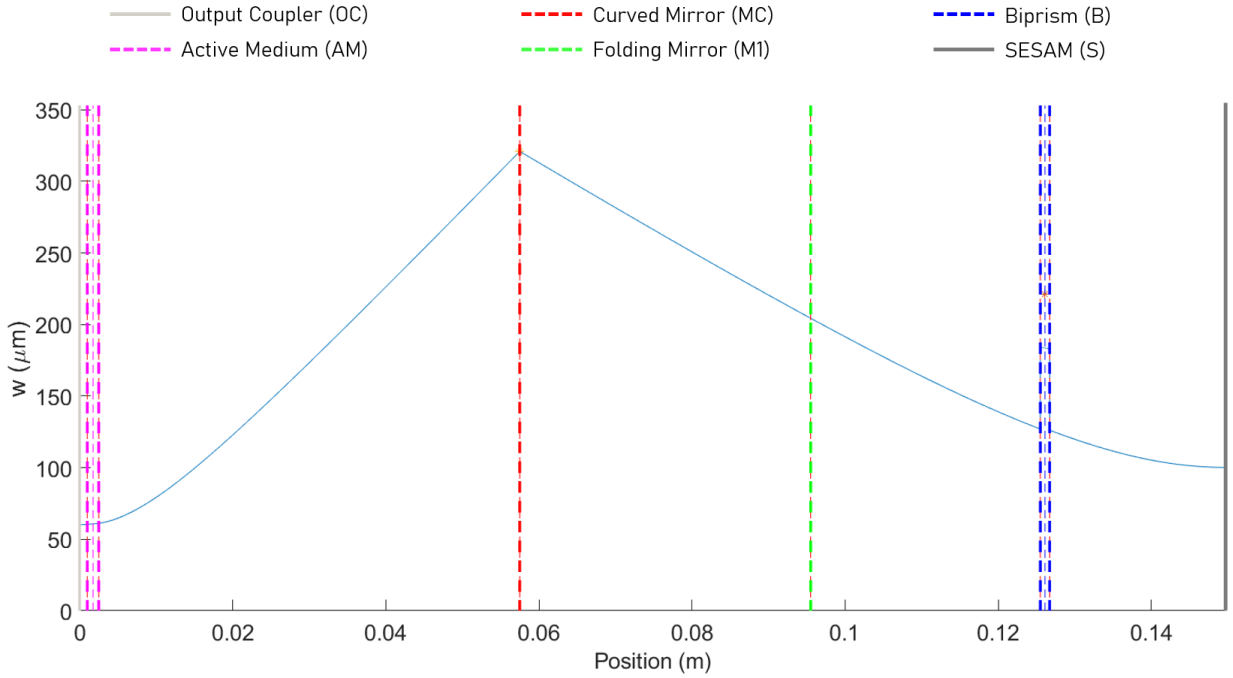

Figure 38 - Simulation of the mode evolution inside the cavity of the DCL oscillator presented in Ch. 5. The vertical lines represent the position of the optical elements indicated in the legend, whereas the curve indicates the variation of the mode radius (w) at different positions inside the resonator

The mode size (indicated as $A_{eff} = 2\pi w$, where w is the mode radius) in the active medium has a role in determining the threshold pump power and a more efficient laser operation since it is directly linked to the optical gain provided by its active medium. The relationship between these quantities impacts the laser efficiency and other quantities determining the performances of the resonator. For instance, the gain coefficient (g) of the active medium represents the rate of increase in the number of photons per unit length in the presence of stimulated emission. The optical gain (G) provided by the active medium is given by:

$$G = g \cdot L \cdot N \propto P_{pump}/A_{eff}$$

where L is the length of the gain medium and N is the number of population inversions (excited state atoms) per unit length. The gain coefficient (g) is related to the pump power (P_{pump}) and the effective cross-sectional area (A_{eff}) of the mode in the gain medium:

$$g = \sigma_L \cdot P_{pump}/A_{eff}$$

where σ_L is a spectroscopic parameter of the gain crystal called stimulated emission cross-section.

C.2 Dispersion compensation and generation of optical solitons

The mode size of the laser radiation inside a resonator is also closely linked to the generation of nonlinear effects in the intracavity elements. The relationship between mode size and nonlinear effects affects pulse duration, spectral broadening, and the balance between chromatic dispersion, self-phase modulation (SPM), and group delay dispersion (GDD). The SPM introduces an intensity-dependent value of the refractive index of the medium, leads to a change in the phase of different frequency components of the pulse. As different frequency components experience different phase shifts due to SPM, the pulse spectrum can broaden. Chromatic dispersion, SPM, and GDD are interconnected phenomena that influence the pulse characteristics. Chromatic dispersion describes how different frequencies of light propagate at different speeds, leading to pulse broadening or compression. SPM, on the other hand, changes the phase of different frequency components of the pulse. GDD represents the variation of group delay with frequency, contributing to the pulse dispersion. In an ultrafast laser resonator, the formation of a soliton light pulse involves the balancing of these quantities. The balance between these effects is crucial for achieving desired pulse duration and spectral properties. Chromatic dispersion can be compensated using suitable dispersive elements like prisms or chirped mirrors. We employed Gires-Tournois Interferometer (GTI) mirrors to introduce the wavelength-dependent phase shift thus balancing the broadening effect of the Self-Phase Modulation (SPM). The light intensity and mode size play a critical role in this balance. A larger mode size results in a higher light intensity, leading to stronger SPM effects and potential pulse shortening. However, it can also increase the challenge of managing dispersion and maintaining a compressed pulse. Proper optimization of mode size, dispersion compensation, and GDD control is necessary to achieve the desired pulse duration, spectral broadening, and overall pulse quality. SPM is a nonlinear optical effect that occurs in materials with a nonlinear response to the intensity of light. Such nonlinearity is described by n_2 that is the nonlinear refractive index associated with the Kerr effect. As the ultrafast pulse propagates through the laser resonator, the intensity (I) profile changes due to the Kerr effect, resulting in a change in the refractive index of the medium ($n(z)$).

$$n(I) = n + n_2 \cdot I$$

The amount of accumulated nonlinear phase due to the Kerr effect is evaluated by calculating the β-integral of the intracavity elements, whose definition is reported in the following equation.

$$\beta = \frac{2\pi}{\lambda}\int_0^{l_i} n_2 I(z)dz$$

where l_i is the length of the optical path inside of the ith optical element and $I(z)$ is the beam intensity. The main sources of these nonlinear phase shifts are the active medium and the intracavity biprism. The following reports the material parameters and the beam features used to evaluate the SPM contribution of these two elements.

	$w(\mu m)$	$L(mm)$	$n_2\ (10^{-20} \cdot m^2/W$
Yb:CALGO	60	1.5	9
Biprism	120	1	2.7

The amount of GDD compensating the effect of the SPM introduced by the intracavity elements is estimated through the following relation:

$$GDD \propto -\tau_P^2 \cdot \beta$$

where τ_P is the expected duration of the ultrashort pulse.

List of scientific contributions

Journal Publications

- C.R. Phillips, B. Willenberg, A. Nussbaum-Lapping, F. Callegari, S. L. Camenzind, J. Pupeikis, U. Keller - Coherently averaged dual-comb spectroscopy with a low-noise and high-power free-running gigahertz dual-comb laser - Optics Express (2023)
- A. Mohebi, A. Le Gratiet, A. Trianni, F. Callegari, P. Bianchini, A. Diaspro - Phasor map analysis to investigate Hutchinson– Gilford progeria cell under polarization-resolved optical scanning microscopy - Scientific Reports, 2022
- F. Callegari, A. Le Gratiet, A. Zunino, A. Mohebi, P. Bianchini, and A. Diaspro - Polarization label-free microscopy imaging of biological samples by exploiting the Zeeman laser emission - Frontiers in Physics, 2021
- A. Le Gratiet, A. Mohebi, F. Callegari, P. Bianchini, A. Diaspro - Review on Complete Mueller Matrix Optical Scanning Microscopy Imaging - Applied Sciences, 2021
- A. Mohebi, A. Le Gratiet, R. Marongiu, F. Callegari, P. Bianchini, A. Diaspro - Combined approach using circular intensity differential scattering microscopy under phasor map data analysis - Applied Optics, 2021.

Conferences – Oral Contributions

- F. Callegari, P. Bianchini, A. Diaspro – A novel approach to label-free microscopy inspired to spectroscopic ellipsometry - Focus On Microscopy (FOM 2023)
- F. Callegari, A. Nussbaum-Lapping, B. Willenberg, J. Pupeikis, A. Zunino, A. Le Gratiet, P. Bianchini, A. Diaspro, C.R. Phillips, U. Keller - Dual-comb laser as a versatile light source for multimodal optical microscopy - Società Italiana di Fisica (SIF) 2022 Congress
- F. Callegari, A. Le Gratiet, A. Zunino, A. Mohebi, P. Bianchini, A. Diaspro - Fast polarization-based label-free imaging in a scanning microscope utilizing the beating signal of a Zeeman Laser (Online Oral Session) - Focus On Microscopy (FOM 2022)
- F. Callegari, A. Le Gratiet, A. Zunino, A. Mohebi, P. Bianchini, A. Diaspro - Label-free microscopy enhanced by the polarization emission of a Zeeman laser (Online Recorded Session) - Società Italiana di Fisica (SIF) 2021 Congress
- F. Callegari, A. Mohebi, P. Bianchini, R. Ranjan, A. Diaspro - Application of He-Ne Zeeman Laser in Polarization-based Microscopy Techniques (Online Recorded Session) - Società Italiana di Fisica (SIF) 2020 Congress

Conferences – Poster sessions

- F. Callegari, A. Le Gratiet, A. Zunino, A. Mohebi, P. Bianchini, C. JR Sheppard, A. Diaspro - Polarization label-free microscopy imaging of biological samples by exploiting the Zeeman Laser emission (Online) - Frontiers in Optics and Laser Science (FiO+LS) 2021

- F. Callegari, A. Le Gratiet, A. Zunino, A. Mohebi, P. Bianchini, A. Diaspro - Application of He-Ne Zeeman Laser in polarization-based characterization of chiral structures (Online) - Focus On Microscopy (FOM) 2021

Conference Proceedings

- Bazzanella, S. Bontorin, F. Callegari, B. Degli Esposti, S. Rabaglia, L. Wolswijk, Alessandro Zunino - Physical based simulation of a real-time LiDAR sensor within a rendering environment based on Unreal Engine 4 - Industrial Problem Solving with Physics (IPSP) 2021 @ Department of Phyiscs, University of Trento, Italy